2015

Experimental and numerical investigations on the flow characteristics of rotary machineries

Zhenyu Wang
Iowa State University

Experimental and numerical investigations on the flow characteristics of rotary machineries

by

Zhenyu Wang

A dissertation submitted to the graduate faculty

in partial fulfillment of the requirements for the degree of

DOCTOR OF PHILOSOPHY

Major: Aerospace Engineering

Program of Study Committee:
Hui Hu, Major Professor
Alric Rothmayer
Anupam Sharma
Chris Rehmann
Xinwei Wang

Iowa State University

Ames, Iowa

2015

TABLE OF CONTENTS

Page

ACKNOWLEDGEMENTS iv
ABSTRACT v
CHAPTER 1. GENERAL INTRODUCTION 1
1.1. Aeroacoustics in small axial fans for computer cooling applications 1
1.2. Innovative twin-rotor and dual-rotor wind turbine designs to improve turbine performance and wind farm efficiency 3
Chapter 2. DEVELOPMENTOF AN ULTRA-QUIET AXIAL FAN FOR COMPUTER COOLING APPLICATIONS 9
2.1. Introduction 10
2.2. Experimental Setup and Test models 12
2.2.1. The baseline and newly designed fans 12
2.2.2. Sound measurements 15
2.2.3. PIV measurements 17
2.3. Experimental Results and Discussions 19
2.4. Conclusions 28
Chapter 3. EXPERIMENTAL AND COMPUTATIONAL STUDY ON AN AXIAL CASE FAN FOR COOLING APPLICATIONS 31
3.1. Introduction 31
3.2. Experimental Setup 34
3.2.1. The axial fan model 34
3.2.2. PIV measurements 35
3.3. Numerical methods 36
3.3.1. Governing equations 37
3.3.2. Computational domain and mesh generation 37
3.3.3. Computational methods and boundary conditions 38
3.4. Results and Discussions 40
3.5. Conclusions 49
CHAPTER 4. A NOVEL TWIN-ROTOR WIND TURBINE DESIGN FOR IMRPOVED TURBINE PERFORMANCE AND WIND FARM EFFICIENCY 53
4.1. Introduction 54
4.2. Experimental Setup and Test Models 60
4.2.1. Atmospheric Boundary Layer (ABL) Wind-tunnel 60

4.2.2. Wind turbine models 62
4.2.3. Power outputs and dynamic wind loads acting on the turbines 64
4.2.4. PIV measurements and point-wise velocity measurements to quantify the wake characteristics behind the model turbines 66
4.3. Measurement Results and Discussions 69
4.3.1. Dynamic wind loads acting on the wind turbine models 69
4.3.2. 2-D PIV measurement results 72
4.3.3. Flow characteristics in the far wakes behind the SRWT and TRWT models 84
4.3.4. Stereoscopic PIV measurements 93
4.4. Conclusion 100
CHAPTER 5. AN EXPERIMENTAL STUDY ON THE WAKE CHRACTERISTICS BEHIND INNOVATIVE DUAL-ROTOR WIND TURTINES 106
5.1. Introduction 107
5.2. Experimental Setup and Test Models 113
5.2.1. Atmospheric Boundary Layer (ABL) Wind-tunnel used in the present study 113
5.2.2. Wind turbine models 115
5.2.3. Dynamic wind loads acting on the turbine and power output measurements 117
5.2.4. PIV and point-wise streamwise velocity measurements to quantify the wake characteristics behind the wind turbine models 119
5.3. Results and Discussions 121
5.3.1. Dynamic wind loads acting on the wind turbine models 121
5.3.2. 2-D PIV measurement results 125
5.3.3. Point-wise flow statistics in the far wakes of the SRWT and DRWT models 136
5.3.4. Power outputs in the wakes behind the SRWT and DRWT models 141
5.3.5. Stereoscopic PIV measurements 146
5.4. Conclusion 152
CHAPTER 6. GERNEAL CONCLUSION 158

ACKNOWLEDGEMENTS

I would like to take this opportunity to say thank you to everyone who has helped me on conducting this research and made this thesis possible. First, I would like to thank my major professor, Dr. Hui Hu, for the opportunity of working with him in the last three and half years, and for his generous guidance, inspiration and patience throughout my entire PhD study.

I would also like to thank my committee members, Dr. Alric Rothmayer, Dr. Anupam Sharma, Dr. Chris Rehmann and Dr. Xinwei Wang, for their insightful comments and suggestions in this work. Besides, I would like to thanks Dr. Partha Sarkar, for providing me the AABL wind tunnel and other facilities to accomplish my wind turbine experiments.

In addition, I would like to thank all of my fellow group members, Dr. Wei Tian, Dr. Blake Johnson, Dr. Meilin Yu, Dr. Yan Zhang, Dr. Ahmet Ozbay, Dr. Rye Waldman, Dr. Kai Zhang, Mr. Wenwu Zhou, Mr. Yang Liu, Mr. Haixing Li, Mr. Zhe Ning, Mr. Morteza Khosravi, Mr. Andrew Bodling, Mr. Pavithra Premaratne and all my other friends for the memorable time in Ames. I am appreciative to all the staff members at the Department of Aerospace Engineering, for their help in the paperwork and answering the endless questions.

Finally, I am extremely grateful to my parents and my grandparents for their unlimited love and support during my whole life. They are my inspiration and motivation for any achievement and success I experience.

ABSTRACT

The research work described in this thesis includes two topics: 1). An experimental and computational study on the aerodynamic and acoustic characteristics of case fans for computer cooling applications; and 2). A comparative study on the aeromechanic performances and wake characteristics of innovative dual-rotor wind turbines (DRWTs) and conventional single-rotor wind turbine (SRWT). For the first topic, by using a commercially-available cooling fan as the baseline, a number of acoustically tailored modifications were implemented in order to reduce the noise level of the cooling fan, which includes optimizing the rotating blades and guide vanes according to axial fan design theory, adding an intake cone in the front of the hub to guide the airflow into the axial fan smoothly, and reducing the tip clearance to lower the noise generation due to tip vortex structures. In order to assess the effects of the modifications on the fan noise reduction, a comparison study was conducted to measure the sound pressure level (SPL) and the sound spectra of the newly designed axial fan in an anechoic chamber, in comparison to that of the baseline fan. The measurement results of our preliminary study revealed that, at the same flow rate, the SPL of the newly designed fan would be up to 5 dB lower than that of the baseline fan. The spectra results demonstrated that the sound power energies in both of peak frequency and broadband frequency for the baseline fan were higher than that of the newly designed fan regardless of flow rate. In addition, a digital particle image velocimetry (PIV) system and numerical simulation were also used to conduct detailed flow field measurements to reveal the inner and outer flow characteristics and unsteady vortex structures associated with the modifications.

For the second topic, a comprehensive study was conducted to investigate the aerodynamics and wake characteristics of innovative dual-rotor wind turbines (DRWTs) consisting of twin-rotor, co-, and counter-rotating configurations, in comparison to a conventional single-rotor wind turbine (SRWT). In addition to measuring the dynamic wind loads acting on the SRWT and DRWT models, a Cobra Probe Anemometry, a conventional 2D and a stereoscopic Particle Image Velocimetry (PIV) system were used to attain the detailed flow field measurements to quantify the flow characteristics in the turbine wakes and to quantitatively visualize the time evolution of the unsteady vortex structures in the wake flows. Furthermore, the power outputs of a duplicate model turbine operating in the wakes behind the DRWT and SRWT models at different downstream locations were also measured and compared quantitatively. The detailed flow field measurements were correlated with the dynamic wind loads and power output measurements to elucidate the underlying physics to explore/optimize design paradigms for higher total power generation and better durability of the wind turbines.

CHAPTER 1. GENERAL INTRODUCTION

1.1. Aeroacoustics in small axial fans for computer cooling applications

It is well known that small axial fans are widely used in computers for cooling applications. As the amount of heat from computer components, such as CPUs and graphic cards, keeps significantly increasing with the great enhancement in computer performance, more and more high-speed axial fans are used to achieve higher cooling performance to meet the requirement of heat dissipation. As a result, significant acoustic noise is generated due to high rotational speed. Therefore, much quieter axial fan designs must be developed due to the increasing demand from customers demanding a silent working environment (Jiang et al., 2007).

The noise generated from axial fans can be separated into two categories: 1) mechanical noise, and 2) aerodynamic noise. Mechanical noise generated by the friction in solid boundaries that can be considered negligible once compared to the sound pressure levels generated from the high RPM rotor. Aerodynamic noise, namely aeroacoustics, is closely related to the aerodynamics of the rotor blades, which would be a much more important noise source as the rotational speed of the axial fan increases (Nashimoto et al., 2004). The noise radiation would be increased by about 18dB if the rotational speed is doubled for a typical axial fan (Lu et al., 2007). The sound pressure levels would be closely related to the flow conditions inside the axial fan. Therefore, detailed flow characteristics in small axial fans need to be thoroughly understood for the development of quieter and more efficient fans in computer cooling applications.

In the past two decades, the noise generation from small axial fans has been investigated extensively by experimental and computational methods (Hodgson et al., 2006). Huang (2003) used a theoretical method to study the fan noise focusing on the radiation from the

interaction between rotor blades and motor struts. It was found that the total sound power is more sensitive to the number of struts than the rotor blades. As the flow in a computer cooling fan is fully turbulent, the three-dimensional flow structure needs to be obtained for a comprehensive analysis due to its close relation to aeroacoustics. Following Huang's work, Lu et al. (2007) conducted a computational study on an isolated axial fan to assess the three-dimensional, unsteady flow fields, and compare the predicted sound radiation with measured data. Axial fan noise, in reality, can be divided into tone and broadband noises. Tone noise is mainly caused by the rotor-stator interaction and is well understood for its generation mechanism (Hase et al., 2011). Broadband noise, on the other hand, is believed to be caused by the turbulence of the flow, such as ingested vortices, secondary inflow distortions, blade trailing edge and tip vortex shedding (Carolus et al., 2007), and its mechanism is not thoroughly elucidated. Carolus et al. (2007) and Hase et al. (2011) found that the turbulent kinetic energy and unsteady blade force can be used as important parameters to evaluate the broadband noise through numerical analysis. In order to reduce the noise generation from axial fans, many strategies were proposed and reported by previous researchers. For example, changing the blade spacing to decrease the tonal noise (Cattanei et al., 2007), and using serrated trailing edge to reduce the broadband noise, especially high-frequency noise, attaching winglets on the rotor blades to change the noise spectrum distributions and the trace of tip vortices to depress the overall noise radiation. However, all the investigations mentioned above only decreased the noise level by 1~2 dB overall with respect to the baseline fan.

In the present study, a comprehensive investigation was carried out to study the mechanism of the noise reduction on an axial fan by using several effective modifications

based on a commercially-available cooling fan. The details including the optimization of the rotor blades and guide vanes according to axial fan design theory, adding an intake cone and reducing the tip clearance to lower the noise generation will be discussed in Chapter 2. The sound pressure level (SPL) and sound spectra of the newly designed fan and the baseline fan will be compared, and a digital particle image velocimetry (PIV) system will be used to achieve the flow field measurements to reveal the differences in flow characteristics associated with the modifications. As the flow field inside the axial fan is very difficult to visualize, a full three-dimensional unsteady computation was conducted for the newly designed fan to obtain more flow information inside the fan, as discussed in Chapter 3. Instantaneous and time-averaged solutions were gathered to elucidate the noise generation due to rotor-stator interactions.

1.2. Innovative twin-rotor and dual-rotor wind turbine designs to improve turbine performance and wind farm efficiency

Wind power is one of the most competitive renewable technologies to alleviate the world's energy dependence on fossil fuels. The electricity produced from modern wind farms can reach as low as USD 0.04~0.05 per kWh, making it competitive with fossil fuel generation. The prospect of wind supplying the base load power is not just a figment of our imagination anymore. However, the challenge to reach this tantalizingly achievable goal should not be underestimated. As the sites with rich wind resources are utilized gradually, new wind farms have to be built at the sites where the wind resources are not as favorable. With the conventional horizontal-axis wind turbine (HAWT) designs, we have already reached the point of diminishing returns. Therefore, the need for revolutionary turbine concepts with higher performance is obvious.

Modern, utility-scale wind turbines are typically horizontal axis designs that use a single rotor with three blades. By applying conservation law in one-dimension, a maximum limit on power coefficient, $C_P \leq 0.59$, can be achieved. This limit, known as the Betz limit, is misleading, as it assumes no wake swirl or viscous losses, and an infinite number of rotor blades. When these assumptions are removed (Okulov et al., 2008; Sharma et al., 2010), the maximum power coefficient potential of a HAWT is close to 0.53. The difference between the maximum value and measured peak performance of modern HAWTs is due to various constraints, such as the root losses induced near the hub region (25% of rotor blades diameter). Utility-scale turbines are deployed in clusters called wind farms. Aerodynamic interactions between turbines in wind farms result in significant energy loss that ranges between 10%~40% (Barthelmie et al., 2007). The primary mechanism of the energy loss is ingestion of low-momentum airflows in the wakes by the downstream turbines. The range of this loss is exceptionally wide because of its strong dependence on wind farm locations, layouts, and atmospheric stability conditions.

The aerodynamics of single-rotor wind turbine (SRWT) and wind farm configuration (comprised of SRWTs) has been extensively investigated using analytical, numerical and experimental techniques. Numerical simulations have ranged from momentum and blade-element theories to time-steady and time-accurate CFD calculations (Snel, 2003; Vermeer et al., 2003). Experiments have also ranged from laboratory scale to real field measurements targeting both isolated and wind farm aerodynamics (Cal et al., 2010; Chamorro et al., 2010; 2011; 2013; Hu et al., 2012). With the wind energy industry fixated on single-rotor HAWT design, primarily due to cost considerations, multi-stage designs (e.g., dual-rotor turbines) have received little concerns. Multi-stage turbomachineries are widely used in gas turbines

and propulsion applications where efficiency is the prime objective need to be considered. While "fuel" in wind turbines is supposedly free, therefore, cost of electricity production instead of efficiency, drives current turbine designs. As we approach the inevitability of having to produce most of our energy sustainably, with wind playing an essential role in this quest, we will run out of sites (land and ocean) where we can realistically install turbines. The focus has to therefore shift towards to efficient turbine and farm designs that extract highest power per surface area.

Multi-stage wind turbines can surpass the Betz limit. Newman (1986) calculated that the maximum C_P of two identical-size dual-rotor wind turbine (DRWT) can be increased up to 0.64, an 8% improvement over the Betz limit. Jung et al., (2005) calculated the performance of a 30kW counter-rotating DRWT and listed the optimum values of distance between rotors and the secondary rotor size. Lee et al. (2010; 2012) compared the design parameters such as combination of pitch angles, rotating speed ratio and radius ratio on a DRWT, and they found that the maximum C_P occurs when the front rotor size was chosen to be 80% of the second rotor. Windpower Engineering & Development has developed a co-axial, twin-rotor turbine with the objective of harvesting more energy at lower wind speeds by using two identical rotors connected by one shaft to a variable-speed generator.

However, none of the DRWT designs mentioned above focuses on what we are targeting with the innovative DRWT concept. There are two objectives to be assessed in the present study: 1) reduce root losses, and 2) mitigate wake losses in a typical wind farm through enhanced wake mixing. The first objective aims to the efficiency of isolated turbine through the use of aerodynamically optimized secondary rotor. The second objective targets

efficiency enhancement by increasing the wake shear and dynamics interaction between vortex structures from the secondary and the main rotors.

The comparisons between a conventional SRWT and innovative twin-rotor wind turbine (TRWT) will be discussed in Chapter 4. The dynamics wind loads acting on the wind turbines, the wake flow quantities behind the turbines measured by 2D and stereoscopic PIV systems and Cobra Probe Anemometry will be characterized quantitatively. The power outputs from a same wind turbine model placed in the wakes will also be measured to assess the velocity deficits recovery ability in the airflows behind the SRWT and the TRWT models. Similar to Chapter 4, the dynamic wind loading, flow characteristic and power output comparisons between the SRWT model and DRWT designs will be quantified clearly in Chapter 5.

References

Barthelmie, R. J., Rathmann, O., Frandsen, S. T., Hansen, K. S., Politis, E., Prospathopoulos, J., … Pijl, S. P. Van Der. (2007). Modelling and measurements of wakes in large wind farms. *Journal of Physics: Conference Series*, *75*, 012049.

Cal, R. B., Lebrón, J., Castillo, L., Kang, H. S., & Meneveau, C. (2010). Experimental study of the horizontally averaged flow structure in a model wind-turbine array boundary layer. *Journal of Renewable and Sustainable Energy*, *2*(1), 013106.

Carolus, T., Schneider, M., & Reese, H. (2007). Axial flow fan broad-band noise and prediction. *Journal of Sound and Vibration*, *300*(1-2), 50–70.

Cattanei, A., Ghio, R., & Bongiovı`, A. (2007). Reduction of the tonal noise annoyance of axial flow fans by means of optimal blade spacing. *Applied Acoustics*, *68*(11-12), 1323–1345.

Chamorro, L., Arndt, R., & Sotiropoulos, F. (2011). Turbulent flow properties around a staggered wind farm. *Boundary-Layer Meteorology*.

Chamorro, L. P., & Porté-Agel, F. (2010). Effects of Thermal Stability and Incoming Boundary-Layer Flow Characteristics on Wind-Turbine Wakes: A Wind-Tunnel Study. *Boundary-Layer Meteorology*, *136*(3), 515–533.

Chamorro, L. P., Tobin, N., Arndt, R. E. A., & Sotiropoulos, F. (2013). Variable-sized wind turbines are a possibility for wind farm optimization.

Hase, T., Yamasaki, N., & Ooishi, T. (2011). Numerical simulation for fan broadband noise prediction. *Journal of Thermal Science*, *20*(1), 58–63.

Hodgson, M., & Li, I. (2006). Experimental study of the noise emission of personal computer cooling fans. *Applied Acoustics*, *67*(9), 849–863.

Hu, H., Yang, Z., & Sarkar, P. (2012). Dynamic wind loads and wake characteristics of a wind turbine model in an atmospheric boundary layer wind. *Experiments in Fluids*, *52*(5), 1277–1294.

Huang, L. (2003). Characterizing computer cooling fan noise. *The Journal of the Acoustical Society of America*, *114*(6), 3189.

Jiang, C., Chen, J., Chen, Z., Tian, J., OuYang, H., & Du, Z. (2007). Experimental and numerical study on aeroacoustic sound of axial flow fan in room air conditioner. *Applied Acoustics*, *68*(4), 458–472.

Jung, S. N., No, T.-S., & Ryu, K.-W. (2005). Aerodynamic performance prediction of a 30kW counter-rotating wind turbine system. *Renewable Energy*, *30*(5), 631–644.

Lee, S., Kim, H., & Lee, S. (2010). Analysis of aerodynamic characteristics on a counter-rotating wind turbine. *Current Applied Physics*, *10*(2 SUPPL.), S339–S342.

Lee, S., Kim, H., Son, E., & Lee, S. (2012). Effects of design parameters on aerodynamic performance of a counter-rotating wind turbine. *Renewable Energy*, *42*, 140–144.

Lu, H. Z., Huang, L., So, R. M. C., & Wang, J. (2007). A computational study of the interaction noise from a small axial-flow fan. *The Journal of the Acoustical Society of America*, *122*(3), 1404.

Nashimoto. A, Fujisawa. T, A. T. (2004). Measurements of Aerodynamic Noise and Wake Flow Field in a Cooling Fan with Winglets. *Journal of Visualization*, *7*(1), 85–92.

Okulov, V. L., & Sørensen, J. N. (2008). Refined Betz limit for rotors with a finite number of blades. *Wind Energy*, *11*(4), 415–426.

Sharma, A. and Frere, A. (2010). Diagnosis of Aerodynamic Losses in the Root Region of a Horizontal Axis Wind Turbine. *General Electric Global Research Center Internal Report*.

Snel, H. (2003). Review of aerodynamics for wind turbines. *Wind Energy*, *6*(3), 203–211.

V, E. S. P. B., & Newman, B. G. (1986). Multiple Actuator-disc Theory for Wind Turbines. *Journal of Wind Engineering and Industrial Aerodynamics*, *24*, 215–225.

Vermeer, L., Sørensen, J., & Crespo, A. (2003). Wind turbine wake aerodynamics. *Progress in Aerospace Sciences*.

Chapter 2. DEVELOPMENT OF AN ULTRA-QUIET AXIAL FAN FOR COMPUTER COOLING APPLICATIONS

Zhenyu Wang and Hui Hu

Department of Aerospace Engineering, Iowa State University

Abstract: We report the progress made in our recent study to develop an ultra-quiet axial fan for computer cooling applications. By using a commercially-available cooling fan as the baseline, a number of acoustically tailored modifications were implemented in order to reduce the noise levels of the cooling fan, which includes optimizing the rotator blades and guide vanes according to axial fan design theory, adding an intake cone in the front of the hub to guide the airflow into the axial fan smoothly, and reducing the tip clearance to lower the noise generation due to tip vortex structures. In order to assess the effects of the modifications on the fan noise reduction, a comparison study was conducted to measure the sound pressure level (SPL) of the newly designed axial fan in an anechoic chamber, in comparison to that of the baseline fan. The measurement results of our preliminary study revealed that, at the same flow rate, the SPL of the newly designed fan would be up to 5 dB lower than that of the baseline fan. The sound spectra of these fans were also analyzed under the same flow rate conditions. The results demonstrated that the sound power energies in both the peak frequency and the broadband frequency of the baseline fan were higher than that of the newly designed fan regardless of the flow rate. In addition to measuring the sound pressure levels (SPLs) and the sound spectra of the fans, a digital particle image velocimetry (PIV) system was also used to conduct detailed flow field measurements to reveal the changes of the flow characteristics and unsteady vortex structures associated with the

modifications. “Time-averaged” PIV measurements illustrated the ensemble-averaged statistics of the flow quantities in the flow field around the axial fans.

2.1. Introduction

With the increase in heat generation from the electrical devices, e.g., data servers and large IT facilities, small axial fans are widely used for cooling applications. As fan diameter is restricted by the limitation of space in such equipment, the rotational speed of the fan must increase significantly to achieve a higher cooling ability (Shigemitsu et al, 2010). Although high speed fans solve the problem of cooling, they also cause the problem of high noise levels. Since the noisy environment caused by cooling fans may affect the working efficiency of employees significantly, therefore, there is a strong demand for noise reduction in cooling fans, and at the same time, maintaining their cooling ability.

When the blade rotational speed becomes higher, mechanical noise can be neglected compared to aeroacoustics. The aeroacoustic levels are closely related to the aerodynamic performance of the fans. As a result, the flow performance in axial fans would have significant effect on the noise radiation. Because the flow in axial fans is quite complicated, the underlying physics of the relationship between flow performance and noise radiation is still difficult to reveal clearly. In the past two decades, there have been considerable efforts to depress the aeroacoustic noise from axial fans. Dam (1984) installed winglets on the blade and reported an effective noise reduction on an axial fan. However, because of the limited experimental capabilities at that time, the physical mechanism for this modification was not clearly explained. Later, to investigate the mechanism of winglets for noise drop, Nashimoto et al. (2004) continued the study in recent years and found that the overall noise level was decreased while the low-frequency noise spectrum was changed when the winglet was

installed. The PIV results demonstrated the influence of the winglet appeared in the traces of the tip vortices and the magnitude of vorticity was reduced in the near wake region, which may indicate the noise reduction. Huang (2003) performed a theoretical study on the cooling fan noise which focused on the acoustic radiation from the interaction between rotor blades and motor struts. He illustrated that a sound source can be decomposed into the components of axial thrust, circumferential drag, and radial force. Quantitative analysis indicated that the drag force and the coincident thrust force can contribute equally to noise generation, and an empirical aerodynamic model of rotor-strut interaction revealed that the total sound power was more sensitive to the number of struts than rotor blades.

Fan blade tip clearance has also received significant research attention. Fukano et al, (1986, 2004) found that a smaller tip clearance can improve flow performance and depress noise radiation, at both the maximum operating efficiency and the low flow rate. Later, he also demonstrated that the tip clearance flow noise consisted of discrete frequency components and broadband components, which were induced by periodic velocity fluctuation and velocity fluctuation in the blade passage, respectively. The peak frequencies in the vortical flow were mainly observed in the first four harmonics of the blade passing frequency, which could be an important noise source when the fans rotated at high RPMs.

Axial fans require struts to support the rotation blades and motor. Guide vanes are typically installed in the fan outlet because they not only can support the blades and motor but also can enhance the flow performance. However, the interactions between rotor and stator may induce unnecessary aeroacoustic noise if the guide vanes are poorly designed. The mechanism of rotor-stator interaction noise was investigated by Lakshminarayana et al. (1982). He suggested that the main source of this noise was caused by flow irregularities in

the tip leakage flow and the secondary flow around the tip and hub regions. Cooper et al. (2006) found that tone noise, a significant component of rotor-stator interaction noise appeared at multiples of the blade passing frequency (BPF), which was caused by the impingement of the periodic fan wakes with stator vanes. Additionally, Cooper observed that the interaction of rotor-wake turbulence with the stator also contributed an important broadband component to the overall noise. Thus, the stator structures, such as the number of guide vanes, stagger angle, geometry and the installed position, can have essential influences on the noise generation.

In the present study, a comprehensive investigation was conducted to investigate the physical mechanism of the noise reduction of an axial fan by modifying some features in it. The modifications on the axial fan, such as the blade geometry, tip clearance, intake cone, and guide vanes were investigated to achieve a better flow performance and lower acoustical level. A digital Particle Image Velocimetry (PIV) system was used to conduct detailed flow field measurements to quantify turbulent flow structures around the axial fan.

2.2. Experimental Setup and Test models

2.2.1. The baseline and newly designed fans

(a) Front view (b) Back view

Fig.1: The geometry of the baseline fan

Figure 1 shows the geometric configurations of the baseline fan. The rotor was made by plastics and has 7 blades. The diameters of casing and hub are 120mm and 62mm, respectively. The tip clearance between the rotor and casing is around 1.5mm. There are 11 guide vanes installed on the outlet, which can be used to support the motor and enhance the flow efficiency by reducing the tangential velocity. The maximum rotational speed of this low pressure axial fan can reach up to 9000 rpm, and therefore, high speed rotation can generate high levels of noise. The blades were driven by a brushless DC motor and the rotational speed was controlled by a Pulse-Width Modulation (PWM) controller. A series of square waves generated by a function generator was used as the input signals to change the rotational speed of the axial fan.

Fig.2 illustrates the newly designed fan by implementing several modifications based on the baseline fan shown in Fig.1. The rotor and stator were designed in Solidworks and then constructed by a rapid prototyping machine in the Aerospace Engineering Department at Iowa State University. The rotor has a casing diameter of 120mm and a hub diameter of 62mm, which are identical to the dimensions of the baseline fan. The design modifications on this new fan are as follows. First of all, the wing section of the blades was re-selected and its stagger angle at each spanwise direction was arranged to achieve the maximum lift-to-drag ratio under different Reynolds numbers. Second, in order to reduce the tip vortex generation, the tip clearance was decreased to be about 1mm compared to 1.5mm in the baseline fan. Additionally, the wires in the baseline fan model obstructed the airflow emanating from the flow passage, a guidance channel (see the black elliptical circle on Fig.2b) was also designed to decrease the drag force induced by the wires. Lastly, the stagger angles

of the guide vanes were optimized to decrease the effect generated by the rotor-stator interactions.

(a) Front view (b) Back view

Fig.2: Newly designed fan

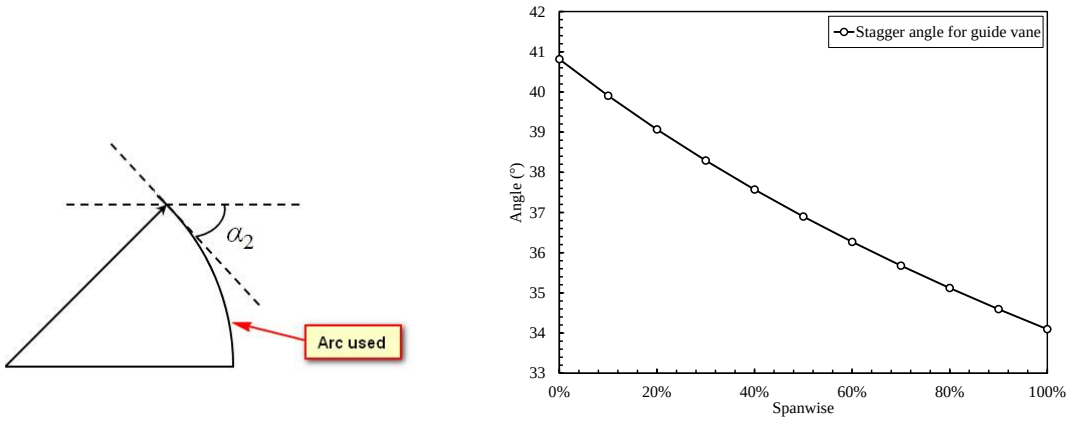

(a) Guide vane geometry (b) Stagger angle for guide vane

Fig.3: Guide vane parameters

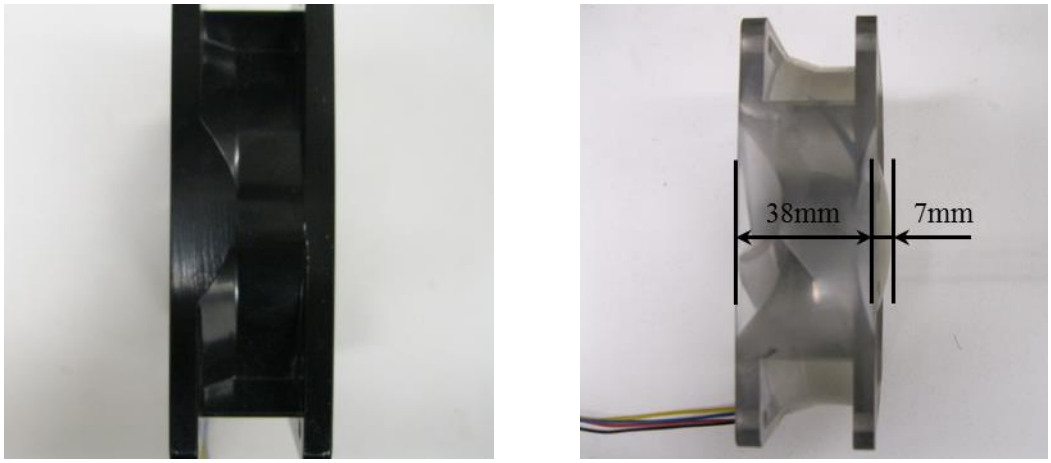

(a) Baseline fan (b) Newly designed fan

Fig.4: Modifications on hub

As a higher streamwise velocity emanating from the axial fans would indicate a higher cooling ability, therefore, the streamwise airflow velocity should be increased as high as possible. Figure 3 depicts an arc used for designing the guide vanes, which can be useful for guiding the rotating airflow into streamwise, where α_2 is the flow angle at the trailing edge of the rotating blades. Lastly, Figure 4 shows a 7 mm long intake cone that was amended on the front of hub for guiding the airflow into the newly designed axial fan smoothly to reduce the distortion at inlet. While the airflow would impinge directly on the flat surface in the baseline model (shown in Fig.4a), then producing extra loss and unnecessary noise.

2.2.2. Sound measurements

The axial fan noise measurements were conducted in an anechoic chamber (as shown in Fig.5a) in the Aerospace Engineering Department at Iowa State University. The background noise in the chamber is lower than 20 dB(A). The sound pressure level (SPL) was measured by a Bruel & Kjaer (Type 2221) sound level meter with A-weighting filter, which was located 1m in front of the fan inlet (We also measured the SPL at different locations which equally distributed around the test fan, the positions and typical results are illustrated in Fig

5c&d). In order to avoid the unnecessary noise induced by the vibration, the axial fan was mounted onto the frames by using the flexible wires. Figure 5(b) shows a linear relationship between the rotational speed and the TTL signal (duty cycle, %) from the function generator. Thus, the rotational speed of the fan can be accurately controlled by adjusting the TTL signal generated from the function generator.

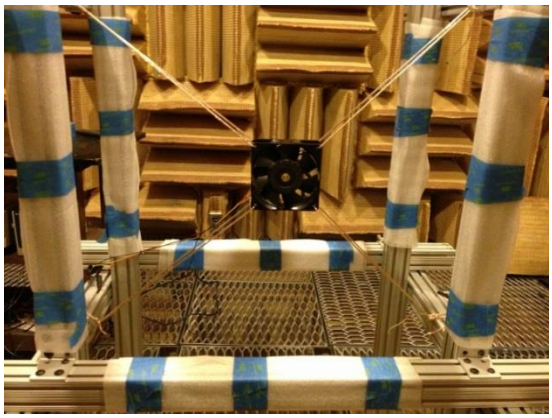

(a) Sound test set-up

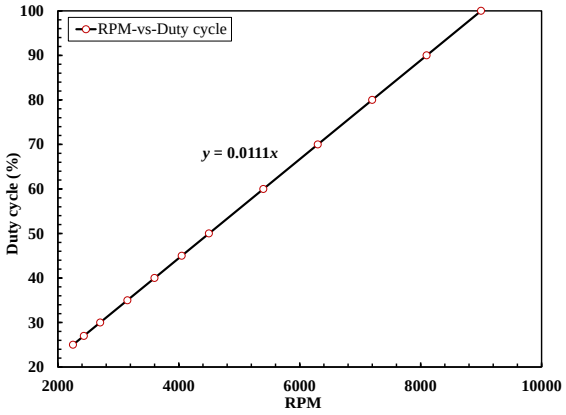

(b) Relationship between rpm and duty cycle

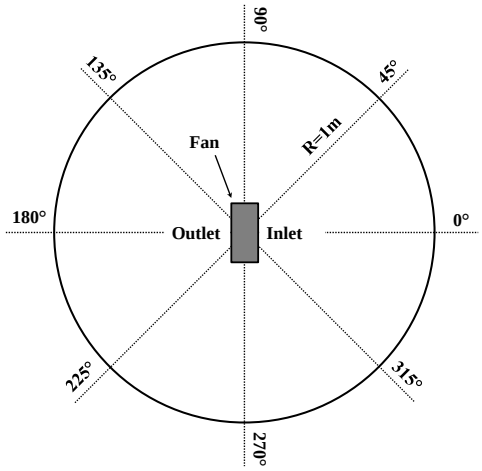

(c) Sound test at circumferential locations

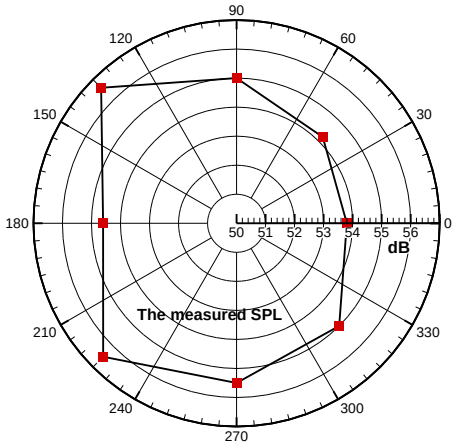

(d) Typical results from the test

Fig.5: Sound pressure level measurement

2.2.3. PIV measurements

In recent years, PIV technique has matured into a powerful tool that can be used to investigate the instantaneous and time-averaged flow fields in turbomachineries and other studies related to aerodynamics (Jiang et al., 2007; Yoon et al., 2004; Yu et al., 2007). It is a planar measurement technique wherein a pulsed-laser light sheet is used to illuminate a flow field seeded with tiny tracer particles. A series of images, captured by a high-speed camera are used to record the motion of the tracer particles as they follow the flow movement. The time interval between the two frames is determined by the mean flow velocity in the area of investigation. The illumination system is synchronized with the CCD camera by the synchronizer to obtain instantaneous and time-averaged velocity fields.

In the present study, a high-resolution digital PIV system was used to measure the details of outer flow fields of the axial fan models. Figure 6 illustrates the schematic of the PIV system used in the present experiment. For the PIV measurements, the airflow was seeded with ~1μm oil droplets by using a fog machine (ROSCO 1900). Illumination was provided by a double-pulsed Nd:YAG laser (EverGreen 200) with a pulse energy of 200 mJ at the wavelength of 532 nm. The laser beam was shaped to a sheet by a set of mirrors along with spherical and cylindrical lenses. The thickness of the laser sheet in the measurement region is about 1 mm. A high-resolution 14-bit CCD camera (PCO1600) was used for image acquisition with the axis of the camera oriented perpendicular to the laser sheet. The CCD camera and the double-pulsed Nd:YAG laser were connected to a host computer via a digital delay generator (BNC565), which controlled the timing of the laser illumination and camera acquisition.

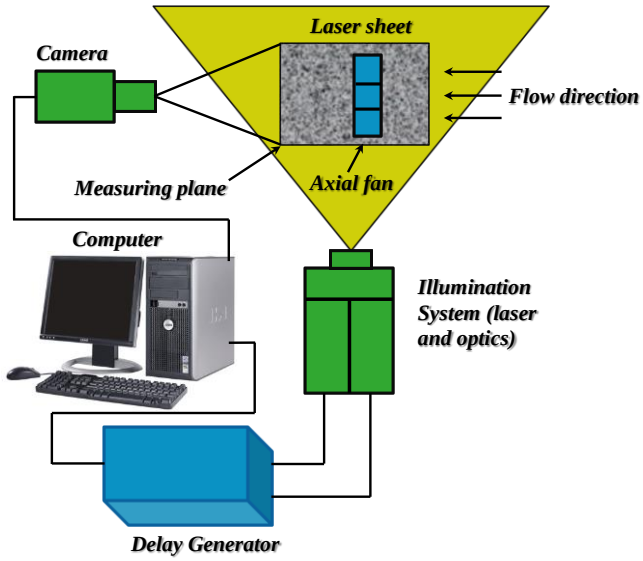

Fig.6: PIV measurement set-up

The time-averaged PIV measurements were conducted during the experiments, which were performed to determine the instantaneous and ensemble-averaged flow statistics (e.g., mean velocity, Reynolds stress, T.K.E) in the outer field of the test fan models. The cooling fans were operated at duty cycles in the range of 30%-80% to achieve low to high rotational speeds. According to different rotational speeds of the fan, the delay time was also varied correspondingly from 35μs to 90μs. For each selected test case, 600 instantaneous frames were captured for post-processing. After PIV image acquisition, the instantaneous PIV velocity vectors were obtained from the cross-correlation with 32 × 32 pixels interrogation windows. An effective overlap of 50% of the interrogation windows was employed in PIV image processing. The vorticity ($\omega_z = \frac{\partial v}{\partial x} - \frac{\partial u}{\partial y}$) can be calculated from the instantaneous velocity vectors (u_i,v_i). The distributions of the ensemble-averaged flow quantities such as the mean velocity, normalized Reynolds stress ($\tau = -\overline{u'v'} / u_{avg}^2$), and turbulence kinetic energy

($T.K.E = \frac{1}{2}(\overline{u'^2} + \overline{v'^2}) / u_{avg}^2$) were also calculated from the data after image processing, where u_{avg} represents the averaged axial velocity in the blade passage.

2.3. Experimental Results and Discussions

By implementing the PIV technique in the present study, the velocity distributions in a specific area can be obtained, and then the flow rate in this area can be calculated by mass conservation equation. Since the velocity in the spanwise direction was not uniformly distributed, an integral should be implemented to calculate the flow rate of the axial fan. The ensemble-averaged axial velocity can be extracted from the time-averaged PIV results at each small interrogation window. When the velocity distributions were obtained, the flow rate can be calculated by the expression of $Q = \int UdA$.

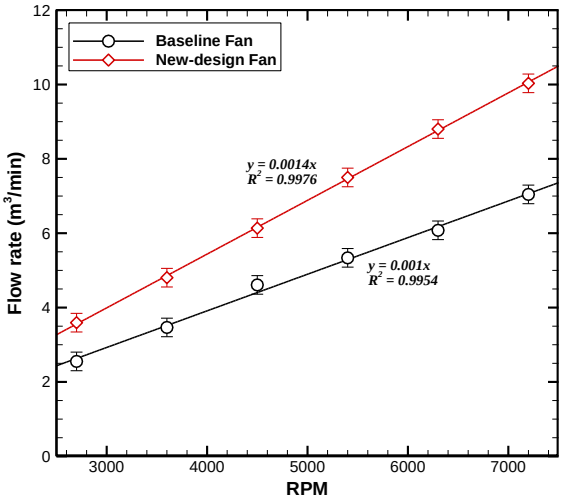

(a) Flow rate vs. Rotational speed

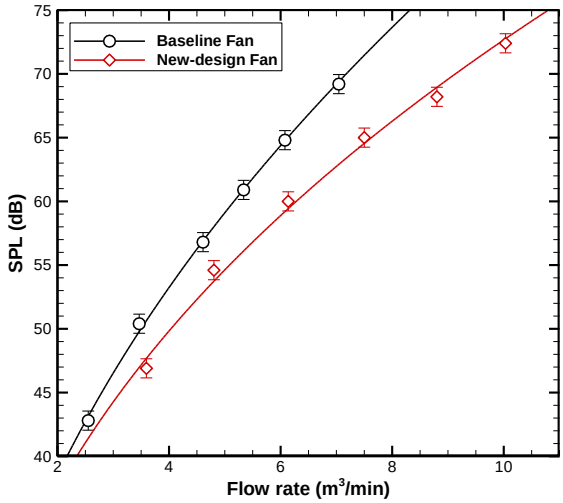

(b) SPL vs Flow rate

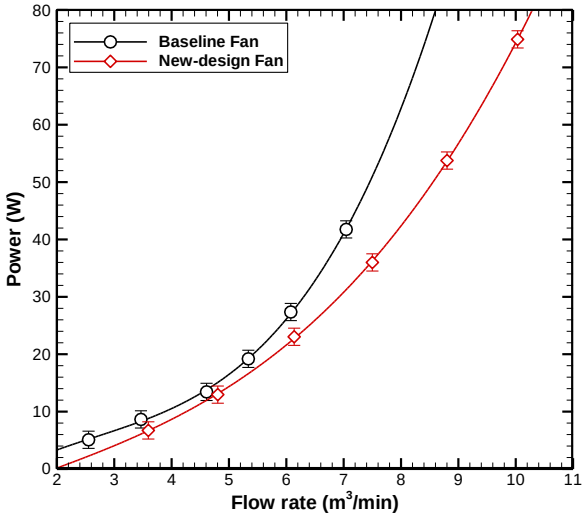

(c) Power vs. Flow rate

Fig.7: Comparison between the baseline fan and the newly designed fan

Figure 7(a) depicts the flow rate comparison between these two fans under different rotational speeds. It can be seen clearly that the flow rate from the newly designed fan is about 30% even up to 40% higher than that from the baseline fan at the same rotational speed. The flow rate difference between them would increase gradually as the rotational speed increases. Additionally, a linear relationship between the flow rate and rotational speed for both of the fans is found based on the test points. The slope of the fitting line can be used for evaluating the capacity of fans. Since the relationship between flow rate and rotational speed has been established, the connection between the sound pressure levels (SPLs) and the flow rate can be obtained indirectly by calculating through the linear relationship shown in Fig.7(a). It is more important to compare the noise level for these two fans under the same flow rate, namely, the same cooling ability. It can be easily found that the newly designed fan has better noise characteristics than the baseline fan when they operate at the same flow rate. This indicates the newly designed fan has better sound performance compared to the baseline fan when they have the same cooling abilities (as shown in Fig.7(b)). For example, the newly

designed fan at a low flow rate (i.e. 3m^3/min) is about 2 dB lower than the baseline fan and has about up to a 6 dB reduction at a high flow rate (i.e. 7m^3/min). The SPL difference between these two fans is increased with the flow rate keeps increasing, which indicates the newly designed fan has a better sound performance than the baseline fan when they are operated at a relatively high rotational speed. From another perspective, when comparing these two fans at the same sound level, the flow rate of the newly designed fan is considerably higher than that of the baseline fan. On the same SPL, the newly designed fan has about 14% and 25% increases in the flow rate at the low (e.g. <50dB) and high (e.g. >70dB) sound levels, respectively. Compared to a 1dB reduction by attaching the winglets on the axial fan rotating blade (Nashimoto et al., 2004) and a 2dB decrease by using incline S-shape trailing edge (Heo et al., 2011), the modifications implemented in the newly designed fan gains a huge improvement for the sound performance. These strategies could be useful for developing the next-generation quiet axial fans in the future. Figure 7(c) shows the relationship between the power requirements and the flow rate. It can be observed that the power input for the newly designed fan is also less than that of the baseline model, which means the newly designed fan has a better flow efficiency. When the flow rate is relatively low (e.g., 3m^3/min), the power requirement for the baseline fan is only slightly higher than that of the newly designed fan. However, when the flow rate is relatively high (e.g. 7m^3/min), the advantage in power requirement for the newly designed fan appears. If the axial fans is ran at a flow rate of 7m^3/min, the newly designed fan has better energy saving abilities because it can save 10 Watts compared to the baseline fan.

As we know, not only the overall SPL is significant for fan noise but also the sound quality, in other words, both the tonal and broadband contents of fans are important. It has

been widely known that the human ear doesn't respond equally to the sound frequency, and is very sensitive to frequencies around 1,000~2,000 Hz (Suárez et al., 2008). Sound spectra, hence, are required to be captured for further understanding of the noise emission, especially to explain why the newly designed fan can provide a better sound performance over the baseline fan. Figure 8 illustrates the sound spectra distributions that were measured by a microphone located at 1m upstream of the test fan models, where Y axis represents the amplitude received by the microphone and X axis is the frequency domain during the measurements. It should be noted that the horizontal axis frequencies were normalized by the blade passing frequency for each fan model. The selected flow rate conditions (i.e., flow rate = $3m^3$/min, $5m^3$/min and $7m^3$/min) represent low, medium, and high rotational speeds during the operation, respectively. As expected, the peak frequencies are proportionally increased by the increasing of the rotational speed of the fan rotor. As shown in Figure 8(a), clear tonal components can be found in the frequency range less than 5BPFs for both of the fan models. The amplitude of the tonal and broadband components in this range of the newly designed fan is lower than the amplitudes of the baseline fan due to a weaker rotor-stator interaction. The sound pressure level for the tonal peaks as well as the broadband frequencies in the baseline case is observed to be considerably higher than that of the newly designed fan. The tonal frequency of the baseline fan can also be found clearly to spread from 1BPF to 10BPF in comparison to the low flow rate case (i.e., Flow rate = $3m^3$/min). Figure 8(c) demonstrates the relatively high flow rate case, where the noise power becomes more dominant by the tonal peaks in comparison to the previous two flow conditions, and the BPFs are continually increased due to the increasing fan rotational speeds. The sound power of both the tonal

components and broadband frequencies is enhanced significantly compared with the low flow rate cases. These findings coincide with the overall SPL results illustrated in Figure 7.

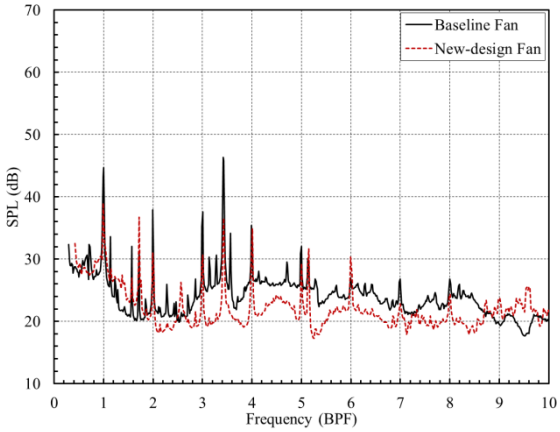

(a) Flow rate = $3m^3$/min

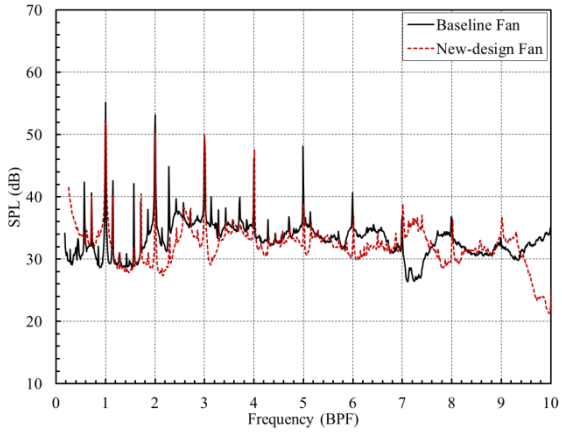

(b) Flow rate = $5m^3$/min

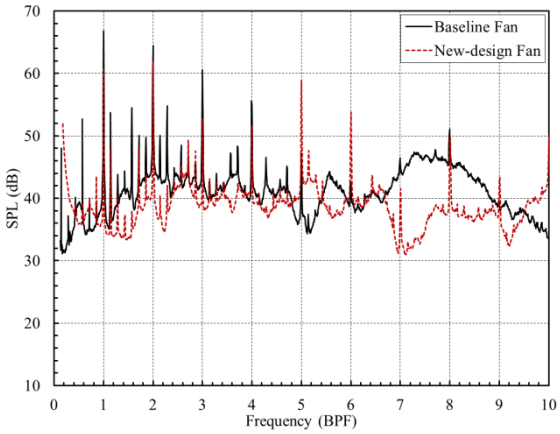

(c) Flow rate = $7m^3$/min

Fig.8: Sound spectra measured at the same flow rate for the fan models

Figures 9~11 compare these two fans in terms of ensemble-averaged velocity distribution, vorticity distribution, turbulence kinetic energy, and normalized Reynolds stress at the flow rate of $5m^3$/min, representing the typical flow condition observed from the PIV measurements. Recall that there is about a 4 dB reduction in the newly designed fan at the medium flow rate (shown in Fig.7b), the difference in noise levels is intrinsically caused the aerodynamic performances of these two fans. Flow field details can help us to understand the

disparity in relation with the noise levels. For this reason, the PIV results are expected to elucidate the underlying physics behind it.

Figure 9 illustrates the ensemble-averaged velocity and vorticity comparisons between the baseline fan and the newly design fan. The vectors and contours indicate the velocity and vorticity distributions, respectively. Similar to the study conducted by Jiang et al. (2007), the highest axial velocity is observed at near medium radius of the blade passage. An interesting flow phenomenon can be found: the low-momentum flow region between the upper and lower streams deflects upward slightly in wake region for both the fan models, and the wake deflection in the newly designed fan has a larger angle (~7 deg) in comparison to that in the baseline axial fan (~5 deg). The high-momentum airflow emanates from the baseline fan and the newly designed fan shapes into two streams and then expands gradually when they are moving downstream. It is apparent that the wake from the newly designed fan has the expansion angles of ~25 deg and ~22 deg for the upper and lower streams, respectively. However, the baseline fan only managed to deflect the upper and lower streams by 15 and 9 deg, respectively. It indicates that a stronger entrainment occurs in the wake of the newly designed fan, and the streamwise velocity in this region is decreased correspondingly due to the total flow rate still being the same. Additionally, the flow in the lower stream (from X/D=0.4 to X/D=0.9) in the baseline fan case has a discontinuous region, which can be inferred that the airflow is impeded by the stators due to the poor guide vane design. Since the rotor-stator interaction has already been identified as an essential noise source emitting from the axial fan (Lu et al., 2007), inappropriate rotor-stator designs, such as the unmatched flow angles between rotor and stator, would generate the additional noise as well as decrease

the efficiency of axial fan. For this reason, the interaction noise between rotor and guide vanes for the baseline fan should be slightly higher compared to the newly design fan.

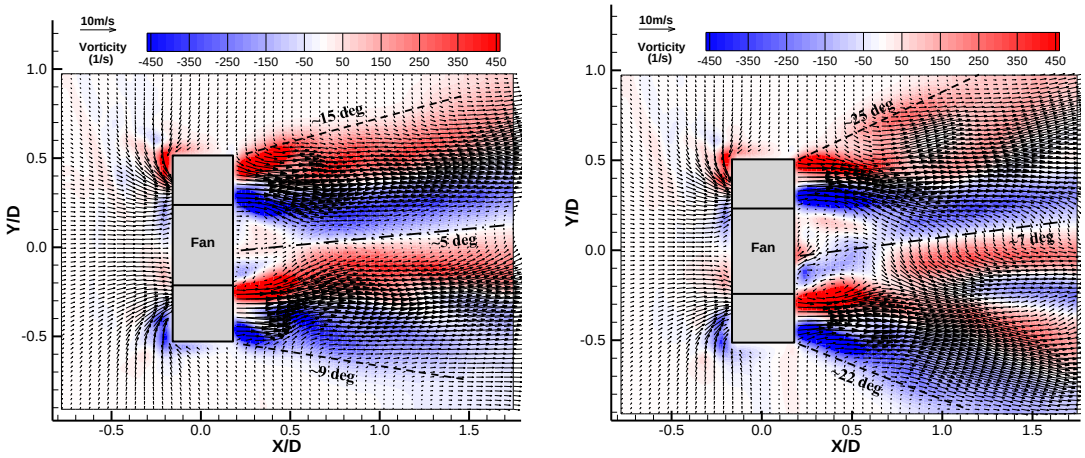

Fig. 9: Ensemble-averaged velocity and vorticity distributions for the baseline (left) and the newly designed (right) fans

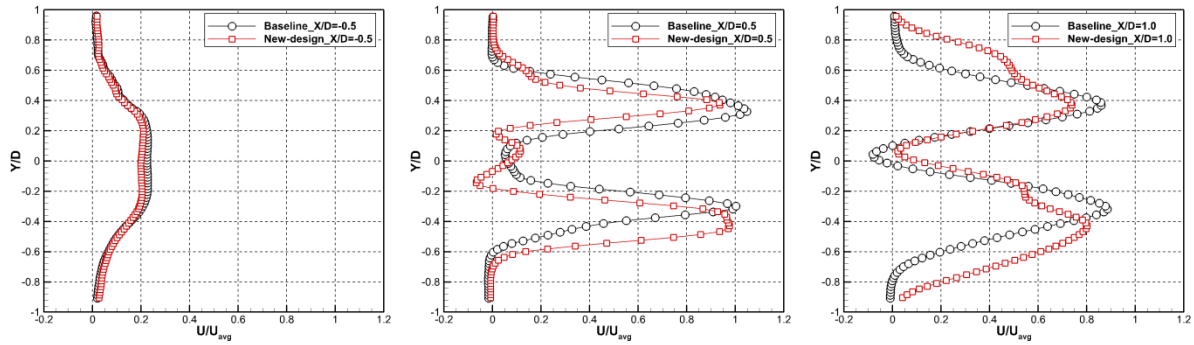

(a) X/D=-0.5 (b) X/D=0.5 (c) X/D=1.0

Fig. 10: Ensemble-averaged axial velocity profiles in the wake region

In order to reflect the characteristics of the downstream wake flow of the axial fans more evidently and quantitatively, the transverse profiles at different downstream locations (i.e., X/D=-0.5, X/D=0.5 and X/D=1.0) are extracted from the PIV results and plotted in Fig. 10. It can be seen clearly that the axial velocity at the inlet side (i.e., X/D=-0.5) in the central region (-0.3<Y/D<0.3) of the newly designed fan is slightly lower than that of the baseline fan, because the extruded intake cone amended on the hub that extends the airflow stagnation point upstream. The axial velocity for these two fan models at the rest of the spanwise

locations remain at the same level. The velocity distributions are found to be quite close to each other at the location of X/D=0.5 behind the fan outlet. However, a huge difference in the flow velocities can be observed at X/D=1.0. The peak velocities in the lower streams only have a minor difference, but the size of the high momentum airflow in the wake of the newly designed fan is much wider than that in the baseline fan. More apparent differences can be found in the upper stream locations, where the high momentum airflow in the baseline case has a larger peak velocity and a smaller width.

As mentioned above, the TKE and Reynolds stress levels are normalized with respect to the averaged streamwise velocity. Figure 11(a) shows the TKE level distributions of the two fan models. It is believed that the TKE levels can be qualitatively used to represent the magnitude of the broadband noise sources (Heo et al., 2011), so the TKE levels of the flow outside of the axial fan can be evaluated as a significant source instead of measuring the broadband noise directly. In the wake flow, the lowest TKE level appears right behind the outlet, and it is enhanced significantly as the interference between low- and high-speed airflows keep increasing. According to the findings shown in Fig.7(a), the rotational speeds of the baseline fan would be higher than that of the newly designed fan when they operated under the same flow rate, so the rotor-stator interaction would cause stronger pressure fluctuations inside the baseline fan. Higher pressure fluctuations would induce the higher TKE levels in the inner flow region and these pressure fluctuations can propagate downstream to increase the flow instability in the wake region. As expected, the baseline fan has a higher TKE compared to the newly designed fan in the far wake locations. High turbulent kinetic energy levels would be associated with higher noise propagating from the internal flow field due to the interactions between the rotor and stator.

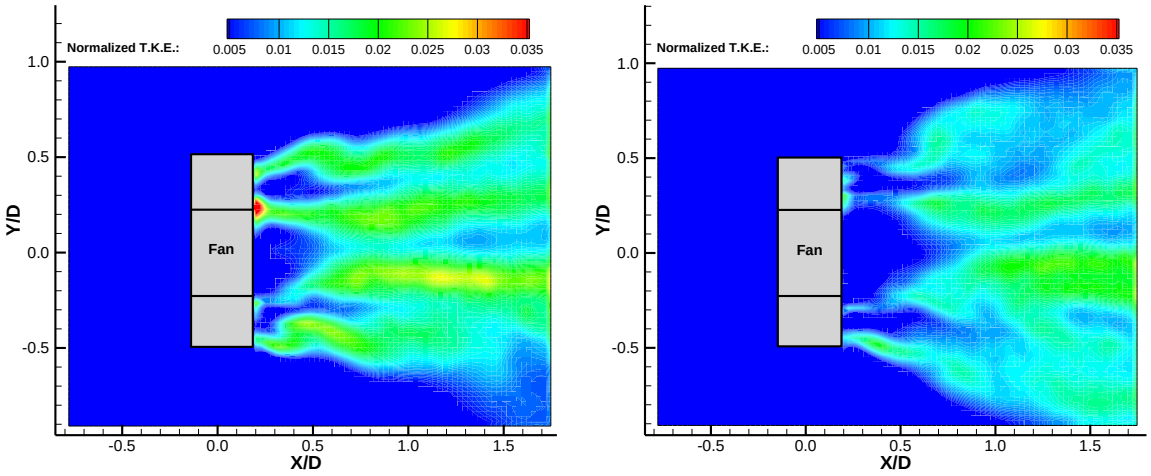

(a) TKE distributions for the baseline (left) and the new-design (right) fans

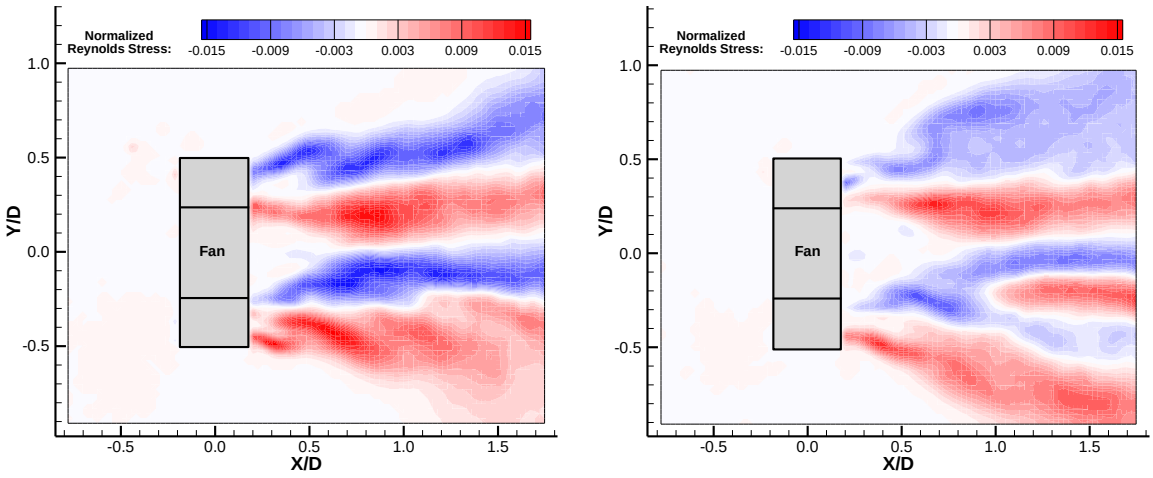

(b) Reynolds Stress distributions for the baseline (left) and the new-design (right) fans

Fig.11: PIV measurement results at the flow rate =5.0m^3/min

Figure. 11(b) illustrates the normalized Reynolds stress distributions in the flow region. Apparently, similar to the results shown in Fig. 11(a), the strength of the normalized Reynolds stress in the wake of the baseline fan is higher than that of the newly designed fan. There are two pairs of "jet-like" flow structures that appear in the wake of the baseline fan. The region with higher Reynolds stress, namely, the shear layer, has larger velocity gradient which leads to stronger shear stresses compared to the newly designed fan. Since the rotational speed of the baseline fan is higher than that of the newly designed fan under the

same flow rate, the stronger rotor-stator interactions and higher noise level would be associated with the increase of the TKE and Reynolds stress levels in the wake flow.

2.4. Conclusions

A comprehensive study was conducted to investigate noise reduction strategies for an axial fan by experimentally investigating some modifications of a baseline axial fan. Sound pressure level measurements and spectra distributions were acquired in an anechoic chamber for both of the fan models.

The flow rate and noise measurement results revealed that the flow rate from the newly designed fan was about 30-40% higher than that of the baseline model on the same rotation speed. An approximately linear relationship between flow rate and rotational speed was found in both the axial fans. Additionally, the overall sound pressure level for the newly designed fan at the relatively low flow rate (e.g., $3m^3$/min) was about 3 dB quieter and there is about a 6 dB decrease at the relatively high flow rate (e.g., $7m^3$/min) compared to the baseline case. The power input requirement for the newly designed fan was less than that of baseline at the same flow rate, which indicated higher flow efficiency in the newly designed fan.

The sound spectra results demonstrated that both the tonal components and the broadband components for the baseline fan were higher than that of the newly designed fan under the three selected flow rate conditions. The higher flow rate corresponded with higher sound power as well as more tonal peaks were found in the measurements. The measured BPF results agreed well with the calculated frequency in each test case.

The PIV results illustrated that the flow in the lower stream of the baseline fan was discontinuous when the airflow emanated from the fan outlet, which indicated the guide vane

may have a poor design. It can be found that this problem was solved in the newly designed fan. The wake expansion angles in the newly designed fan case were higher than those of the baseline case. The baseline fan has higher TKE as well as Reynolds stress levels compared with the newly design fan on the same flow rate, which were propagated by the stronger pressure fluctuations generated through rotor-stator interaction, and corresponded to higher rotor-stator interaction noise levels compared with the newly design fan at the same flow rate.

ACKNOWLEDGMENTS

The support from Iowa Alliance for Wind Innovation and Novel Development (IAWIND) and National Science Foundation (NSF) under award number of CBET-1133751 is gratefully acknowledged. The authors also want to thank Jerry Xu of Futurewei for help and useful discussions related to the present study.

References

Cooper, A. J., & Peake, N. (2006). Rotor-Stator Interaction Noise in Swirling Flow: Stator Sweep and Lean Effects. *AIAA Journal*, *44*(5), 981–991.

Dam, C. P. van. (1984). Natural Laminar Flow Airfoil Design Considerations for Winglets on Low-speed Airplanes. *NASA Contractor Report*, 1–26.

Fukano, T., & Jang, C.-M. (2004). Tip clearance noise of axial flow fans operating at design and off-design condition. *Journal of Sound and Vibration*, *275*(3-5), 1027–1050.

Heo, S., Cheong, C., & Kim, T.-H. (2011). Development of low-noise centrifugal fans for a refrigerator using inclined S-shaped trailing edge. *International Journal of Refrigeration*, *34*(8), 2076–2091.

Huang, L. (2003). Characterizing computer cooling fan noise. *The Journal of the Acoustical Society of America*, *114*(6), 3189.

Jiang, C., Chen, J., Chen, Z., Tian, J., OuYang, H., & Du, Z. (2007). Experimental and numerical study on aeroacoustic sound of axial flow fan in room air conditioner. *Applied Acoustics*, *68*(4), 458–472.

Lakshminarayana, B., Thompson, D. E., & Trunzoj, R. (1982). Strut or Guide Vane Secondary Flows and Their Effect on Turbomachinery Noise. *Journal of Acraft*, *20*(2), 178–186.

Lu, H. Z., Huang, L., So, R. M. C., & Wang, J. (2007). A computational study of the interaction noise from a small axial-flow fan. *The Journal of the Acoustical Society of America*, *122*(3), 1404.

Nashimoto. A, Fujisawa. T, A. T. (2004). Measurements of Aerodynamic Noise and Wake Flow Field in a Cooling Fan with Winglets. *Journal of Visualization*, *7*(1), 85–92.

Shigemitsu, T., Fukutomi, J., Okabe, Y., & Iuchi, K. (2010). Performance and Flow Condition of Contra-rotating Small-sized Axial Fan at Partial Flow Rate. *International Journal of Fluid Machinery and Systems*, *3*(4), 271–278.

T. Fukano, Y. Takamatsu, K. K. (1986). THE EFFECTS OF TIP CLEARANCE AXIAL AND ON THE NOISE FANS OF PRESSURE. *Journal of Sound and Vibration*, *105*, 291–308.

Velarde-Suárez, S., Ballesteros-Tajadura, R., Santolaria-Morros, C., & Pereiras-García, B. (2008). Reduction of the aerodynamic tonal noise of a forward-curved centrifugal fan by modification of the volute tongue geometry. *Applied Acoustics*, *69*(3), 225–232.

Yoon, J.-H., & Lee, S.-J. (2004). Stereoscopic PIV measurements of flow behind an isolated low-speed axial-fan. *Experimental Thermal and Fluid Science*, *28*(8), 791–802.

Yu, X.-J., & Liu, B.-J. (2007). Stereoscopic PIV measurement of unsteady flows in an axial compressor stage. *Experimental Thermal and Fluid Science*, *31*(8), 1049–1060.

Chapter 3. EXPERIMENTAL AND COMPUTATIONAL STUDY ON AN AXIAL CASE FAN FOR COOLING APPLICATIONS

Zhenyu Wang and Hui Hu

Department of Aerospace Engineering, Iowa State University

Abstract: An experimental and a numerical investigation were conducted to study the flow fields of an optimized axial fan based on a commercial-available axial fan. The PIV measurements illustrated the outer flow field of the axial fan and provided a good agreement with the 3-D numerical results by qualitative and quantitative validations. Instantaneous static pressure solutions on the rotating blades and the streamline patterns located in the rotor part depicted the details of flow characteristics in the inner region of the axial fan, which were believed to have close relationship with the aerodynamic noise generation. The time-averaged velocity and pressure solutions on the measuring plane between rotor and stator revealed the noise radiation corresponded with the turbulence kinetic energy (TKE) distributions as well as pressure fluctuations induced by the rotor-stator interaction. The airflow velocity distributions near the fan outlet were also obtained to analyze the blockage effect caused by the wire guidance channel.

3.1. Introduction

As the amount of heat generated from CPUs, graphic cards and other components in modern computers has continuously increased, which has already became a serious problem for the further development of computers. In order to find an economic and efficient way to solve this issue, small-size or miniature axial fans are widely used for cooling applications to protect the computer components overheating and ensure them working within an

appropriate temperature range. However, the size of axial fans is always restricted by the condense space for ventilation in such equipment. Hence, increasing the rotational speed of the fan is taken as the usual way to enhance the cooling ability. Although the high rotational speed could solve the cooling problem, it would also cause the high levels of noise at the same time. The noisy environment would harm human's health and also significantly decrease the working efficiency, so there is a strong demand to reduce the noise level of cooling fans, and meanwhile, maintaining their cooling ability.

The noise sources in axial fans can be categorized into the mechanical and the aeroacoustic noise, respectively (Nashimoto et al., 2004). While the aeroacoustic noise will become the dominant source when the rotational speed of axial fans keeps increasing, so the mechanical noise source can be neglected. However, the high-level noise in some axial fans is due to the poor structure design, which would deteriorate the flow performance as well as generate unnecessary noise components. As a result, the aeroacoustics levels are largely depended on the aerodynamic performance of the axial fans. If the axial fans' aerodynamic performance can be optimized then, the aeroacoustic noise may be essentially depressed. In the past two decades, extensively experimental and numerical investigations have been carried out to obtain the flow fields for further development of axial fans. Fukano et al. (2004) used two hot-wire probes rotating with the fan blades to measure the tip clearance flow in an axial fan. The results illustrated that the discrete frequency noise was due to the periodic velocity fluctuation in the blade passage. Hurault et al., (2012) obtained the steady and unsteady wall pressure fluctuations in an axial automotive cooling fan to predict the flow-induced noise by utilizing pressure sensors. As PIV technique has been matured into an effective tool in flow field measurements, a large number of investigations were

implemented by using this technique in the axial fan studies to achieve 2D and stereoscopic velocity fields (Estevadeordal et al., 2000; Yoon et al., 2004; Yu et al., 2007). The flow statistics, such as wake structures, vortices, can be precisely characterized by measuring the flow fields. However, the shortages of experimental investigations are high-investment and long-period when people try to optimize axial fans.

Recently, Computational Fluid Dynamics (CFD) tools provide another powerful and economic way to obtain more elaborate flow details than experimental measurements (Gue et al., 2012; Heo et al., 2011; Anup et al., 2014). Hase et al. (2011) used a 3-D unsteady Reynolds-averaged Navier-Stokes (URANS) model to evaluate the broadband noise of an axial fan in terms of the turbulent kinetic energy (TKE) distributions. Liu et al. (2014) carried out a numerical study to investigate the unsteady flow characteristics induced by the rotor-stator interaction. It was found that the pressure fluctuations and stator lean angles could be the main sources for the interaction noise.

More and more researchers prefer to adopt a combined method (experiment and simulation) to conduct the study on axial fan because it can shorten the time and decrease the investment and it has already been demonstrated as an efficient way in many applications. Jiang et al. (2007) did a comprehensive visualization of an axial fan flow field by CFD simulation, the tip vortex was found to play a major role in the blockage effect in the flow, which also provided a good agreement with Fukano's model for experimental investigation. Hurault et al. (2010) conducted a calculation by comparing the sweep effect between the numerical and experimental solutions. The results showed that the TKE could be a very important parameter to predict the radiated noise in turbomachinery, and the radial velocity

component should also be analyzed due to the radial equilibrium hypothesis which is often wrongly assumed.

In the present study, an experimental and a numerical study were conducted to investigate the detailed flow fields of a newly designed axial fan based on a commercially-available product. A digital Particle Image Velocimetry (PIV) system was used to conduct the outer flow field measurements to quantify turbulent flow structures around the axial fan and also provide the validation for the simulation results. A CFD work was utilized to obtain the internal flow quantities such as TKE, streamline and pressure fluctuations inside the axial fan for further analysis pertinent to the aeroacoustics and optimization.

3.2. Experimental Setup

3.2.1. The axial fan model

(a) Front view (b) Back view

Fig. 1: Axial fan model

Figure 1 illustrates the configurations of the optimized axial fan model. It should be noted that this fan was modified based on a commercially-available axial fan. The detailed modifications of this fan in comparison to the baseline fan can be found in the previous study (Wang et al., 2014). Except the motor, all the other components in this fan were redesigned

in order to achieve better flow and acoustic performance. The axial fan was made of plastics and precisely manufactured by a rapid prototyping machine.

3.2.2. PIV measurements

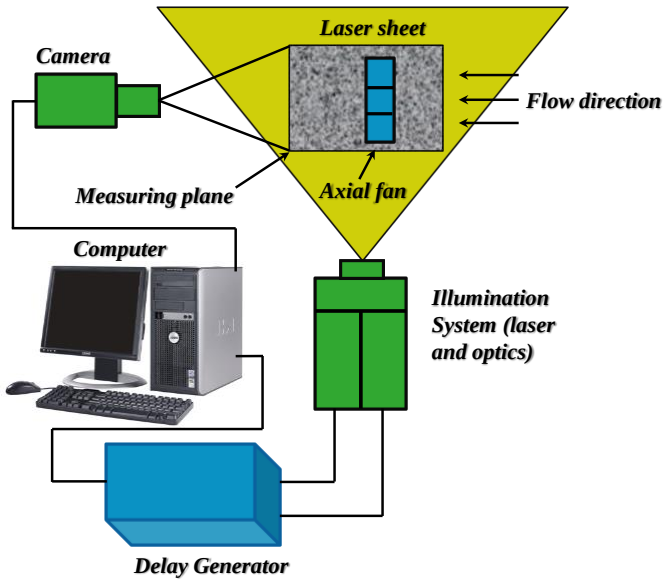

Fig. 2: PIV measurement set-up

In the present study, a high-resolution digital PIV system was used to capture the whole-field flow details around the axial fan models (shown in Fig. 2) and provide a reasonable validation for the numerical simulation. During the PIV measurements, the airflow was seeded with ~1μm oil droplets by using a fog machine (ROSCO 1900). Illumination was provided by a double-pulsed frequency-doubled Nd:YAG laser (EverGreen 200) with a pulse energy of 200 mJ at the wavelength of 532 nm. The laser beam was shaped into a sheet by a set of mirrors along with spherical and cylindrical lenses. The thickness of the laser sheet in the measurement region was about 1 mm. A high-resolution 14-bit CCD camera (PCO1600) was used for image acquisition with the axis of camera oriented perpendicular to the laser sheet. The CCD camera and the double-pulsed Nd:YAG laser were connected to a host

computer via digital delay generator (BNC565), which controlled the timing of the laser illumination and camera acquisition.

In this study, the fan was operated at the flow rate of $5m^3$/min, which represents the typical operating condition. For each tested case, 600 instantaneous frames were captured for post-processing. After PIV image acquisition, the instantaneous PIV velocity vectors were obtained from the cross-correlation with 32 × 32 pixels interrogation windows. An effective overlap of 50% of the interrogation windows was employed in the PIV image processing. The distributions of the ensemble-averaged flow quantities were calculated from the data after image processing.

3.3. Numerical methods

The PIV measurements only provide the flow details outside of the axial fan, but the flow statistics inside the fan are more important to give a further understanding for the noise radiation. However, due to the complicated geometry of the axial fan, it is difficult to visualize the internal flow field of the axial fan by using PIV technique. Hence, numerical method would be a more realistic way to get an insight into the flow structures in the fan model. In the present study, the 3D URANS (Unsteady Reynolds Averaged Navier-Stokes) model was implemented through the commercially-available solver, ANSYS/FLUENT to simulate the flow field of the axial fan. URANS model is an economic and effective tool that offers reasonable results, which was widely used in the investigations of axial fan studies (Akturk et al., 2009).

3.3.1. Governing equations

The fluid dynamics in the present axial fan is an incompressible, three-dimensional and fully turbulent flow, which is generally expressed by the Navier-Stokes equations in Cartesian tensor notation as follows:

Continuity

$$\frac{\partial u_i}{\partial x_i} = 0 \tag{1}$$

Momentum

$$\frac{\partial(\rho u_i)}{\partial t} + \frac{\partial(\rho u_i u_j - \tau_{ij})}{\partial x_j} = -\frac{\partial p}{\partial x_i} + S_i \tag{2}$$

where u_i and u_j are the velocity components of the air flow, ρ is the air density, p is the pressure, τ_{ij} is the Reynolds stress component and S_i is the momentum source.

3.3.2. Computational domain and mesh generation

Figure 3(a) shows the computational domain for the simulated axial fan model. In order to minimize the effects from the boundary, the inlet and outlet boundaries were extended to 5D and 8D away from the fan, respectively. Figure 3(b) illustrates the mesh used for the present calculation. Because of the complicated blade geometry, the unstructured mesh was used and prism layers were also adapted near the wall to enhance the accuracy of the flow field. The rest of regions in the calculation domain were generated with fine structural meshes to reduce the timing and boost the precision of calculation. Figure 4 depicts the grid independence study by using the area-weighted average total pressure on the stator outlet under different cell sizes. It can be clearly seen that the total pressure would increase along the mesh number increases. However, when the number of cells was over 3.5 million, the total pressure became leveled off. Therefore, 3.5 Millions cells were used in this study, which

would be a reasonable mesh size to converge all the flow quantities for the sake of economy and accuracy.

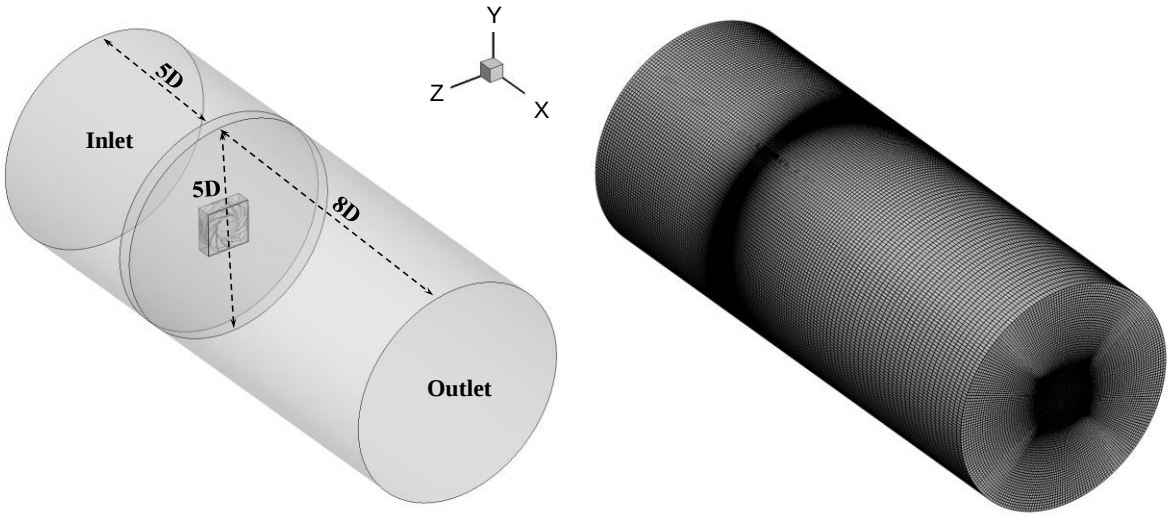

(a) Computational domain (b) Mesh used in the calculation

Fig. 3: Computational domain and mesh

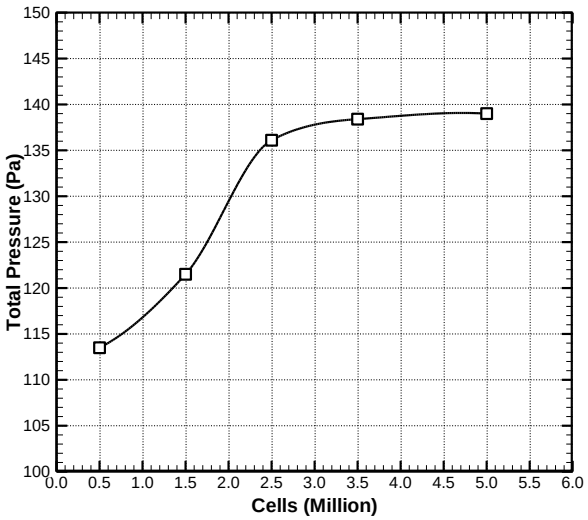

Fig. 4: Grid independence study

3.3.3. Computational methods and boundary conditions

A turbulence model is needed to be used in turbomachinery simulation because it is almost impossible to calculate the flow field directly. Since the flow in the present axial fan model is a fully turbulent and is dominated by the rotating flows, a two-equation turbulence

model of the Renormalization Group (RNG) *k-ε* type was used to offer a better prediction compared with the standard *k-ε* turbulence model (Heo et al., 2011; Liu et al., 2010). Although, there are many other turbulence models have been successfully applied in the simulation of axial fan flow including realizable *k-ε* model (Li et al., 2014), *k-ω SST* model (Borges et al., 2015) and Reynolds stress model (Hurault et al., 2010; Lu et al., 2007), after comparing with the flow field results obtained from the PIV measurements, it was found that the *k-ε* RNG model can provide a better prediction than other turbulence models.

In order to decrease the requirement on computational resources, the boundary conditions were specified close to the real operating condition because it can save the heavy demand on the computational resources for a large computational domain (Lu et al., 2007). As the outer flow field of the fan axial can be attained by the PIV measurements, the flow rate of the axial fan can be roughly calculated through the velocity field. Therefore, mass flow rate boundary condition was defined for the fan inlet, and then the atmospheric static pressure was selected as the outlet boundary condition. The computational domain was divided into rotational region and stationary region, which contained the rotor part and the others, respectively. Interfaces were implemented between the rotating and stationary parts in order to capture the transient flow variables that can be transferred between each other through the meshes from different regions. The wall surfaces were defined as "adiabatic, non-slip" condition associated with wall functions for the velocities.

During the simulation, steady solutions were calculated firstly to provide a reasonable initial flow field for the transient calculation to save the computational resources and ensure the accuracy. The "Semi-Implicit Method for Pressure Linked Equations-Consistent" (SIMPLEC) algorithm was used to couple the pressure and velocity fields, which can

enhance the convergence in the computation of the rotating flows (Li et al., 2014). The Moving reference Frame (MRF), which has been widely used for turbomachinery applications, was applied in the rotor region to exchange the flow characteristics with the stationary regions through the interfaces. The simulation was switched to transient computation when the flow quantities in the steady calculation became stable. It should be noted that "Pressure implicit with splitting of operator" (PISO) algorithm was applied in the unsteady calculation for the pressure-velocity corrections, due to large time steps and lesser computing efforts can be performed in the computation (Issa et al., 1986). Hence, large time steps (e.g., 10^{-3}s) were used at the beginning of the computation, and then the time step was decreased to a small gap (e.g., 10^{-5}s) for fine calculation as the flow characteristics stabilized gradually. Finally, a total of 360 time steps were used for one rotational cycle for the unsteady flow calculation, which means the blades would rotate 1 degree for each time step. Sliding mesh was used to capture the transient flow details between rotating region and stationary regions. A second-order upwind scheme was also implemented for the discretization of convective terms, diffusive terms and turbulent viscosity terms.

3.4. Results and Discussions

The PIV measurement obtained the outer ensemble-averaged velocity fields of the test fan, which can also offer an authentic validation for the computational solutions and provide a complement for the simulated results. It should be noted that the axial fan was operated at the same rotational speed during the PIV measurements and simulations, and the computational model was a full scale three-dimensional flow fields and no simplification was assumed.

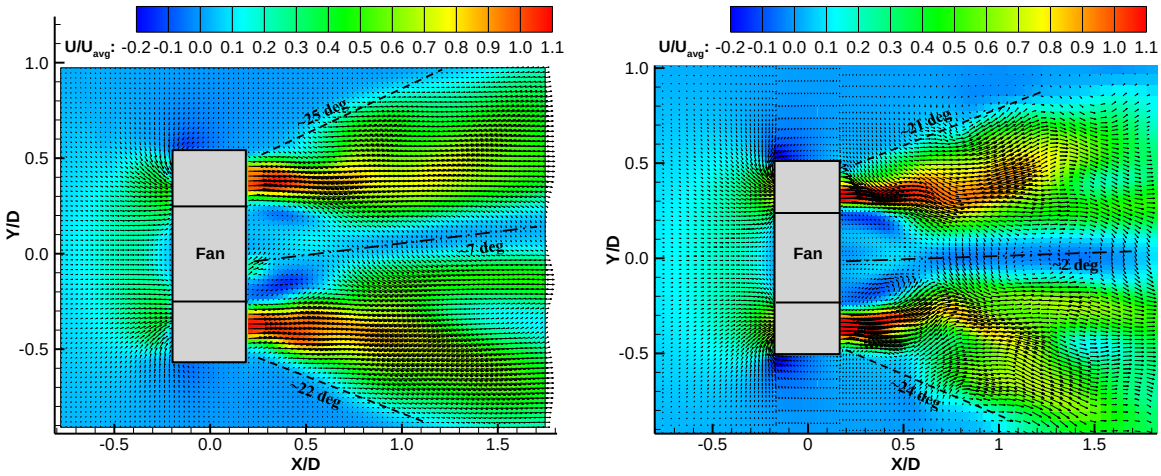

Fig. 5: Ensemble-averaged velocity distributions on the same measuring plane from experiment (left) and simulation (right)

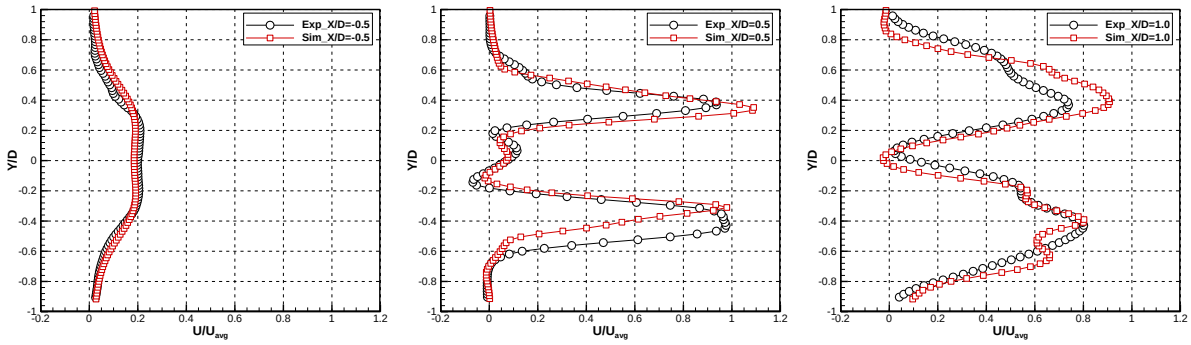

(a) X/D=-0.5 (b) X/D=0.5 (c) X/D=1.0

Fig. 6: Ensemble-averaged streamwise velocity profiles

Figure 5 illustrates the ensemble-averaged velocity comparisons between the experimental results and the numerical solutions at the same 2-D central measurement plane. The flow structures and the contours of the velocity magnitude, derived from the computational solutions match very well with the experimental results. There is a recirculation region, namely, low-momentum airflow region for both of them occurs near the motor region due to high velocity gradient existing in the shear layer. this phenomenon was also illustrated in Yoon et al.'s (2004) work when they investigated a low-speed axial fan by using a stereoscopic PIV measurement. The low-momentum air flow region is tilted upward

about 7 deg in the wake of the experimental case, but the tilted angle is found to be only around 2 deg in the simulation case. The expansion angle for the upper stream in the experimental results is about 25 deg in comparison to a smaller angle of 21 deg in the simulation solutions, but the lower stream in the simulation solution shows a larger tilted angle than that of the experimental results.

In order to quantitatively compare the velocity fields between the experimental and numerical solutions, the transverse velocity profiles at three locations (i.e., X/D=-0.5,X/D=0.5 and X/D=1.0) were extracted from the PIV results and simulations. Figure 6 demonstrates the transverse velocity distributions on the measuring locations. The velocity is normalized by the averaged velocity U_{avg} that is calculated by the flow rate divided by the flow passage area of the axial fan (U_{avg}=Q/A) in the flow passage. As shown in the plot, the calculated velocity distributions at X/D=-0.5, which represents the location in front of the fan inlet, agrees very well with that from the experiment results. Only a small discrepancy exists on the velocity peak values. The velocity distributions on the lower stream and central region behind the rotor in the numerical simulations match nicely with the experimental results at the location of X/D=0.5. A slight over-prediction for the airflow width is found in the upper stream of the simulated results. However, the velocity distribution at the position of X/D=1.0 doesn't show a similar trend as the previous two locations. A secondary velocity-crest is observed in the lower stream through the experiment which is absent from the simulation results. Overall, it can be concluded that the width and flow structures in the wakes between experiment and calculation are within a reasonable range for prediction, and this quantitative comparison can offer the confidence for analyzing the flow fields accurately inside the axial fan.

Figs.5 and 6 have showed the outer flow fields of the axial fan, but the internal flow of the axial fan, which contributes the main aeroacoustic source such as the tip leakage vortex and the passage vortex (Lu et al., 2007) and rotor-stator interaction (Laurent et al., 2011), still hasn't uncovered in relation to the noise generation. Hence, the inner flow fields should be achieved for further analysis due to its importance on the aeroacoustics of the axial fan. Figure 7 illustrates the instantaneous pressure coefficient ($C_P = \frac{P_{static}}{0.5\rho u_{avg}^2}$) distributions on the suction surface of the rotating blades in one revolution with a phase angle interval of 60 degrees. In the present simulation, there are 7 identical blades that would rotate in anti-clockwise direction, and the blade position shown in Fig. 7(a) is identified as the initial phase angle (i.e., Phase angle = 0 deg). As expected, it can be easily found that the high negative pressure regions appear close to the blade tip, which indicates that the air flow is accelerated to the highest level in rotary region. However, the static pressure on the blade surface increases gradually towards the trailing edge of the blade, which can be inferred as a suppression of airflow along the streamwise. This could be induced by the tip vortex that plays a major role in the flow fields near the blade tip (Jiang et al., 2007), and has a large blockage effect to the airflow. As mentioned above, the flow field in the stator cannot be treated as an axial-symmetric since wires extruded from the rotor part to the fan casing. When the blade rotates closer to guide channel, the static pressure near the tip region is increased to some extent compared with the blade on other phase angles, which can be inferred that the airflow is restricted by the blocking effect of the guide channel. However, there is no significant effect on the static pressure distributions near the blade trailing edge caused by the stators in comparison to Lu et al.'s (2007) findings, as more stator struts can

decrease the instantaneous pressure fluctuations due to relative motion between rotor and stator.

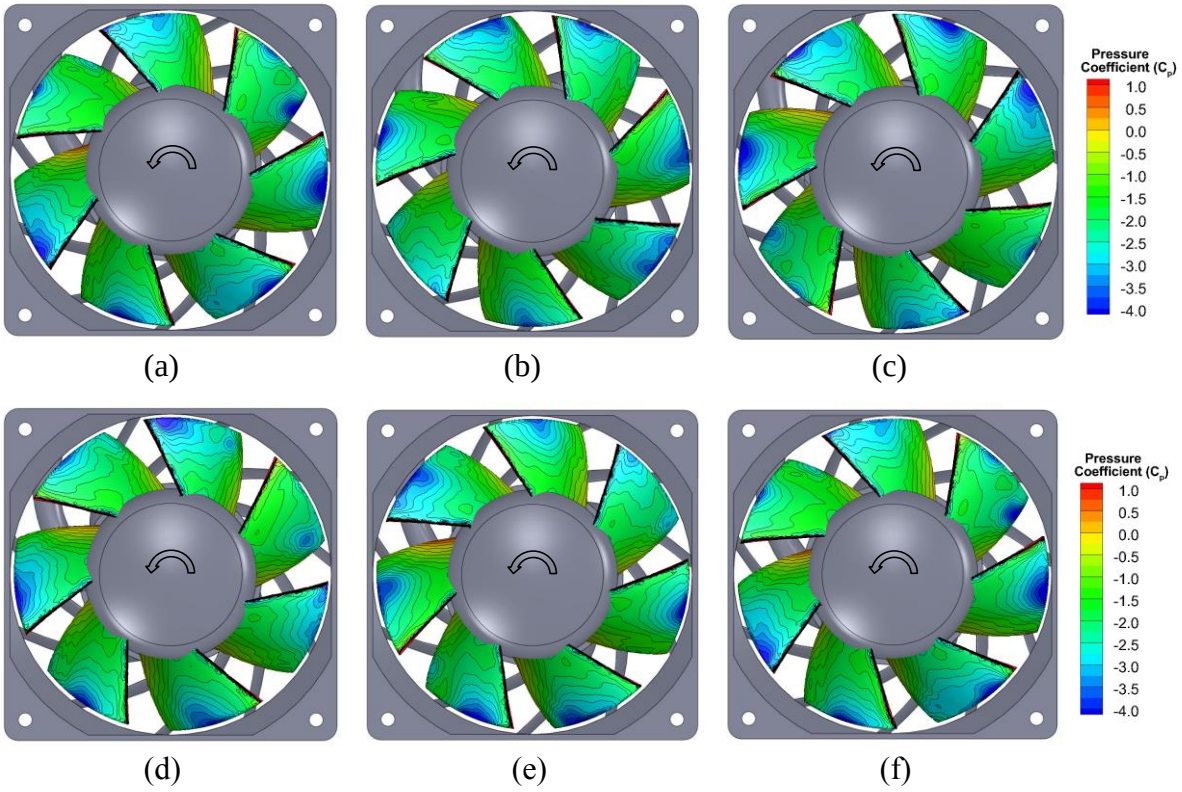

Fig. 7: Instantaneous static pressure coefficient distributions on the blade suction surface. (a) Phase angle = 0deg, (b) Phase angle = 60deg, (c) Phase angle = 120deg, (d) Phase angle = 180deg, (e) Phase angle = 240deg, (f) Phase angle = 300deg.

In order to capture the flow characteristics inside the axial fan, three planes, as shown in Fig. 8, were extracted from the numerical solutions for revealing a detailed investigation. Plane #1 was selected right in the rotary region and plane #2 was arranged between the rotor and stator where could reveal the severe interactions caused by the rotating blades and the stationary guide vanes. Plane #3 was selected to reflect the downstream flow fields at the fan outlet. It should be noted that, since this simulation is an unsteady calculation, the instantaneous flow quantities can be visualized on plane #1 and the time-averaged results can be recorded on plane #2 as well as plane #3.

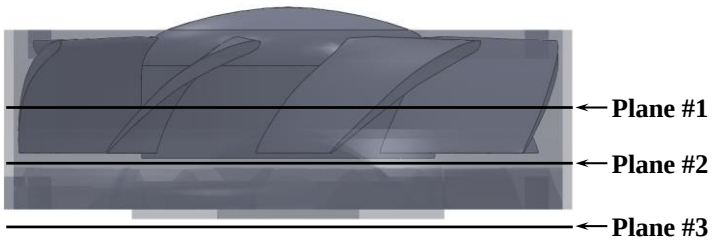

Fig. 8: Measuring planes

Figure 9 illustrates the instantaneous streamline patterns between neighboring rotor blades with a phase angle of 60 degrees on the measuring plane #1, which is visualized to investigate the flow statistics such as the tip leakage vortex and passage vortex in the rotary region. According to the study conducted by Li et al. (2014), blade tip clearance variation would significantly affect the leakage flow distribution. Compared to the tip clearance in the original axial fan (Wang et al., 2014), the gap was shrunk from 1.5mm to 1.0mm in the optimized axial fan. However, there is no conspicuous tip vortex that occurs under this flow condition according to the results illustrated in Fig. 8, which demonstrates that the spacing of tip clearance is an appropriate value in this newly designed axial fan. The elliptical cycles highlighted in the figures demonstrate the unsmooth flow, namely, vortices appear in the flow passages. The reasons for this phenomenon could be inferred as the flow rate being only 50% of the full scale or the airflow inside the fan having a slight separation from the blade surface due to inappropriate design such as blade angle of attack or stagger angle arrangement on the rotating blades. The unsmooth flow which occurs in the blade passage would also induce unnecessary noise emission from the fan. In addition, it should be noted that most of the unsmooth streamlines appear in the middle region of flow passage close to the suction surface, which point out the positions need to be taken into account for further optimization. The stator structures near the upper-right corner of the fan frame should be optimized

because the vortex is almost always generated when the blades rotate through this region. It is believed to be induced by the unreasonable design on the stator and produced unnecessary noise source propagating from the rotor-stator interactions.

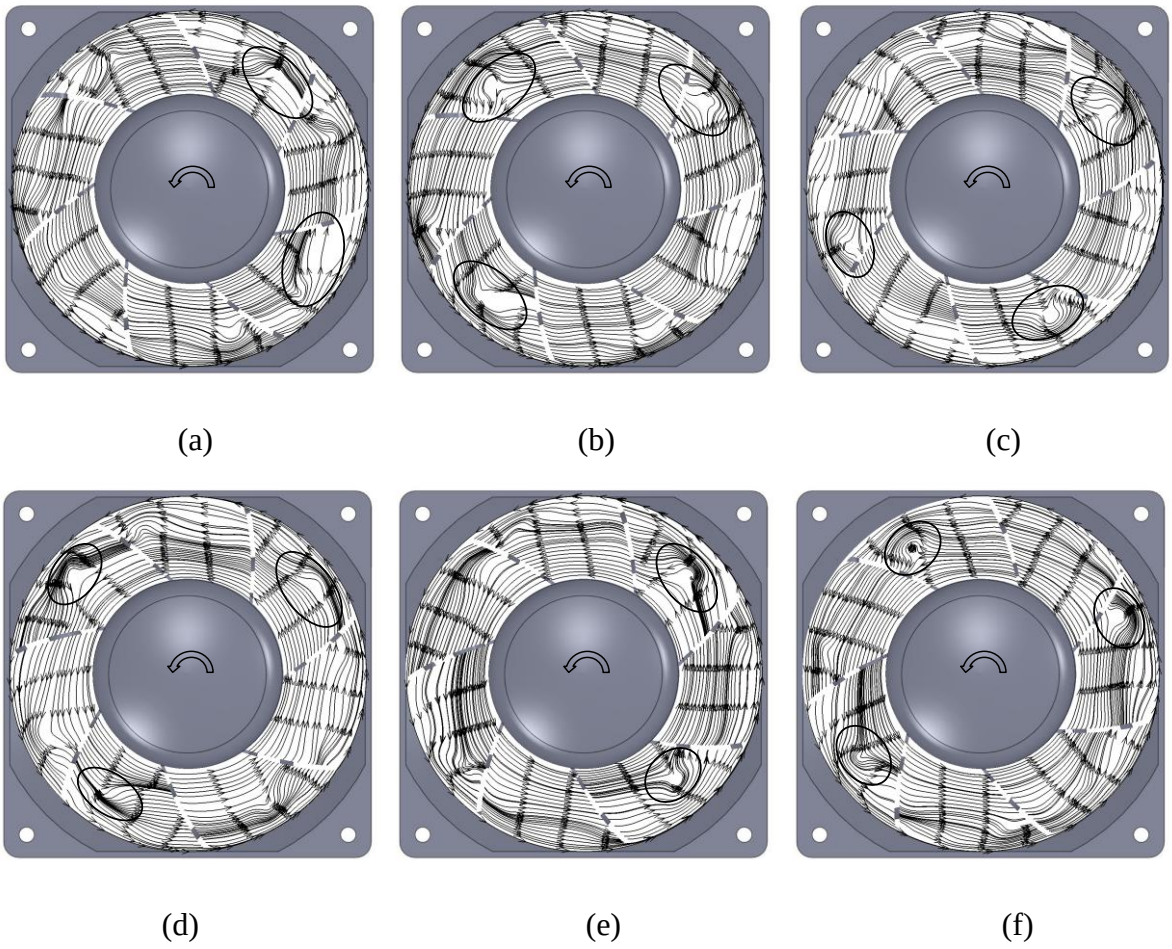

Fig.9: Instantaneous streamline distributions in the flow passages on measuring plane #1. (a) Phase angle = 0deg, (b) Phase angle = 60deg, (c) Phase angle = 120deg, (d) Phase angle = 180deg, (e) Phase angle = 240deg, (f) Phase angle = 300deg.

Rotor-stator interaction noise has been identified as one of the most important sources in modern turbomachinery. Hence, the flow characteristics between rotor and stator need to be revealed to elucidate the noise generation. Instead of predicting the broadband noise directly, Heo et al. (2011) and Hase et al. (2011) found that the turbulent kinetic energy (TKE), which was originated by random turbulence behavior, can represent the magnitude of broadband

noise sources in the study of centrifugal and axial fans, respectively. Fig. 10(a) illustrates the time-averaged normalized TKE distributions on the measuring plane #2. TKE levels are not uniformly distributed in the circumferential direction and the high values are observed in the corner regions close to the blade tip, which points out the locations of the noise sources caused by the rotor-stator interactions. While the low TKE levels in the central region of the flow passages may have less importance for the rotor-stator noise generation. In addition, as the aeroacoustics in axial fan is intrinsically generated by pressure fluctuations in the flows, the variation of the static pressure between the rotor and stator is also a significant characteristic for further analysis. Fig. 10(b) depicts the contour of pressure fluctuations (ΔC_p) on the measuring plane #2, which is defined as follows:

$$\Delta C_p = \frac{\sqrt{\frac{1}{N}\sum (P_i - \bar{P})^2}}{\frac{1}{2}\rho u_{avg}^2} \tag{3}$$

Where N is the number of data point, P_i is the instantaneous static pressure on each measuring phase angle, $\bar{P}$ is the time-averaged static pressure and u_{avg} is the averaged streamwise velocity in the flow passage.

As expected, the most intense pressure fluctuations would be associated with the high TKE levels in the corner regions approaching to the blade tip, and low TKE levels are concentrated in the central region, which was also observed in the study performed by Liu et al. (2014) when they investigated the rotor-stator interaction noise in a turbo fan. Several intensive spots that occur in the high pressure fluctuation regions, which may be caused by the severe rotor-stator interaction as well as the existence of a strong shear layer between the high-speed airflow in the passage and casing surface. Recall the streamline distributions in Fig. 9, it can be easily found that the regions with high amplitude TKE and pressure

fluctuations on the measuring plane #2 correspond with the regions with unsmooth streamlines on the measuring plane #1 in the same spanwise direction. This may indicate that the flow separations occur in rotary regions would induce high TKE levels and pressure fluctuations. The high TKE levels and pressure fluctuations would propagate to downstream locations and then increase the rotor-stator interaction noise.

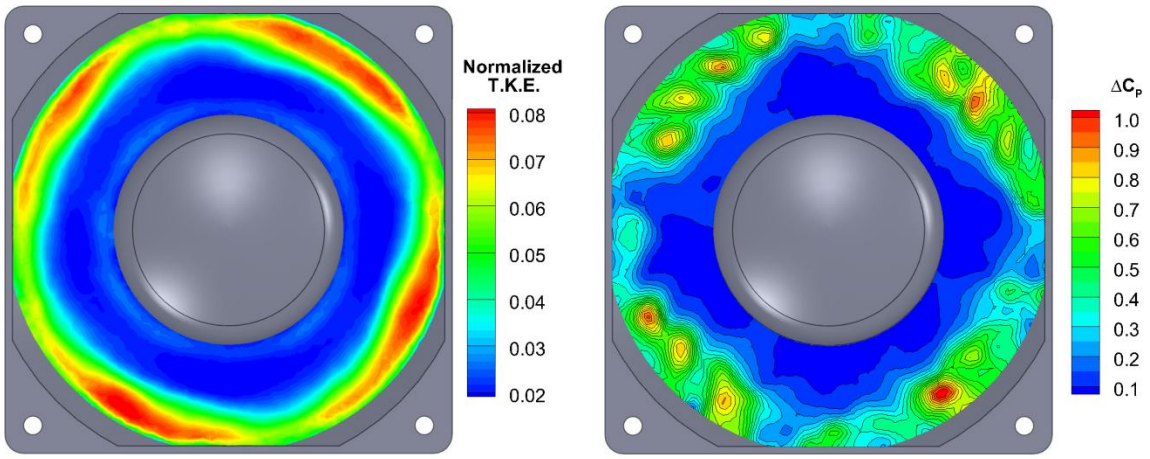

(a) Normalized T.K.E. (b) Pressure fluctuations

Fig. 10: Time-averaged flow quantities distributions on the measuring plane #2

Figure 11 shows the ensemble-averaged velocity distributions on the measuring plane #3, located right behind the fan outlet. Compared to the experimental and numerical solutions illustrated in Fig.5(a), the out-of-plane velocity (*v*, *w*) can be captured as a supplement for the previous streamwise velocity results. Similar to the results characterized by Jiang et al. (2007), the highest axial velocity is observed in the half way through the blade span. Wave-shape flow structures are found in the circumferential directions due to the uniformly installed stator vanes. Except the region near the guidance channel, the axial velocity is almost evenly distributed behind the blade passage along this direction. The size of the guidance channel should be minimized to reduce the noise caused by the blockage effects.

The air flow would rotate in the anti-clockwise direction and entrain the outside air into the main stream when emanating from the fan stators.

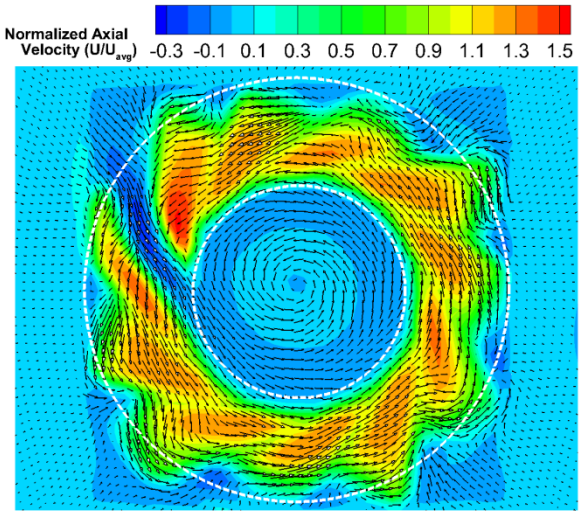

Fig. 11: Time-averaged velocity distributions on measuring plane #3

3.5. Conclusions

An experimental and a numerical study were conducted to investigate the flow fields of an optimized axial fan based on a commercial-available fan. By qualitatively comparing the flow structures and quantitatively comparing the velocity distributions, it was found that the PIV measurements agreed well with the simulation solutions and provided the necessary confidence for analyzing the flow fields inside the axial fan. The instantaneous pressure solutions represented the high negative pressure region on the blade surface near the blade tip, which indicated the air flow was accelerated to the highest level in the rotor region. When the blade rotated closer to the guide channel, the static pressure near the tip region was increased to some extent compared with the blade on other phase angles.

The instantaneous streamline patterns demonstrated the unsmooth flow paths occurred in the flow passages, which could be caused by the severe interaction between the blades and

stators or inappropriate design such as angle of attack or stagger angle in the rotor. It could induce unnecessary noise emit from the fan by the reasons such as boundary layer separation from the blade surface. The time-averaged normalized TKE distributions and static pressure fluctuations caused by rotor-stator interaction indicated that the locations of the noise sources, and also the flow separations occurred in rotary regions would be associated with high TKE and pressure fluctuations in the downstream wake.

ACKNOWLEDGMENTS

The support from Iowa Alliance for Wind Innovation and Novel Development (IAWIND) and National Science Foundation (NSF) under award number of CBET-1133751 is gratefully acknowledged. The authors also want to thank Jerry Xu of Futurewei for help and useful discussions related to the present study.

References

Akturk. Ali, Shavalikul. Akamol, C. C. (2009). PIV Measurements and Computational Study of a 5-Inch Ducted Fan for V/STOL UAV Applications. *47th AIAA Aerospace Sciences Meeting*, (January), 1–17.

Borges, S. S., Zdanski, P. S. B., & Barbieri, R. (2015). A hybrid analytical/experimental model for evaluation of the aerodynamic noise in fans. *Applied Acoustics*, *90*, 81–87.

Estevadeordal. J, S.Gogineni, W.Copenhaver, G.Bloch, M. B. (2000). Flow field in a low-speed axial fan : a DPIV investigation. *Experimental Thermal and Fluid Science*, *23*, 11–21.

Fukano, T., & Jang, C.-M. (2004). Tip clearance noise of axial flow fans operating at design and off-design condition. *Journal of Sound and Vibration*, *275*(3-5), 1027–1050.

Gue, F., Cheong, C., & Kim, T. (2012). Development of low-noise axial cooling fans in a household refrigerator. *Journal of Mechanical Science and Technology*, *25*(12), 2995–3004.

Hase, T., Yamasaki, N., & Ooishi, T. (2011). Numerical simulation for fan broadband noise prediction. *Journal of Thermal Science*, *20*(1), 58–63.

Heo, S., Cheong, C., & Kim, T.-H. (2011). Development of low-noise centrifugal fans for a refrigerator using inclined S-shaped trailing edge. *International Journal of Refrigeration*, *34*(8), 2076–2091.

Hurault, J., Kouidri, S., & Bakir, F. (2012). Experimental investigations on the wall pressure measurement on the blade of axial flow fans. *Experimental Thermal and Fluid Science*, *40*, 29–37.

Hurault, J., Kouidri, S., Bakir, F., & Rey, R. (2010). Experimental and numerical study of the sweep effect on three-dimensional flow downstream of axial flow fans. *Flow Measurement and Instrumentation*, *21*(2), 155–165.

Jiang, C., Chen, J., Chen, Z., Tian, J., OuYang, H., & Du, Z. (2007). Experimental and numerical study on aeroacoustic sound of axial flow fan in room air conditioner. *Applied Acoustics*, *68*(4), 458–472.

KC, A., Thapa, B., & Lee, Y.-H. (2014). Transient numerical analysis of rotor–stator interaction in a Francis turbine. *Renewable Energy*, *65*, 227–235.

Li, C., Li, X., Li, P., & Ye, X. (2014). Numerical investigation of impeller trimming effect on performance of an axial flow fan. *Energy*, *75*, 534–548.

Liu, H., Ouyang, H., Wu, Y., Tian, J., & Du, Z. (2014). Investigation of Unsteady Flows and Noise in Rotor-Stator Interaction with Adjustable Lean Vane. *Engineering Applications of Computational Fluid Mechanics*, *8*(2), 299–307.

Liu, S. H., Huang, R. F., & Lin, C. A. (2010). Computational and experimental investigations of performance curve of an axial flow fan using downstream flow resistance method. *Experimental Thermal and Fluid Science*, *34*(7), 827–837.

Lu, H. Z., Huang, L., So, R. M. C., & Wang, J. (2007). A computational study of the interaction noise from a small axial-flow fan. *The Journal of the Acoustical Society of America*, *122*(3), 1404.

Nashimoto. A, Fujisawa. T, A. T. (2004). Measurements of Aerodynamic Noise and Wake Flow Field in a Cooling Fan with Winglets. *Journal of Visualization*, *7*(1), 85–92.

R. Issa, A.Gosman, A. W. (1986). The Computation of Compressible and Incompressible Recirculating Flows by a Non-iterative Implicit Scheme. *Journal of Computational Physics*, *82*, 66–82.

Soulat. Laurent, Stephane. Moreau, H. P. (2011). Wake Model Effects on the Prediction of Turbulence-Interaction Broadband Noise in a Realistic Compressor Stage. *41st AIAA Fluid Dynamics Conference and Exhibit*, (June), 1–18.

Wang, Z., & Hu, H. (2014). Development of an Ultra-quiet Fan for Computer Cooling Applications. *Proceedings of the ASME 2014 4th Joint US-European Fluids Engineering Division Summer Meeting*, 1–10.

Yoon, J.-H., & Lee, S.-J. (2004). Stereoscopic PIV measurements of flow behind an isolated low-speed axial-fan. *Experimental Thermal and Fluid Science*, *28*(8), 791–802.

Yu, X.-J., & Liu, B.-J. (2007). Stereoscopic PIV measurement of unsteady flows in an axial compressor stage. *Experimental Thermal and Fluid Science*, *31*(8), 1049–1060.

CHAPTER 4. A NOVEL TWIN-ROTOR WIND TURBINE DESIGN FOR IMRPOVED TURBINE PERFORMANCE AND WIND FARM EFFICIENCY

Zhenyu Wang, Ahmet Ozbay, Wei Tian, Anupam Sharma, Hui Hu

Department of Aerospace Engineering, Iowa State University

Abstract: An experimental study was performed to examine the wake characteristics and aeromechanic performance of an innovative twin-rotor wind turbine (TRWT), which has an extra set of smaller, auxiliary rotor blades appended in front of the main rotor blades, in comparison with those of a conventional single-rotor wind turbine (SRWT). The comparative study was conducted in a large-scale Aerodynamic/Atmospheric Boundary Layer (AABL) wind tunnel with the scaled TRWT and SRWT model sited in simulated atmospheric boundary layer (ABL) winds under neutral stability conditions. In addition to measuring the dynamic wind loads acting on the wind turbine models, a high-resolution PIV system and a Cobra Probe Anemometry were used to attain the wake flow quantities behind the turbine models. The power outputs of a duplicate model turbine operating in the wakes behind the TRWT and SRWT models at different downstream locations were also measured and compared quantitatively. The measured results reveal clearly that the TRWT design is capable of harnessing more wind energy from the same incoming airflow by reducing the roots losses incurred in the region near the roots of the main rotor blades, which also result in much higher velocity deficits in the near wake behind the TRWT model as well as much greater dynamic wind loads acting on the TRWT models, in comparison with those of the SRWT model. Due to the existence of the auxiliary rotor appended in front of the main rotor, more complex vortex structures were found to be generated in the wake behind the TRWT

model, which would significantly enhance the turbulent mixing in the wake flow and facilitate a much faster recovery of the velocity deficits in the far wake behind the TRWT model. As a result, the TRWT design was found to enable downstream wind turbine sited in the TRWT wake to generate more power than that in the SRWT wake by mitigating the wake losses. The detailed flow field measurements were correlated with the dynamic wind loads and power output measurements to elucidate the underlying physics to explore/optimize design paradigms for higher total power generation and better durability of the wind turbines.

4.1. Introduction

Conventional horizontal axis wind turbine (*HAWT*) design is the predominant design for utility-scale wind turbines in nowadays, it has one singular rotor is used and the rotor blades are aerodynamically optimized in the outboard sections. However, the sections near the blade root are primarily designed for sustaining structural loads (i.e., bending and torsion). Thus, extremely high thickness-to-chord airfoils, which have poor aerodynamics, are utilized in this section to afford structural integrity. Such a configuration results in a significantly weak wind energy harvest zone near the root of the turbine. As we know, by applying conservation law in one-dimension, a maximum limit (Betz limit) of 0.593 can be achieved for the power coefficient (C_P). But this limit is misleading because it assumes there is no wake swirling and viscous losses and with infinite number of rotor blades. If these assumptions are removed, the maximum C_P potential of a typical *HAWT* is close to 0.53 (Okulov et al., 2008; Sharma et al., 2010). The distinction between the Betz limit and the measured peak performance of modern *HAWT*s is due to several constraints, one important of which is the losses in the root region (approximately bottom 25% of rotor blades). Flow separation in the root region causes span-wise (cross) flow, which would also deteriorate the aerodynamic performance of the

outboard blade sections (Rosenberg et al., 2014). Up to 5% loss in wind energy extraction is estimated to occur per turbine for the compromise of structural constraint (Sharma et al., 2010). The importance of these losses is enormous especially when contrasted with the electric power generated per year in the world from wind turbines.

Recently, people recognized that wind turbines could not be investigated as operating in isolation since utility-scale turbines are always deployed in clusters. The downstream wind turbines that are located in the near- and far-wake regions of upstream turbines in typical wind farm settings would experience significantly different incoming surface wind profiles in comparison to the ones located upwind due to the interferences of the wake flows of the upwind turbines. Since a portion of the wind energy carried by the incoming surface wind has already been harvested by the upstream wind turbines, significant velocity deficits would be generated in the wake flows behind the upstream turbines. Therefore, the aerodynamic interaction/interferences from upstream turbines, which are usually called wake losses, have been found to be in the range of 20%-40% (Barthelmie et al., 2007a). The primary mechanism of the wake losses is due to the ingestion (by downstream turbines) of low-momentum wake flow of upstream turbines. The range of the wake losses is exceptionally wide because of their strong dependence on the factors such as farm location, layout, and atmospheric stability conditions.

As described in the paper of Vermeer et al., (2003), the wake behind a wind turbine can be typically divided into a near wake and a far wake. The near wake refers to the region from the turbine to approximately one rotor diameter downstream. The near wake structures would be essentially influenced by the number of blades, blade aerodynamics such as attached or stalled flows, 3-D effects and tip vortices due to the existence of the rotor. The far wake is

the region beyond the near wake, where the actual rotor shape is less important, and the main attentions to far wake flows are usually drawn in wake models, wake interferences, turbulence models and topographical effects. Chamorro et al. (2011), Hu et al. (2012) and Yang et al. (2012) investigated the evolution of the unsteady vortex and turbulent flow structures in the near wakes of the wind turbine models placed in atmospheric boundary layer airflows with rather high turbulence intensity levels. Based on the field measurements in offshore wind farms, Barthelmie et al. (2003) reported that, with spacing between the wind turbines in the offshore wind farms being 1.7D to 7.4D, the wake velocity deficit recovery that can be achieved was in the range of 10% to 45%. They also found that the wake velocity deficit would recover very slowly when the spacing exceeds 6.5D. Tian et al. (2014) also conducted an experiment to examine the effects of turbulence level of the incoming ABL winds on the recovery rate of the wake velocity deficits behind wind turbines. They observed that the wake velocity deficits would recover much faster with a higher turbulence level in the incoming flow (i.e., for the cases in typical onshore wind farms), compared with that with relatively low turbulence level in the incoming airflow (i.e., for the cases in typical offshore wind farms).

In comparison to large amounts of work dedicated to predict and measure wake losses, relatively very little research has focused on reducing wake losses. Single-rotor wind turbine (*SRWT*) wake characteristics and wind farm (composed of *SRWT*s) wake characteristics have been comprehensively investigated by using experimental and numerical techniques. Experiments have ranged from miniature laboratory scale to real field measurements aiming both singular and wind farm wake aerodynamics. Adaramola et al. (2011) found that the reduction in the maximum power coefficient of the downstream turbine is strongly dependent

on the distance between the turbines and the operating condition of the upstream turbine, and then by operating the upstream turbine in yawed condition, the harvest in total power output from the two turbines could be increased by about 12%. Barthelmie et al. (2010) did a real field measurement at the Nysted offshore wind farm to evaluate the wind farm efficiency and wind turbine wakes. They quantified that the wake losses are most strongly pertinent to wind speed variation through the turbine thrust coefficient, and wind direction, turbulence and atmospheric stability as important second order effects. Later, Hansen et al. (2012) analyzed statistical data about wind turbine operational characteristics, power measurements and meteorological measurements from Horns Rev offshore wind farm at Denmark. It was found that stable conditions tend to be associated with lower levels of turbulence intensity and this relationship persists as wind speed increase. In addition, power deficit is a function of ambient turbulence intensity and is strongly dependent on the wind turbine spacing: as turbulence intensity increases, the power deficit decreases. Hu et al. (2012) used a high-resolution digital particle image velocimetry (PIV) to quantify the characteristics of the turbulent vortex flow in the near wake of a horizontal axis wind turbine model. They performed "free-run" measurements to determine the ensemble-averaged statistics of the flow quantities such as mean velocity, Reynolds stress and turbulence kinetic energy (TKE) distribution in the wake flow and also used "phase-locked" measurements to elucidate further details about the evolution of the unsteady vortex structures in relation to the position of the rotating turbine blades in the downstream wake flow. Varshney (2012) employed quantitative digital PIV and qualitative dye flow visualization technique to investigate the helical tip vortices in the wake of a wind turbine model. It was found that the helical vortex core size was increasing with downstream distance and the normalized streamwise component of the

wake velocity decreased with increasing tip speed ratios. Chamorro et al. (2010) used a customized triple wire anemometer to conduct high-resolution velocity and temperature measurements to characterize the mean velocity, turbulence intensity, turbulent flux and spectra at different locations in the wake. The effect of the wake on the turbulence statistics is found to extend as far as 20 rotor diameters downstream of the turbine. Also, the velocity deficit shows a nearly axisymmetric shape but the turbulence intensity distribution illustrates as non-axisymmetric due to the non-uniform distribution of the incoming velocity in the boundary layer. Zhang et al. (2013) employed stereoscopic PIV to visualize the shedding of tip vortices and triple wire anemometry to acquire profiles of the mean flow, turbulence intensity, turbulent momentum and heat flux at downstream locations from 2-20 rotor diameters in the center plane of the wake in a simulated convective boundary layer and a neutral boundary layer. From the comparison results, a smaller velocity deficit (about 15% at the wake center) in the convective boundary layer is observed in comparison with the wake in the neutral boundary layer, which is because an enhanced radial momentum transport leads to a more rapid momentum recovery. However, the velocity deficit at the wake center decays following a power law regardless of the thermal stability.

Due to cost considerations, multi-stage designs (e.g., dual-rotor turbines) on *HAWT* have received little concern. Multi-stage turbomachineries are widely used in gas turbine and propulsion industries in order to maximize the efficiency of fossil fuel usage. Since the "fuel" for wind turbines in nature is supposedly free, the cost of electricity production, instead of efficiency, leads to current wind turbine designs. With the concerns that we will run out of sites (land or ocean) where we can realistically install wind turbines, the focus has to therefore shift towards efficient turbine and wind farm designs that harvest higher power per

square meters of surface area. Betz limit is just applicable for *SRWT*s, while multi-stage rotors can surpass this limit. Newman (1986) calculated that the maximum C_p that an identical size dual-rotor wind turbine (*DRWT*) could reach was 0.64, almost an 8% increase compared to the Betz limit. But further addition of rotor stages would give diminishing returns. Windpower Engineering & Development have designed a co-axial, twin-rotor wind turbine (*TRWT*) with the objective of harvesting more energy at lower wind speeds. They used two identical-sized rotors connected by one shaft to a variable-speed generator, but this twin-rotor application focused on improving energy harvesting rather than reducing losses.

In the present study, a novel twin-rotor wind turbine (a big main rotor tailored with a small auxiliary rotor on the same shaft) was designed aiming to reduce root losses and also reduce wake losses in a wind farm through the enhanced wake mixing. In addition to measuring the dynamic wind loads acting on the model turbine, the detailed velocity measurements are performed by using intrusive (Cobra-probe) and non-intrusive (2-D and stereoscopic PIV) measurements in a neutral atmospheric boundary layer flow to quantify the turbine wake characteristics and evolutions of the unsteady wake vortices between the TRWT system and conventional SRWT systems. The power outputs of a model turbine sited in the wake flow behind the TRWT model at different downstream locations were also compared quantitatively with those of the same model turbine sited in the wake behind the SRWT model. The detailed flow field measurements were correlated with the power output data and dynamic wind loading measurements to elucidate underlying physics for higher total power yield and better durability of wind turbines.

4.2. Experimental Setup and Test Models

4.2.1. Atmospheric Boundary Layer (ABL) Wind-tunnel

The present experimental investigations were performed in a large-scale Atmospheric Boundary Layer (*ABL*) wind-tunnel located at the Aerospace Engineering Department of Iowa State University. This wind-tunnel is a closed-circuit wind-tunnel with a test section dimension of 20m×2.4m×2.3m, optically transparent side walls, and a capacity of generating a maximum wind speed of 45 m/s in the test section. Figure 1 shows a picture of the test section of the *ABL* wind-tunnel with a scaled *HAWT* model mounted in the center of floor. Chains (with a spacing of 15 inches) that are perpendicular to the flow direction were placed on the upstream floor of the wind turbine model in order to generate a typical atmospheric boundary layer wind profile and turbulence intensity usually seen in offshore wind farms. The wind-tunnel ceiling is flexible and can be adjusted along the length to ensure the turbulent boundary layer growth of the simulated *ABL* wind under close to zero pressure gradient condition in the flow direction.

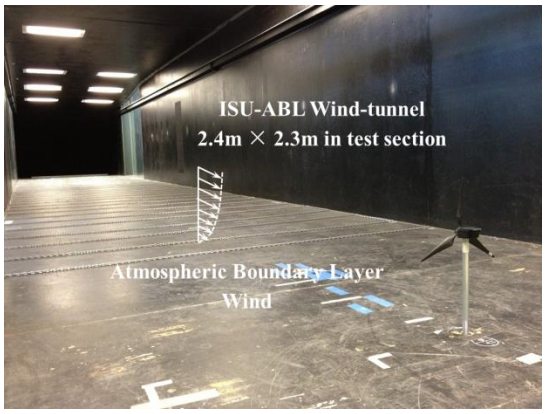

Fig. 1 Test section of the ABL wind-tunnel

It is suggested that the mean velocity profile of an atmospheric boundary layer flow over an open terrain condition can usually be fitted by using a power law (Jain, 2007). For the

present study, the wind speed at various heights can be expressed as a power law based on rotor hub height, i.e., $U(z)=U_H(z/H)^{\alpha}$, where U_H is the wind speed at hub height H. The value of the power law exponent 'α' is determined by the surface roughness. Turbines in offshore wind farms (e.g., the Greater Gabbard in UK and Horns Rev II in Denmark) operate in an *ABL* profile of $\alpha \approx 0.10$. An exponent of $\alpha \approx 0.11$ for open water (e.g., for offshore wind farms) under neutral stability conditions was recommended by Hsu et al. (1994), and this value was also recommended by ASCE standard to represent the ABL wind over offshore (open sea) terrain. Furthermore, offshore wind farms on the flat ocean surfaces have relatively lower turbulence level compared to the circumstance of onshore case. Tong (2010) and GL (Germanischer Lloyd) regulations suggested a range from 0.08 to 0.12 for the turbulence intensity at hub height of offshore wind turbines. Figure 2 illustrates the measured *ABL* wind profiles, which were obtained by using a Cobra Probe Anemometry system (TFI series 100 of Turbulent Flow Instrumentation Pty Ltd) at the location where the wind turbine model was mounted. In the present study, by adjusting the ceiling height in the test section, the wind profile fitted very well to a curve with the exponent of α=0.11 and turbulence intensity of 9.9% at the wind turbine hub height. Here turbulence intensity is defined by using the expression of $I_u = \sigma_u / \overline{U}_{local}$, where σ_u is the root-mean-square of the turbulent velocity fluctuation, and $\overline{U}_{local}$ is the time-averaged local velocity where Cobra probe located.

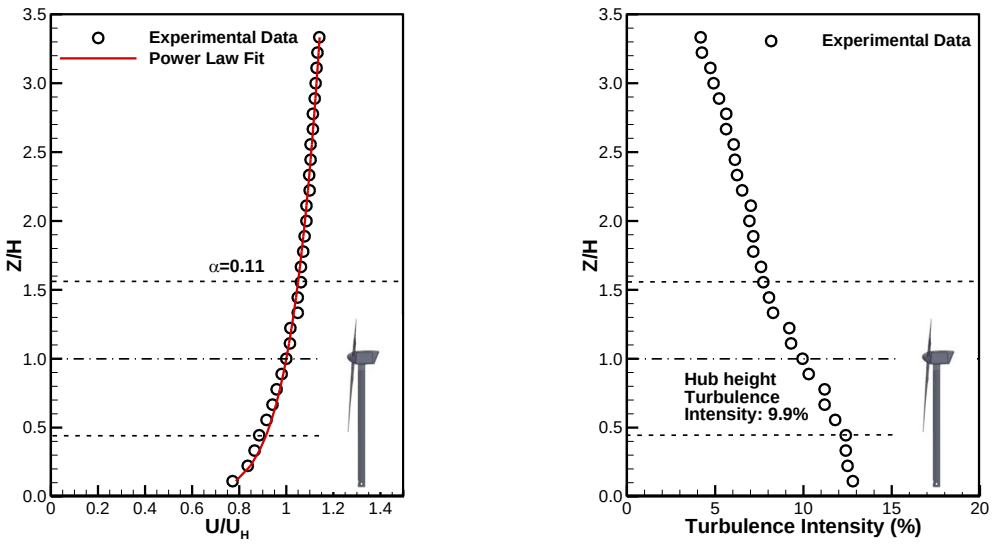

(a) Mean velocity profile (b) Turbulence intensity profile

Fig.2 Measured Atmospheric Boundary Layer wind profiles

4.2.2. Wind turbine models

In the present investigation, two wind turbine models were built for the comparative experiments. A *SRWT* was used as the baseline, which represents the most widely used three-blade *HAWT*. The detailed description about the design parameters for the *SRWT* can be found in the previous study (Tian et al., 2013). Figure 3 illustrates the dimensions of the *TRWT*. In order to give a considerable comparison with the *SRWT*, an auxiliary rotor with three small blades was appended on the main rotor (the same shaft used in the *SRWT*). The phase-offset for auxiliary and main rotors was designed with 60 degrees. The diameters for the main rotor and auxiliary rotor are 280*mm* and 150*mm* respectively, the height of the turbine nacelle is 225*mm* over the wind-tunnel floor. These test models (at a scale ratio of 1:350) simulate the typical commercial horizontal axis wind turbines mounted in the offshore wind farm with the rotor diameter around 90*m* and tower height about 80*m*. The rotor blades consist of hard plastic materials which were built by using a fast prototyping machine. It

should be noted that the blockage ratio of the wind turbine models (i.e., the ratio of the turbine blades sweeping area to the cross-section area of the *ABL* wind-tunnel test section) was found to be 1.2%, and thus the blockage effect of the wind turbine models in the test section can be negligible for present study.

During the experiments, the wind turbine models were installed in the simulated *ABL* wind. The mean wind velocity at hub height was set to be around 6.5 m/s (i.e., U_H=6.5m/s), which corresponded to the rotor diameter Reynolds number to be about 1.2×10^5 (i.e., $\mathrm{Re}_D \approx 1.2\times10^5$, based on the rotor diameter and the wind speed at the hub height). It is significantly lower than those of the utility-scale wind turbines ($\mathrm{Re}_D > 1.0\times10^7$) in wind farms. As a result, it may have an essential effect on the power generation performance of the wind turbine (i.e., the maximum power coefficient would be much lower for a small-scale model turbine operating at a lower Reynolds number). However, according to a comprehensive investigation conducted by Chamorro et al. (2011) recently, they found that the fundamental flow statistics (e.g., normalized profiles of mean velocity, turbulence intensity, and kinetic shear stress) showed asymptotic behavior with Reynolds number in the wake. Mean velocity in the wake to reach Reynolds number independence at a lower values compared to those of higher statistics (i.e., turbulence intensity and kinetic shear stress). Reynolds number independence for mean velocity could be reached at $\mathrm{Re}_D \approx 4.8\times10^4$ and that of higher order statistics started at $\mathrm{Re}_D \approx 9.3\times10^4$. It should be noted that the Reynolds number for the present study is around 1.2×10^5, which is in the range of the required minimum Reynolds number as suggested by Chamorro et al. (2011) to satisfy Reynolds dependence for wake flow characteristics. In addition, Whale et al. (2000) observed similar wake statistics for a wide range or Reynolds number although the boundary layer over the

blades and the shedding vorticity is known to be highly sensitive to Reynolds number. As suggested by Medici et al. (2006), the behaviors of the unsteady vortex and turbulent flow structures in the wake of wind turbines would be almost independent to the Reynolds number when the Reynolds number of the wind turbine is high enough. The wind turbines with similar tip-speed-ratio (*TSR*) would generate similar near wake characteristics such as helical shape, rotation direction and strength decay of the tip vortices. In the present experiments, the incoming wind velocity was kept as constant; the rotating speed of the rotors was varied by applying different electric loadings to the small electricity DC generator installed inside the turbine nacelle.

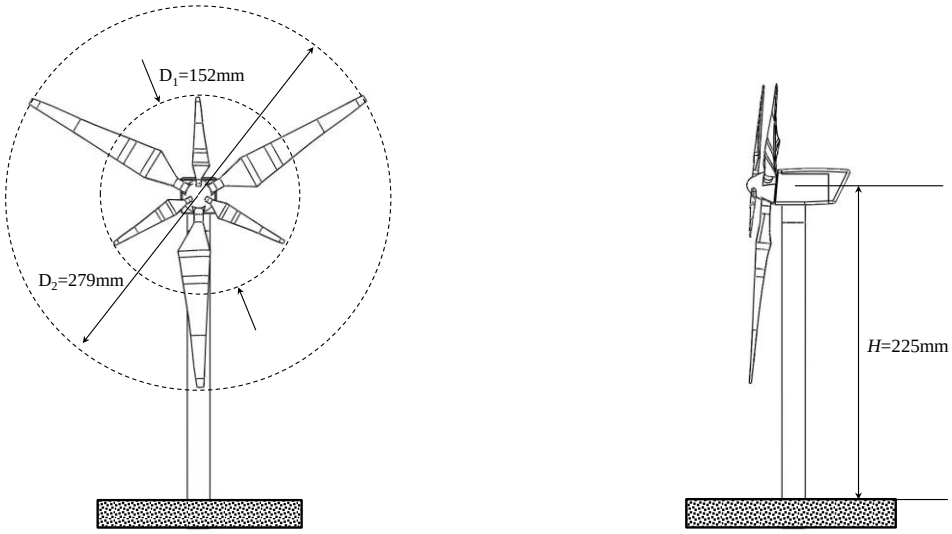

(a) Front view (b) Side view

Fig.3 Schematic of the TRWT model used in the present study

4.2.3. Measurements of power outputs and dynamic wind loads acting on the turbines

During the experiments, the rotation speed of the turbine rotors was adjusted by applying different electric loads to the small direct current (DC) electricity generators installed inside the turbine nacelles. The turbine rotation speed Ω can change from 0 to 2200 rpm, and the

tip-speed-ratio ($\lambda = \Omega R/U_{hub}$, where R is the radius of the main rotor) of the turbine models is in the range from 0 to 6.5. The power outputs of the model turbines were achieved by measuring the voltage outputs of the small generators installed in the turbine nacelles and the corresponding electrical loadings applied to the electric circuits. During the experiments, the voltage outputs of each DC generator were acquired through an A/D board plugged into a host computer at a data sampling rate of 1.0 kHz for 120 seconds. By applying different electric loads to the small electricity generators, the optimum tip-speed-ratio of a turbine model, i.e., at the tip-speed-ratio when the turbine model reaches the maximum power output, can be determined. The optimum tip-speed-ratio (TSR) of the wind turbine models used in the present study was found to be about 5.0 (i.e., $TSR \approx 5.0$).

It should be noted that, since the Reynolds number of the small model wind turbine models used in the present study is much smaller than those of utility-scale wind turbines sited in wind farms, the absolute values of the power coefficients of the small wind turbine models used in the present study (i.e., $C_P \approx 5\%\sim12\%$) were found to be much smaller than those of the utility-scale wind turbines. Instead of using absolute values of the power coefficients, the normalized power outputs of the model turbine (i.e., normalized by the power output of the same turbine model operating in isolation) were used in the present study to assess the effectiveness of using the TRWT design to reduce the wake losses for improved wind farm efficiency.

For the current study, the wind turbine rotor and nacelle were supported by an aluminum rod which was also used as a turbine tower. A high-sensitive force-moment sensor (JR3 load cell, model 30E12A-I40) was mounted under the wind tunnel floor and was used for holding the turbine tower, and measuring the dynamic wind loads (thrust forces and bending

moments) acting on the wind turbine models. The JR3 load cell is capable of measuring the forces on three orthogonal axes and the moments about each axis. The precision of this load cell for force measurements is ±0.25% of full range (40N). During the experiments, the dynamic wind load data were acquired for 120 seconds at a sampling rate of 1,000 Hz for each testing case.

4.2.4. PIV measurements and point-wise velocity measurements to quantify the wake characteristics behind the model turbines

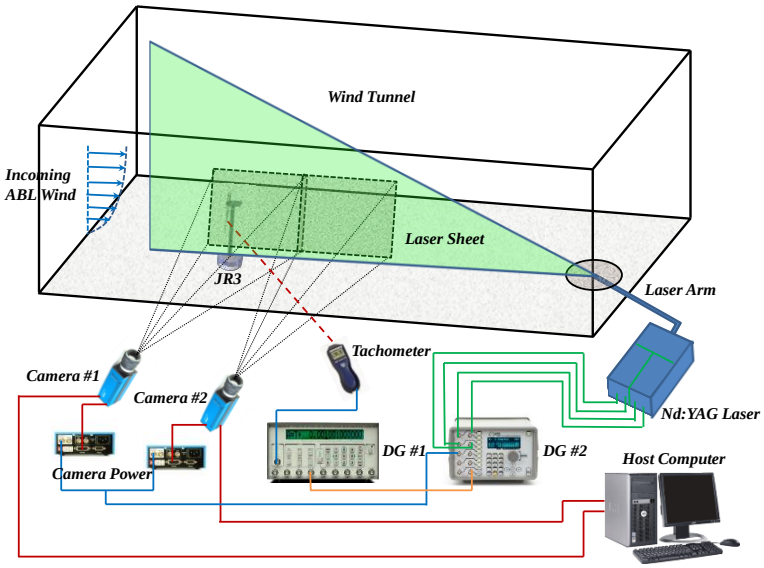

Fig.4

Fig.4 Experimental setup used for 2-D PIV measurements

Figure 4 illustrates the schematic of the experimental setup applied for 2-D PIV measurements, which was used to obtain detailed flow field measurement to quantify the turbulent flow structures in the near wake (X/D<2.5) of the test models. The airflow was seeded with ~1um oil droplets by using a fog generator (ROSCO 1900). Illumination was provided by a double-pulsed Nd:YAG laser (EverGreen 200) with a pulse energy of 200 mJ at the wavelength of 532nm. The laser beam was shaped to a sheet by a set of mirrors along

with spherical and cylindrical lenses. The thickness of the laser sheet in the measurement region was about 1.5mm. A high resolution 14 bit CCD camera (PCO2000) was used for image acquisition with the axis of camera oriented perpendicular to the laser sheet. In the present study, because the image capture window size from one camera was not enough to cover the near wake region, two cameras with an overlapping region of 20mm length were used to capture the images to cover the whole interested flow field (~2.5*D*) simultaneously. The CCD camera and the double-pulsed Nd:YAG laser were connected to a host computer via digital delay generator (BNC565), which was used to control the timing of the laser illumination and image acquisition.

After image acquisition, the instantaneous *PIV* velocity vectors were calculated from the cross-correlation of 32 × 32 pixels interrogation windows. An effective overlap of 50% of the interrogation windows was employed in the PIV image processing. The vorticity ($\omega_z = \frac{\partial v}{\partial x} - \frac{\partial u}{\partial y}$) can be calculated from the instantaneous velocity vectors (u_i,v_i). The distributions of the ensemble-averaged flow statistics such as the mean velocity, normalized Reynolds stress ($\tau = -\overline{u'v'}/U_H^2$), and turbulence kinetic energy ($TKE = 0.5(\overline{u'^2} + \overline{v'^2})/U_H^2$) were also calculated from the data after image processing. In the present study, a sequence of 1000 frames of instantaneous PIV image pairs were acquired in order to achieve a good convergence of flow quantities of the PIV measurements, especially for high-order turbulence statistics such as TKE and Reynolds stress. The measurement uncertainty level for the first-order flow quantity such as velocity vector is estimated to be within 2%, while the uncertainties levels for ensemble-averaged high-order flow statistics such as TKE and Reynolds stress distributions are about 5%.

Both “free-run” and “phase-locked” PIV measurements were performed during the experiments. The “free-run” PIV measurements were conducted in order to determine the time-averaged flow quantities (e.g., mean velocity, TKE, Reynolds stress) in the near wake flow. For the “free-run” experiments, the image acquisition rate was selected at a fixed frequency which would avoid matching the harmonic frequency of the rotating blades in order to obtain as much blade phase positions as possible to ensure the ensemble-averaged flow statistics. The “phase-locked” PIV measurements were performed to elucidate more details about the evolution of unsteady wake structures such as vortices related to the phase position of the rotating blades. For the “phase-locked” measurements, a digital tachometer (Monarch PLT 200) and an additional timing delay generator (Stanford DG535) were used to detect the phase position of a pre-marked rotor blade to achieve the “phase-locked” PIV measurements. By adding variant time delays between the input signal from the tachometer and the output TTL signal from the delay generator to trigger the PIV system, the “phase-locked” measurements at different rotor blade phase angles can be achieved. At each selected phase angle, 400 frames of image pairs were acquired to calculate the phase-averaged flow quantities (i.e., velocity and vorticity) distribution in the wake flow.

A Cobra probe Anemometry (TFI Series 100 of Turbulent Flow Instrumentation Pty Ltd) system was mounted on an accurate motorized traverse system, which was used to measure all three components of instantaneous and time-averaged flow velocity and at the locations of interest to supplement the PIV results, especially at far wake region (i.e., at the downstream locations of X/D=2, 4, 6 and 8). The Cobra Probe anemometry is capable of measuring all three components of instantaneous flow velocity at a prescribed point with a sampling rate up to 2.5 KHz. In the present study, the Cobra probe was used to acquire the velocity data at a

sampling rate of 2.5 KHz for 60 seconds at each measurement location. Other flow quantities such as the turbulence intensity can also be derived based on the instantaneous measured data.

4.3. Measurement Results and Discussions

4.3.1. Dynamic wind loads acting on the wind turbine models

In the present study, the wind loading measurements were conducted with the TRWT and SRWT models mounted in the same incoming boundary layer airflow and operating at their optimum tip-speed-ratio (i.e., $TSR \approx 5.0$) where the power outputs of model turbines reaching their peak values. The JR3 load cell used in the present study can provide time-history measurements of all three force components and moments about each axis at a certain sampling rate. According to a similar research conducted by Hu et al. (2012), tip-speed-ratio (TSR) was adjusted by applying different electric loads to the small electricity generator installed inside the turbine nacelle. The thrust coefficient and the bending moment coefficient which as a function of TSR of the wind turbine model, are defined as

$$C_T = T / (0.5\rho U_H^2 \pi R^2) \tag{1}$$

and

$$C_M = M / (0.5\rho U_H^2 \pi R^2 H) \tag{2}$$

where T is the thrust force acting on the wind turbine model, M is the bending moment,, ρ is the air density, U_H is the air incoming velocity at hub height, R is the radius of the turbine rotor. As shown clearly in Fig. 5, the instantaneous wind loads acting on the model turbines were found to be highly unsteady with their magnitudes fluctuating significantly as a function of time. While the TRWT and SRWT models were mounted in the same incoming turbulent boundary layer airflow, due to the existence of the additional set of the auxiliary

rotor blades, the dynamic wind loads acting on the TRWT model were found to become much greater (i.e., both the mean values and the fluctuation amplitudes) than those acting on the SRWT model.

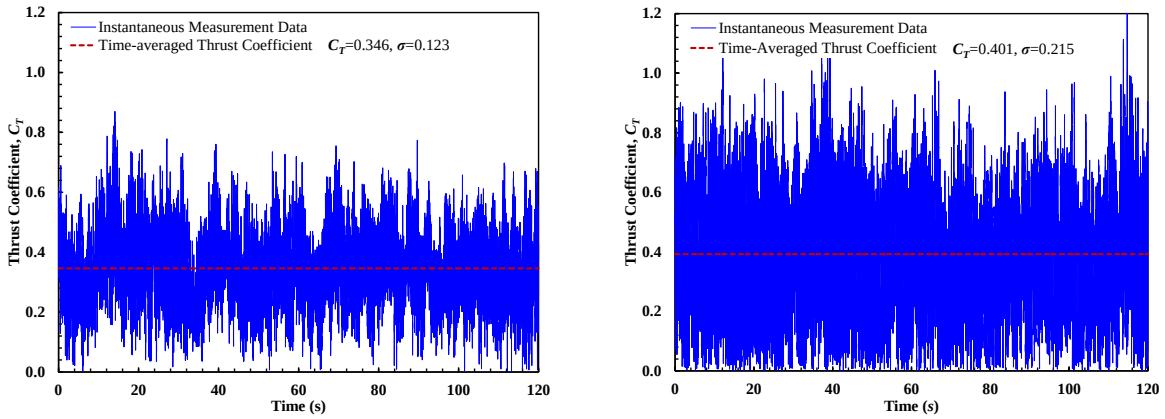

Fig.5 Time history of the instantaneous thrust coefficient for SRWT (left) and TRWT (right)

Table.1 The wind loads acting on the turbines in SRWT and TRWT models

	SRWT	TRWT
Mean thrust coefficient, C_T	0.346	0.401
The standard deviation of the thrust coefficient, σ_{CT}	0.123	0.215
Mean bending moment coefficient, C_M	0.411	0.475
The standard deviation of the bending moment coefficient, σ_{CM}	0.133	0.324

Based on the time sequences of the dynamic wind loading measurements as those shown in Fig. 5, the mean and standard deviation values of the dynamic wind loads acting on the model turbines can be determined, and the results are listed in Table 1, which reveal the characteristics of the dynamics wind loads acting on the TRWT and SRWT models more clearly and quantitatively. It can be seen that, due to the existence of the auxiliary rotor blades appended in front of the main rotor blades for the TRWT model, the mean wind loads

acting on the TRWT model increased slightly (i.e., ~ 16% increase in both the time-averaged thrust force and mean bending moment), the standard deviation values of the dynamic wind loads acting on the TRWT model were found to increase much more significantly (i.e., ~75% increase in the dynamic thrust force, and 140% more in the dynamic bending moment), in comparison with those acting on the SRWT model.

As described in the article of Hu et al. (2012), according to the momentum and energy conservation laws, while the aerodynamic thrust force acting on a wind turbine is proportional to the momentum deficits in the square of the flow velocity (i.e., momentum differences) across the rotation disk of the wind turbine, the power output of the wind turbine (i.e., the wind energy harvested by the wind turbine) would be proportional to the deficits in the cube of the flow velocity (i.e., the differences in flow kinetic energy) across the rotation disk. With the turbine models mounted in the same incoming airflow, the higher mean thrust force acting on the TRWT model (i.e., $\boldsymbol{C_T}$=0.401 for the TRWT model versus $\boldsymbol{C_T}$=0.346 for the SRWT model) is believed to be closely related to the better wind energy harness performance of the TRWT design by reducing the root losses of the wind turbine (i.e., the auxiliary rotor blades would harvest extra wind energy from in the regions near the roots of the main rotor blades). A similar relationship between the measured thrust coefficients and the power coefficients of wind turbines was also reported by Adaramola & Krogstad (2011) in their study to investigate the effects of various pitch and yaw angles of rotor blades on the power generation and thrust coefficients of wind turbines.

It should also be noted that, as described in Tian et al. (2014), the standard deviation of the dynamic wind loads acting on a wind turbine can be used as a quantitative parameter to evaluate the fatigue loads acting on the wind turbine. In comparison with those of the SRWT

case, the much larger fluctuation amplitudes of the dynamic wind loads acting on the TRWT model would indicate much severe fatigue loads acting on the TRWT models. This is believed to be closely related to the much more complicated wake vortex structures and higher turbulence kinetic energy (TKE) and Reynolds stress levels in the wake flow behind the TRWT model induced by the additional auxiliary rotor blades, which were revealed clearly and quantitatively in the PIV measurements to be discussed in the next session.

4.3.2. 2-D PIV measurement results

As described above, a high-resolution PIV system was used in the present study to quantify the characteristics of the wake flows behind the TRWT and SRWT models. Based on a cinema sequence of about 1,000 frames of instantaneous PIV measurements, the ensemble-averaged flow quantities in the turbine wake flows, such as the mean velocity, normalized Reynolds Stress and in-plane *TKE* values, were determined. Figure 6 shows the ensemble-averaged flow velocity distributions in the wake flows behind the SRWT and TRWT models. As shown clearly in Fig. 6, since a portion of the kinetic energy carried by the incoming airflow was harvested by the model turbines, the incoming airflow was found to decelerate greatly as it passed through the rotation disks of the turbine blades. As a result, the magnitudes of the flow velocity in the wakes behind the turbine models were found to become much smaller, in comparison with those in the incoming airflow. The PIV results given in Fig. 6(a) also reveal clearly the existence of a region with relatively high velocity in the near wake behind the SRWT model right above the turbine nacelle and near the roots of the turbine rotors (i.e., $Z/D<0.2$), which extends up to $X/D=0.5$ downstream. This is believed to be due to the aerodynamically poor design at the roots of the rotor blades (i.e., the rotors of the rotor blades are designed mainly to provide structural integrity, instead of harvesting

wind energy) for the SRWT case, which results in a "dead zone" near the roots of turbine rotor blades where virtually very little wind energy is harnessed by the wind turbine. For the TRWT case, since the smaller auxiliary rotor blades appended in front of the main rotor blades would be able to harness extra wind energy from the same incoming airflow by eliminating the "dead zone" near the roots of main rotor blades (i.e., reducing the root losses), the flow velocity behind the TRWT model were found to become much smaller in the near wake region, especially in the region near the roots of the main rotor blades.

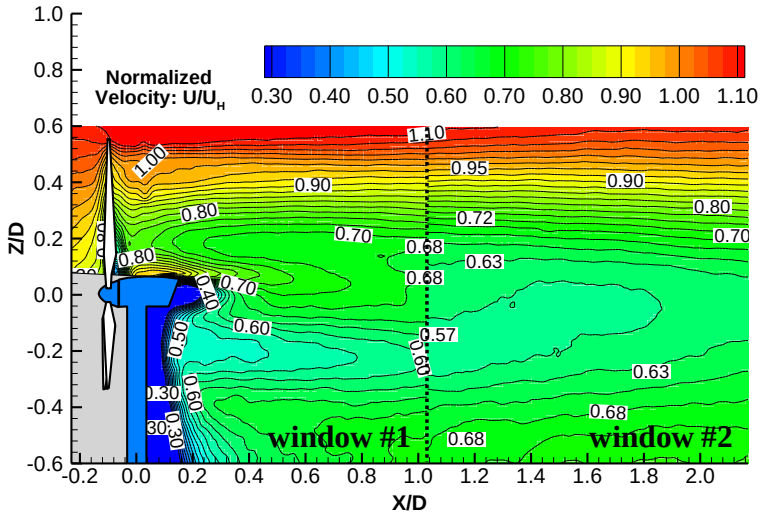

(a) The wake behind the SRWT model

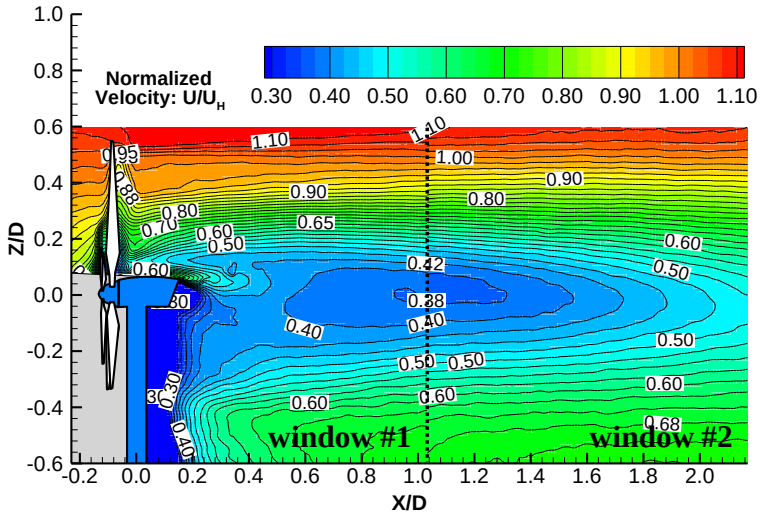

(b) The wake behind the TRWT model

Fig. 6 Ensemble-averaged velocity distributions for the SRWT and TRWT models

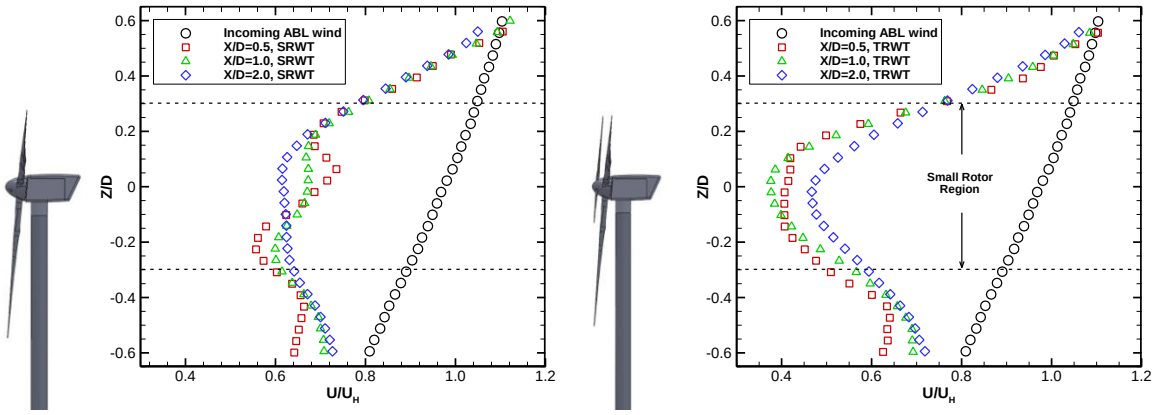

(a) In the wake of the SRWT model (b) In the wake of the TRWT model

Fig.7 Transverse velocity profiles in the wake flows behind for SRWT and TRWT

Figure 7 illustrates the transverse velocity profiles extracted from the ensemble-averaged PIV measurement results at the downstream locations of *X/D*=0.5, 1.0 and 2.0, respectively. The mean velocity profile of the incoming airflow was also plotted in the plots for comparison. It can be seen clearly that, compared with the velocity profile of the incoming airflow, significant velocity deficits were found to be generated in the turbine wakes due to the installation of the wind turbine models. The size of the regions with significant velocity deficits were found to be much greater than those can be expected from the turbine nacelle only. In comparison with those behind the SRWT model, the velocity deficits behind the TRWT model were found to be much more significant, especially in the downstream of the sweeping area of the smaller auxiliary rotor blades near the roots of the main rotor blades. As described in Hu et al. (2012), larger velocity deficits in the near wake behind a wind turbine would indicate a stronger thrust force acting on the wind turbine as well as a better power production performance of the wind turbine design. With the TRWT and SRWT models mounted in the same incoming airflow, larger velocity deficits in the near

wake behind the TRWT model would indicate a greater thrust force acting on the TRWT model as well as a better power production performance of the TRWT design in comparison with those of the conventional SRTW design. While the stronger wind loads acting on the TRWT model were confirmed quantitatively from the wind loads measurement results given in Table 1, the better power production of the TRWT design is due to the existence of the smaller auxiliary rotor blades appended in front of the main rotor blades to reduce the root losses of the main rotor blades.

Based on the measurement results given in Fig. 7(a), it can also be seen that, very little changes can be observed among the transverse velocity profiles extracted at different downstream locations behind the SRWT model up to X/D=2.0. It indicates that the velocity deficits in the wake behind the SRWT model would need a much longer distance to recover. However, as shown in Fig. 7(b), while the velocity deficits behind the TRWT model were also found to recover very slowly in the near wake region (i.e., X/D≤1.0 region), the recovery of the velocity deficits in the wake behind the TRWT model was found to become much faster in the far wake region (i.e., X/D>1.0 region). The much faster recovery of the velocity deficits in the far wake behind the TRWT model is believed to be closely related to the generation of more complex wake vortex structures and enhanced turbulent mixing of the turbine wake flow due to the existence of the auxiliary rotor blades appended in front of the main rotor blades, which were revealed clearly from the measured TKE and turbulent Reynolds stress distributions in the wake flow behind the TRWT model given in Fig. 8 and Fig. 9.

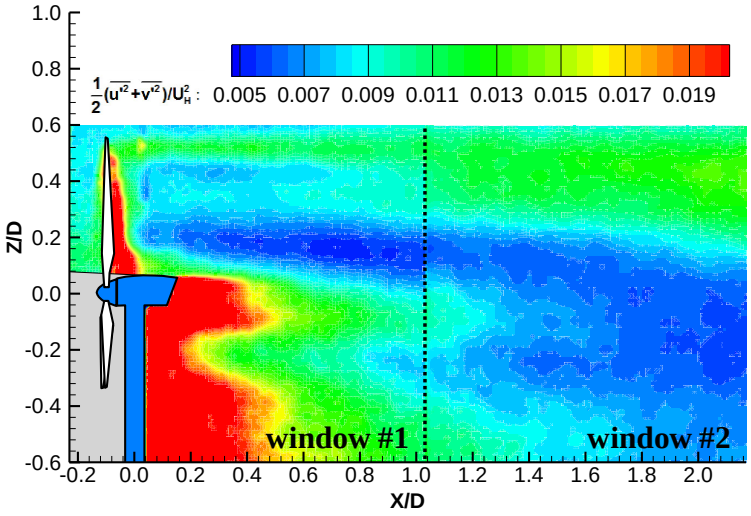

(a) Normalized TKE distributions behind the SRWT model

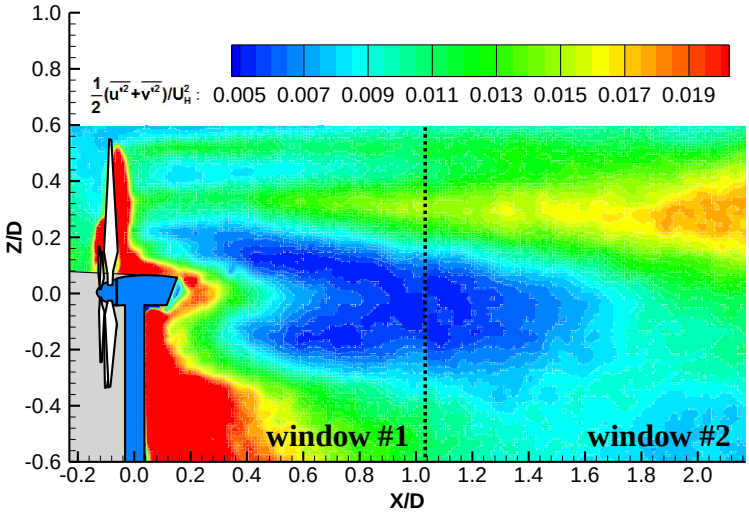

(b) Normalized TKE distributions behind the SRWT model

Fig.8 Normalized TKE distributions in the wake flows behind the SRWT and TRWT models

Figure 8 shows the normalized in-plane turbulent kinetic energy, i.e., $TKE = 0.5(\overline{u'^2} + \overline{v'^2})/U_{hub}^2$, distributions in the turbine wake flows, which can provide further insights to explain the differences in the wake velocity deficit recovery behind the two compared turbine models. Lignarolo et al. (2014) and Tian et al. (2014) suggested that the evolution of the unsteady wake vortices (i.e., the generation, breakdown and dissipation

processes) would play an important role on the TKE production in a turbine wake. As shown clearly in Fig. 8, the regions with relatively high TKE levels were found to concentrate in the wakes immediately behind the turbine nacelles and towers. This is believed to be closely related to the formation and shedding of unsteady wake vortices from the turbine nacelles and towers, which are visualized more clearly from the "phase-locked" PIV measurement results to be discussed later. The TKE levels were also found to be quite high at the upper regions behind the rotation disks of the turbine blades, which is correlated well to the shedding paths of the unsteady tip vortices from the tips of the rotating rotor blades in the PIV measurement plane. The expansion of the turbine wakes with the increasing downstream distance can also be observed from the TKE distributions.

While the distribution pattern of the measured TKE values in the turbine wakes behind the two model turbines was found to be quite similar in general, some obvious differences still can be identified from the comparison of the TKE distributions behind the TRWT and SRWT models. Corresponding to the tip vortex shedding from the smaller auxiliary rotor blades appended in front of the main rotor blades, an additional region with relatively high TKE levels was also found to exist in the wake behind the TRWT model (i.e., X/D<1.0), in comparison with those behind the SRWT model. The onsets of the tip vortex breakdown (i.e., the starting points of the regions with much higher *TKE* levels) in the wake flows behind the TRWT and SRWT models were also found to be quite different. The breakdown of the tip vortices in the wake behind the TRWT model was found to take place earlier than that behind the SRWT model. The absolute TKE values in the wake behind the TRWT model were also found to be greater than those of behind the SRWT model, especially in the wake region (i.e., X/D>1.0 region). As described in Tian et al. (2014), the TKE level can usually be used as a

parameter to indicate the extent of turbulent mixing in a turbulent flow. In comparison with those of the SRWT case, the higher TKE levels in the TRWT wake would indicate more intensive mixing in the wake flow, resulting in a faster recovery of the velocity deficits in the wake behind the TRWT model. It should also be noted that, the absolute TKE values along the shedding paths of the tip vortices in near wake region (i.e., $X/D < 1.0$) were found to be relatively low in general, where concentrated tip vortices were observed in the "phase-locked" PIV measurement results to be discussed later. The measurement results were found to agree well with the findings reported in Medici (2005), who suggested that the concentrated tip vortices would act as a shield preventing turbulent mixing and TKE production in the near wake of a wind turbine.

Based on a series of experimental and numerical studies on the wake interferences of wind turbines, Meneveau (2010; 2010; 2010; 2001) and his co-workers suggested that the vertical fluxes of kinetic energy into arrays of wind turbines are very essential to determine how much power can be extracted from the incoming surface wind by turbines on a wind farm. They also proposed that the energy extracted from a turbine array is less a matter of wind passing through one turbine to the next and more of turbulence created behind one turbine drawing down high velocity wind from above. As described in Wu et al., (2012), Calaf et al. (2010) and Cal et al. (2010), the Reynolds stress levels in a turbine wake would play a very important role in promoting the vertical transport of the kinetic energy from above into a turbine wake. Higher Reynolds stress levels in a turbine wake will draw down more high velocity airflow from above to "re-charge" the low momentum wake flow behind the wind turbine. Figure 9 shows the normalized Reynolds stress distributions in the wakes behind the SRWT and TRWT models. As shown in Fig. 9, the regions with relatively higher

levels of Reynolds shear stress were found to exist in the turbine wakes at the top tips of turbine main rotors, similar to the *TKE* distributions given in Fig. 8. As the distance away from the turbine model increases, the absolute values of the Reynolds shear stress in the turbine wakes were found to increases rapidly at the top-tip levels of the main rotor blades. Higher levels of the Reynolds shear stress were also observed in the wakes behind the turbine towers and nacelles. It should also be noted that, while the general features of the Reynolds stress distributions in the turbine wakes for the two compared turbine models were found to be quite similar, the absolute values of the Reynolds shear stress in the turbine wake behind the TRWT model were found to be greater than those of the SRWT case, especially in the far wake region behind the TRWT model (i.e., in the downstream region of X/D>1.0).

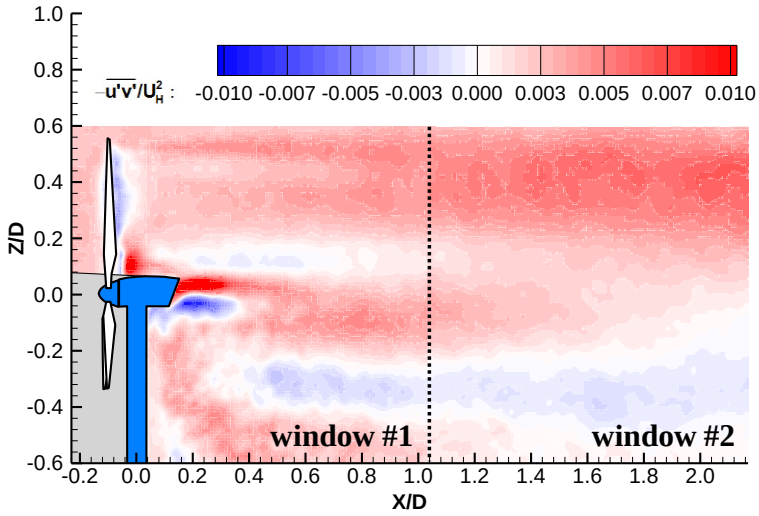

(a) Normalized Reynolds shear stress distributions behind the SRWT model

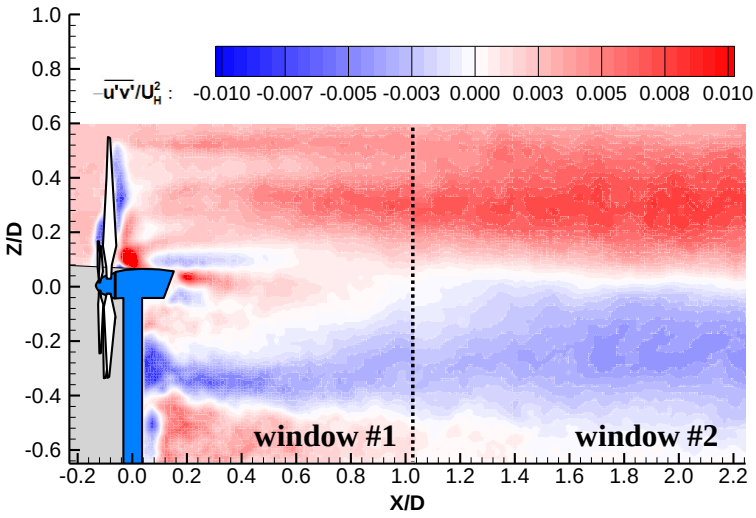

(b) Normalized Reynolds shear stress distributions behind the TRWT model

Fig.9 Normalized Reynolds stress distributions for SRWT (left) and TRWT (Right)

Based on the comparisons of the *TKE* and Reynolds stress distributions described above, it can be seen that, due to the existence of the smaller auxiliary rotor blades appended in front of the main rotor blades, the *TKE* and Reynolds shear stress levels in the wake behind the TRWT models were found to become higher in comparison with those of the SRWT case, especially in the far wake region (i.e., X/D>1.0). As suggested by Wu et al. (2011), Calaf et al. (2010) and Cal et al. (2010), the higher *TKE* and Reynolds shear stress levels in the wake flow would indicate more intensive mixing in the turbine wake, which would cause a faster vertical transport of kinetic energy by entraining more high-speed airflow from above to re-charge the lower momentum wake flow behind the TRWT model. As a result, the velocity deficits in the wake behind the TRWT model would recover much faster than those behind the SRWT model, especially in the far wake region (i.e., in the downstream region of X/D>1.0).

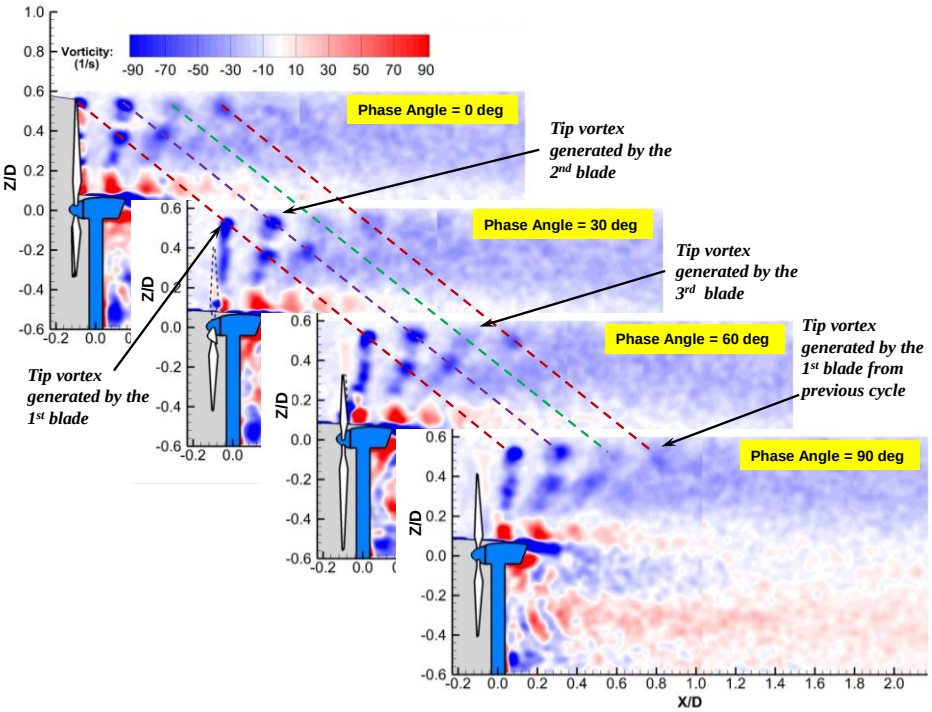

(a) Vorticity distributions in the wake behind the SRWT model

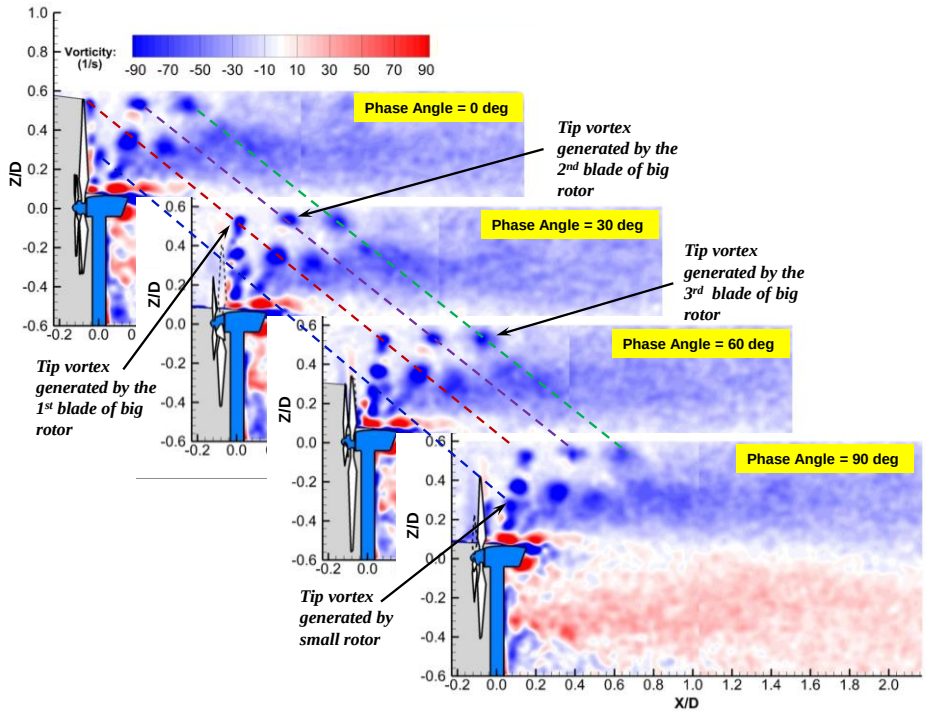

(b) Vorticity distributions in the wake behind the TRWT model

Fig.10 Phase-locked vorticity distributions in the wake flows

"Phase-locked" PIV measurements were also conducted in the present study to produce "frozen" images of unsteady vortex structures in the turbine wakes at different rotation phase angles of the turbine rotor blades, from which the dependence of the unsteady wake vortices on the rotation of the rotor blades can be revealed more clearly. In the present study, the phase angle is defined as the angle between the vertical PIV measurement plane and the position of a pre-marked main rotor blade. The pre-marked rotor blade would be in the most upward position (i.e., within the vertical PIV measurement plane) at the phase angle of θ = 0.0°. As the phase angle increases, the turbine blade would rotate out of the vertical PIV measurement plane. Figures 10 gives the "phase-locked" PIV measurement results in the term of the vorticity distributions in the wakes behind the SRWT and TRWT models at the phase angle of θ = 0.0°, 30.0°, 60.0°, and 90.0°, respectively. It can be seen clearly that, the wake flows behind the wind turbine models are actually very complex turbulent flows, which are almost fully filled with various unsteady vortex structures in different sizes and orientations.

As shown clearly in Fig. 10(a), a tip vortex was found to be induced in the wake flow behind the SRWT model from the tip of the pre-marked rotor blade at the phase angle of θ =0.0°. With the pre-marked turbine blade rotating out of the vertical PIV measurement plane (i.e., the phase angle increasing), the tip vortex was found to shed from the tip of the pre-marked rotor blade. As moving downstream, the tip vortex was found to align itself nicely with other tip vortices induced by other rotor blades to form a moving tip vortex array in the wake behind the SRWT model. An additional row of concentrated vortex structures were also found to be generated in the wake flow at approximately 60% ~ 70% span of the turbine blades. The vortex structures were found to move outward with the expansion of the wake

flow behind the SRWT model, merging with the tip vortex structures and dissipated eventually at further downstream locations. Similar wake vortex structures at approximately 60%~70% span of the rotor blades were also observed in the experimental studies of Hu et al. (2012), Tian et al. (2014) and (Whale et al. (2000) to investigate the evolution of the unsteady vortex structures in turbine wake flows. It can also be seen that unsteady vortices would also be generated and shed periodically from the roots of the turbine rotor blades (i.e., root vortices), as expected. Other wake vortex structures, such as those generated over the upper and lower surfaces of the turbine nacelles as well as the unsteady von-Karman vortex streets shedding from the turbine towers, can also be observed clearly in the phase-locked PIV measurements. As described in Tian et al. (2014), the flow characteristics in the turbine wake were found to be dominated by the evolution (i.e., formation, shedding, breakdown and dissipation) of the unsteady wake vortices.

Due to the existence of the auxiliary rotor blades appended in front of the main rotor blades, the wake vortex structures behind the TRWT model were found to become more complicated, in comparison to those behind the conventional SRWT model. As shown in Fig. 10(b), in addition to the similar wake vortex structures as those behind the SRWT model (i.e., the tip and root vortices shedding from tips and roots of the main rotor blades, the concentrated vortices at 60%~70% blade span of the main rotor, and the unsteady vortices shedding from the turbine nacelle and tower), a new set of tip vortices were also found to be generated and shed periodically from the tips of the smaller auxiliary rotor blades of the TRWT model. Induced by the tip vortices shedding from the tips of auxiliary rotor blades, the concentrated vortices at 60%~70% span of the main rotor blades were found to move inward as they travel downstream in the wake behind the TRWT model, whereas the vortex

structures were found to move outward for the SRWT case. The root vortices shedding from the roots of the main rotor blades were also found to become much smaller and weaker due to the effects of the auxiliary rotor blades appended in front of the main rotor blades. Due to the more complicated interactions among the wake vortices behind the TWRT model, the breakdown of the concentrated tip vortices and the wake vortices at 60%~70% span of the main rotor blades were found to take place earlier in the wake behind the TRWT model, in comparison with that behind the SRWT model (i.e., vortex breakdown at $X/D\approx0.6$ for the TRWT case, while at $X/D\approx0.9$ for the SRWT case), which was found to be in good agreement with the earlier appearance of the regions with relatively high TKE and Reynolds stress in the wake behind the TRWT model as shown in Figs. 8 and 9.

4.3.3. Flow characteristics in the far wakes behind the SRWT and TRWT models

As described above, a Cobra Probe Anemometry system was also used in the present study to conduct flow velocity measurements in the far wakes behind the wind turbine models (i.e., in the region of X/D≥2.0) to supplement the near wake PIV measurements. Figures 12 and 13 give the measured transverse profiles of the streamwise velocity and turbulent intensity in the far wakes behind the SRWT and TRWT models at the downstream locations of X/D=2.0, 4.0, 6.0 and 8.0, respectively. The streamwise velocity and turbulent intensity profiles of the incoming airflow were also given in the plots for comparison. Based on the measured streamwise velocity and turbulent intensity profiles as those shown in Figs. 11 and 12, the upper boundaries of the turbine wakes can be identified easily, and indicated as the dash lines in the plots. As expected, the turbine wakes were found to expand monotonically as the downstream distance increases.

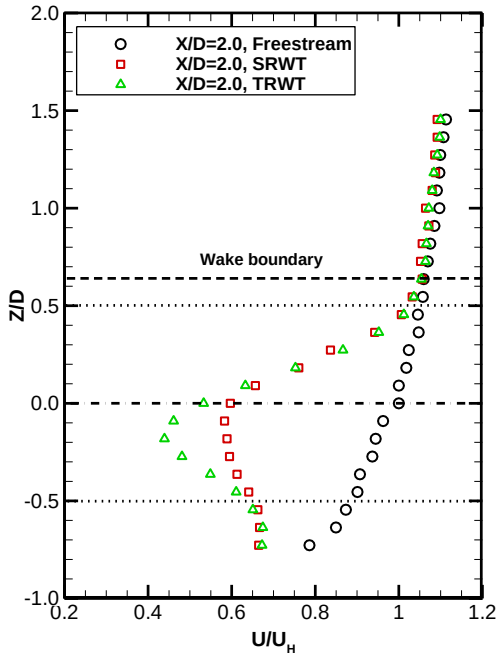

(a) X/D=2.0

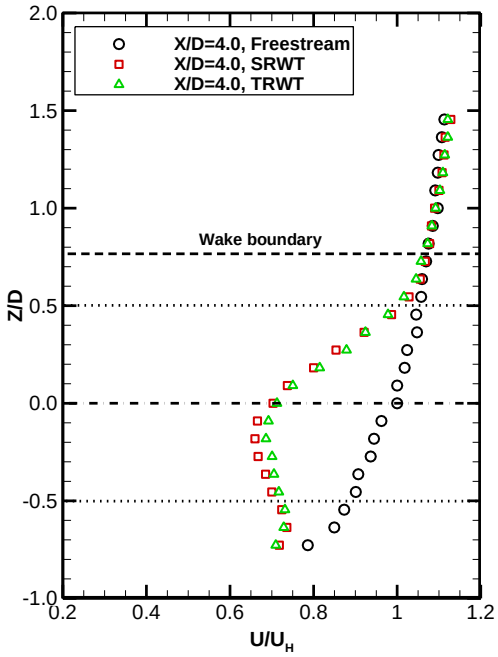

(b) X/D=4.0

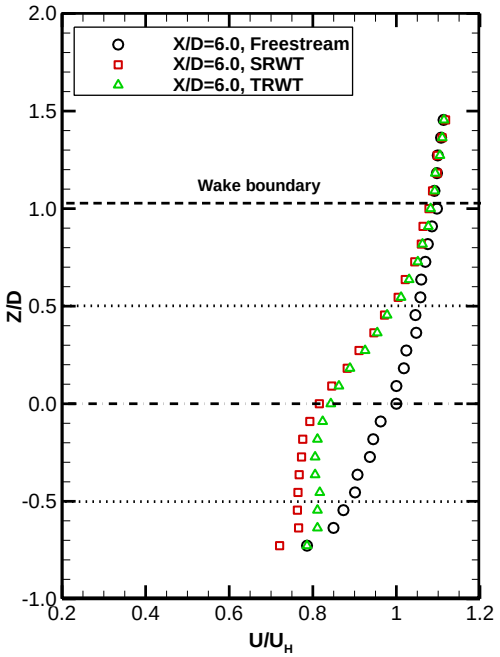

(c) X/D=6.0

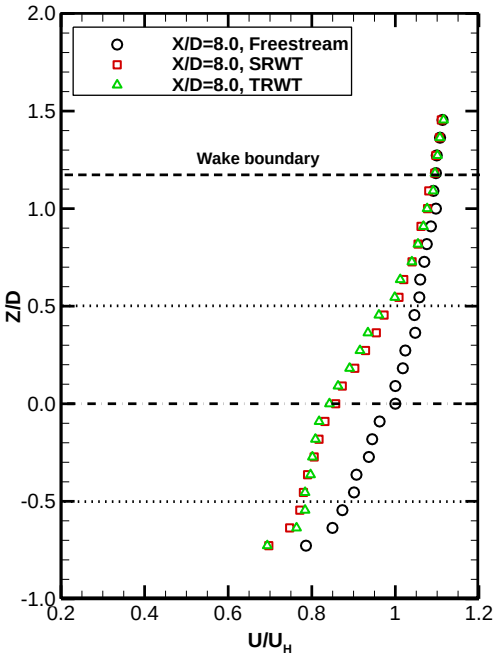

(d) X/D=8.0

Fig.11 Transverse velocity profiles in the far wakes behind the SRWT and TRWT models

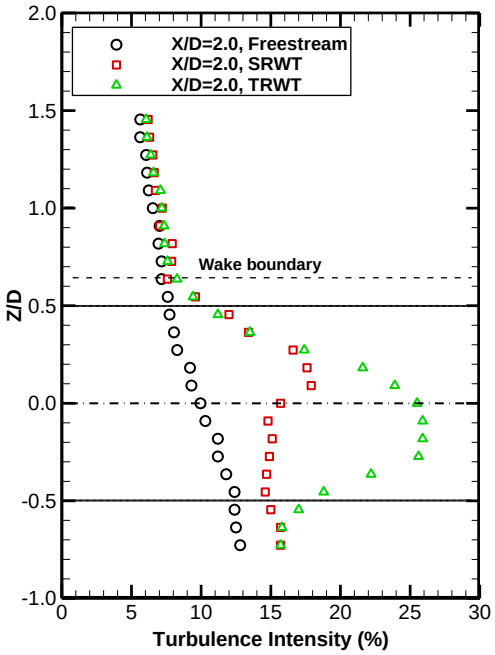

(a) X/D=2.0

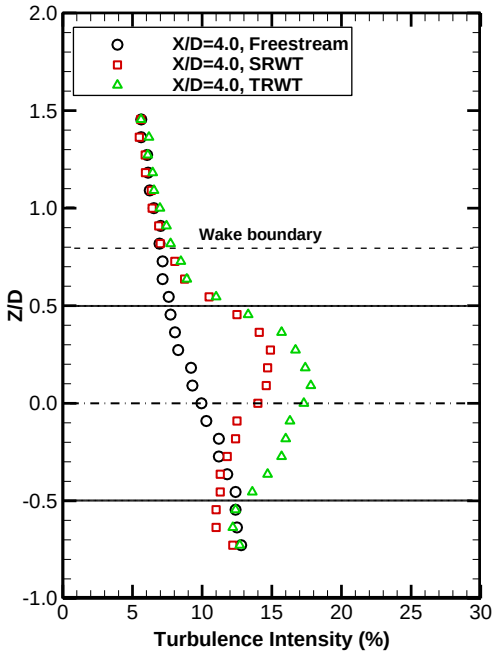

(b) X/D=4.0

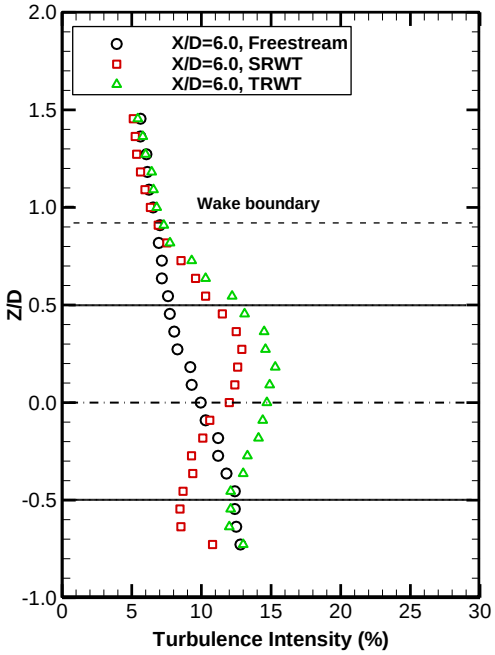

(c) X/D=6.0

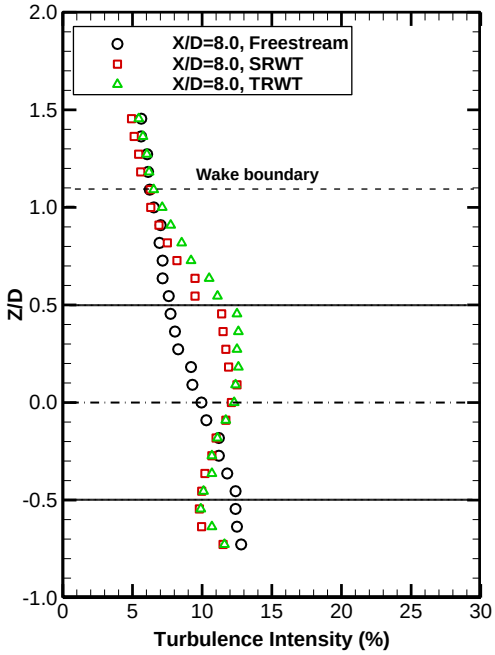

(d) X/D=8.0

Figure.12 Transverse profiles of the turbulent intensity in the far wakes behind the SRWT and TRWT models

As described above, with the smaller auxiliary rotor appended in front of the main rotor, the TRWT design would be able to harness more wind energy from the same incoming airflow by reducing the root losses of the main rotor blades. As a result, the incoming airflow would be decelerated more severely in the near wake behind the TRWT model, in comparison with that of the SRWT case, especially in the region near the roots of the main rotor blades. The greater velocity deficits in the near wake behind the TRWT model were also revealed quantitatively from the measurement results of the Cobra Probe Anemometry system at the downstream of location of *X/D*=2.0 given in Fig. 11(a). The measured turbulent intensity profiles given in Fig. 12(a) reveal clearly that the turbulent intensity levels in the wakes behind both the SRWT and TRWT models at the downstream location of X/D=2.0 were much higher than those of the incoming airflow. The elevated turbulent intensity levels in the turbine wakes are believed to be closely related to the generation and shedding of various unsteady vortex structures in the turbine wakes as visualized clearly in the phase-locked PIV measurements described above. It can also be seen that, corresponding to the more complicated wake vortex structures in the wake behind the TRWT model, the turbulent intensity level in the TRWT wake was found to be much higher than that behind the SRWT model at the same downstream location of *X/D*=2.0, especially in the region near the roots of the rotor blades. The higher turbulent intensity levels in the turbine wake would indicate more intensive turbulent mixing in the wake flow to promote a faster vertical transport process of kinetic energy from above to re-charge the turbine wake flow, as suggested by Wu et al. (2012), Calaf et al. (2010)and Cal et al. (2010). This would result in a faster recovery of the velocity deficits in the wake behind the TRWT model.

Since the TRWT design with an extra auxiliary rotor appended in front of the main rotor would generate more complicated wake vortex structures to enhance turbulent mixing in the wake flow, the velocity deficits in the far wake behind the TRWT model were found to recover much faster than those behind the SRWT model. As shown in Fig. 11(b), the flow velocity in the wake behind the TRWT model were found to become greater than those in the SRWT wake at the downstream location of X/D=4.0. It implies that, at the same downstream location of X/D=4.0, the TRWT wake flow would carry more kinetic energy in comparison with the SRWT case. A higher wind power generation can be expected for a downstream wind turbine sited in the wake behind a TRWT (i.e., mitigating wake losses), in comparison with the case with the same turbine sited in the wake of a SRWT. The measurement results given in Fig. 12(b) reveal that, while the turbulent intensity levels in the wake behind the TRWT model were still found to be much higher than those behind the SRWT model at the downstream location of X/D=4.0, the differences in the turbulent intensity profiles between the two TRWT and SRWT cases were found to become slightly smaller than those at the downstream location of X/D=2.0.

Due to the more intensive turbulent mixing in the TRWT wake flow induced by the extra auxiliary rotor, the flow velocity, thereby, kinetic energy of the wake flow behind the TRWT model at the downstream location of X/D=6.0 were found to become much greater than those of the SRWT case, as shown clearly in Fig. 11(c). The measured turbulence intensity profiles given in Fig. 12(c) reveal that, at the downstream location of X/D=6.0, while the turbulent intensity levels in the TRWT wake were still found to be higher than those of the SRWT case, the differences between the two cases were found to be much smaller compared with those at the upstream locations. This implies a shrinking differences

in the recovery of the velocity deficits in the wake flows between the two compared cases in the further downstream region of X/D>6.0.

As shown clearly in Fig. 11(d), with the downstream distance increase further to X/D=8.0, velocity deficits were still found to exist in the wake flows behind both the TRWT and SRWT models. It indicates that the flow velocity profiles in the turbine wakes have not fully recovered yet in comparison with that of the incoming airflow, even at the further downstream location of X/D=8.0. However, the differences in the transverse velocity profiles of the wake flows behind the TRWT and SRWT models were found to become much smaller at the downstream location of X/D=8.0. The measurement data given in Fig. 12(d) reveal that, while the absolute values of the turbulent intensity levels in the turbine wake flows were found to decrease greatly and become almost comparable to those of the incoming airflow, the turbulent intensity levels in the wake flows behind the two compared turbine models were found to become almost the same at the downstream location of X/D=8.0. Such measurement results indicates that the flow characteristics in the wakes behind the TRWT and SRWT model would become very similar at the further downstream region of X/D>8.0, which implies that the benefits of the TRWT design with additional auxiliary rotor to generate more complex wake vortex structures to augment turbulent mixing for a faster recovery of the velocity deficits in the turbine wake would die away gradually in the further downstream region of X/D>8.0.

In the present study, a set of experiments were also conducted to measure the power outputs of a conventional SRWT model sited right in the wakes behind the TRWT and SRWT model (i.e., aligned with the incoming airflow direction) at different downstream locations. The experimental study is aimed to simulate the worst scenario to experience the

greatest wake losses in wind farm settings as reported in Barthelmie et al. (2007b; 2009). Figure 13 gives the measured power outputs of the same downstream SRWT model sited in the wakes behind the TRWT and SRWT models as a function of the downstream distance away from the upstream turbine models. Following the work of Barthelmie et al. (2007b), the power outputs of the downstream turbine model were normalized by the power output of the same turbine model operating in isolation (i.e., without any wake effects from upstream wind turbines) in order to reveal the characteristics of the power losses of the downstream wind turbines due to wake effects in typical wind farm settings more clearly and quantitatively. As shown clearly in Fig. 13, corresponding to the significant velocity deficits in the wake flows behind the TRWT and SRWT models, the downstream turbine model was found to experience significant wake losses due to ingestion of the low-momentum wake flows. The wake losses were found to be as high as 60%~70% when the downstream turbine model was sited at about 2.0 rotor diameters away from the upstream turbine model (i.e., either SRWT or TRWT model). As revealed from the transverse velocity profiles given in Fig. 11, the velocity deficits in the turbine wakes would recover gradually as the downstream distance increases, the power loss of the downstream turbine due to the wake effects was found to become less and less as the downstream turbine being moved further away from the upstream turbines. As shown in Fig. 13, the power loss of the downstream turbine due to the wake effects was found to be about 35%, 27% and 23% when the distance between the upstream and downstream turbines for the SRWT case being about 7.0D, 9.4D and 10.5D. The results were found to agree well with the findings reported by Barthelmie et al. (2007b), who measured wake losses of conventional single-rotor wind turbines sited in Horns Rev offshore wind farm.

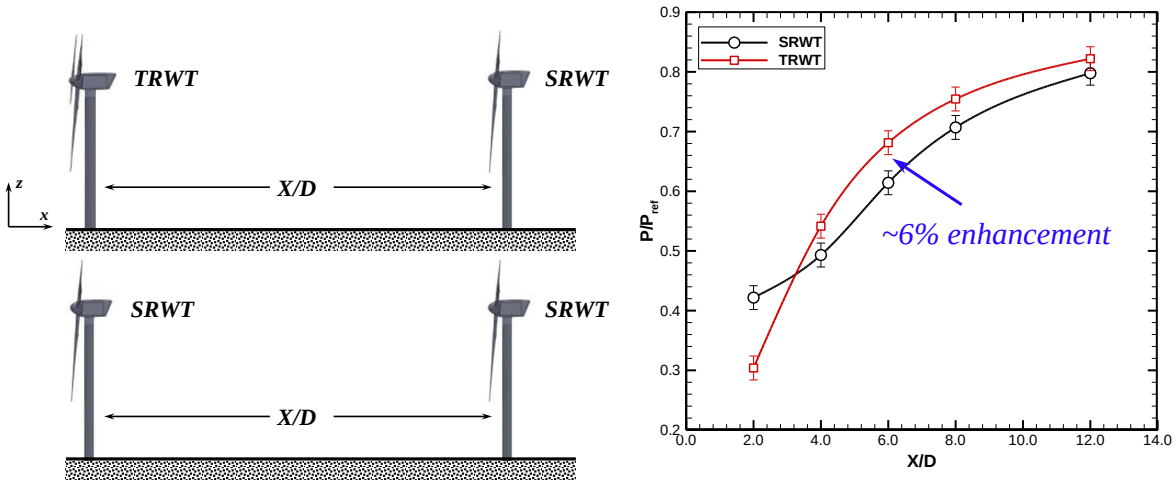

(a) Schematic of the locations for SRWT (b) Normalized power outputs

Figure.13 Power measurements of downstream turbine model sited in the wakes behind the SRWT and TRWT models

The feasibility of the TRWT design with an extra auxiliary rotor appended in front of the main rotor to reduce the wake losses in typical wind farm settings was also demonstrated clearly from the power measurement results given in Fig. 13. As revealed quantitatively from the PIV measurement results described above, due to the existence of the smaller, auxiliary rotor appended in front of the main rotor, the TRWT design would harness extra wind energy from the same incoming airflow (i.e., to reduce the roots losses in the region near the roots of the main rotor blades), in comparison to the SRWT design. As a result, the velocity deficits in the near wake behind the TRWT model were found to be much more significant than those behind the SRWT model. As expected, corresponding to the much lower momentum of the TRWT wake flow in the near wake region, the downstream turbine was found to have less power output when sited at the downstream location of the X/D=2.0 behind the TRWT model, in comparison with that in the SRWT wake. However, since the TRWT design with

an extra auxiliary rotor can generate more complicated wake vortex structures to augment turbulent mixing in the TRWT wake flow, the velocity deficits in the wake behind the TRWT model were found to recovery much faster in the far wake region than that in the SRWT wake. As shown in Fig. 11(b), the magnitude of the flow velocity of the TRWT wake at the downstream location of X/D=4.0 was found to become greater than that in the SRWT wake due to the much faster recovery of the velocity deficits in the far wake behind the TRWT model. Corresponding to the higher flow velocity, thereby more kinetic energy, in the TRWT wake at the downstream location of X/D=4.0, the same downstream turbine model was found to be able to produce about 5% more power when sited in the wake behind the TRWT model, in comparison with that behind the conventional SRWT model at the same downstream location of X/D=4.0. It indicates that the TRWT design with an extra auxiliary rotor appended in front of the main rotor would not only be able to harness extra wind energy from the same incoming airflow (i.e., by reducing the root losses in the region near the roots of the main rotor blades), but also be capable of mitigating wake losses of downstream turbines in typical wind farm settings, in comparison with those of the conventional SRWT design.

The measurement results given in Fig. 13 also reveals that, the benefits of the TRWT design in reducing the wake losses of the downstream turbines would be maximized when the downstream turbine model was mounted at about 6.0 rotor diameters downstream away from the upstream TRWT model, where the same downstream turbine model was found to be able to generate about 6% more power when sited in the TRWT wake, in comparison with that in the SRWT wake at the same downstream location of X/D=6.0. With the downstream turbine model moving further away from the upstream turbine model, the advantage of the TRWT design over the conventional SRWT design in reducing the wake losses of the

downstream turbines was found to decrease gradually, and the difference in the downstream turbine power outputs between the two compared cases were found to become about 2.5% when the same downstream turbine model was moved to 12 rotor diameters away from the upstream wind turbine models (i.e., at downstream location of X/D=12). The smaller and smaller benefits of the TRWT design in mitigating the wake losses of the downstream turbines sited in the far wake region of X/D>6.0 was found to be correlated well with the continually shrinking differences in the wake flow velocity and turbulent intensity profiles behind the TRWT and SRWT models in the far wake region of X/D>6.0 as shown in Fig. 11 and Fig. 12. It should be note that, the distance between the upstream and downstream wind turbines is about 7 ~ 10 rotor diameters in a typical offshore wind farm as reported in Barthelmie et al. (2007b), the TRWT design with an extra auxiliary rotor appended in front of the main rotor would be able to reduce the wake losses of the downstream turbines by 4% ~ 6%, in comparison with the conventional SRWT design.

4.3.4. Stereoscopic PIV measurements

It is well known that a 2-D PIV system is only capable of obtaining the projection of velocity components perpendicular to the camera lenses, which means the out-of-plane velocity component is lost while the in-plane components could be influenced by an unrecoverable error due to the perspective transformation (Prasad et al., 1993). As the turbulent wake behind a scaled wind turbine is a highly three-dimensional flow field, the 2-D PIV measurements may not be capable of identifying the three-dimensional flow structures successfully. Thus, a high-resolution Stereoscopic PIV (SPIV) system was also employed in the present study to measure the three velocity components (u,v,w) at several pre-selected vertical planes (Y-Z planes) perpendicular to the central plane (used in 2-D PIV

measurements) in the turbulent wake. Figure 14 illustrates the set-up used for SPIV, two PCO cameras equipped with two 105mm lenses were arranged at the downstream side of the laser sheet. Similar to the 2-D PIV measurements, "free-run" and "phase-locked" measurements were acquired and processed to analyze the flow quantities in the wind turbine wake.

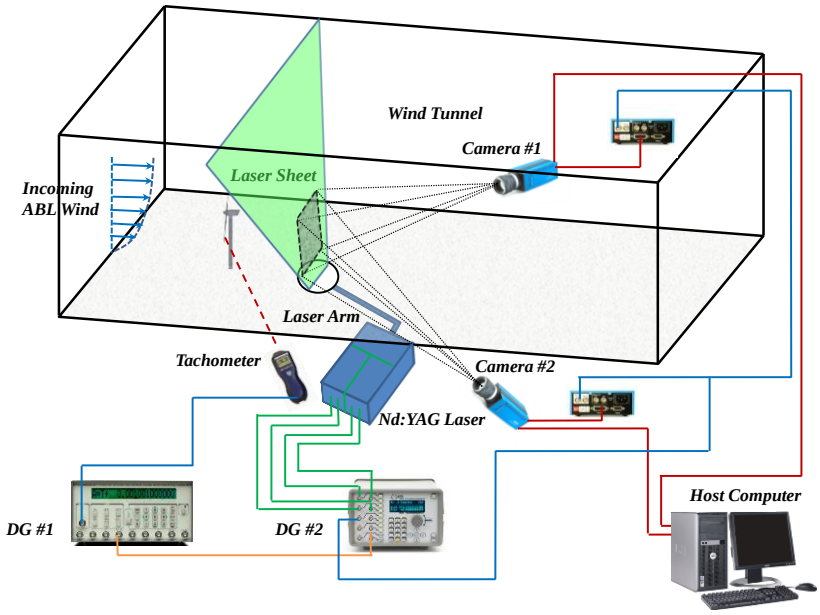

Fig.14 Experimental setup used for Stereoscopic PIV measurements

Figures 15 and 16 depict the "phase-locked" velocity distributions at four pre-selected rotation phase angles (i.e., θ=0, 30, 60 and 90 deg) of the turbine rotor blades in the wakes of X/D=1.0 for the SRWT and TRWT models, respectively. The contour in the figure indicates the streamwise velocity and the arrows represent the transversal velocity distributions. As the phase angle increases, the turbine blades would rotate in anti-clockwise direction. High velocity deficits behind the wind turbine models can be found occurred in the central region. The streamwise velocity distributions are found to be increased gradually from center to the outside region of the rotation disk in the turbulent wake of wind turbine models. The difference between the low-momentum flow and the high-momentum flow creates a shear

layer in the wake which is made up of concentrated vortices, corresponding to the measurements visualized by 2-D PIV in Fig. 10. The vector arrows, indicating the transversal velocity, demonstrate the rotational direction of the wake in opposite to the rotor inside the shear layer. It is affected mildly at the outside region of the shear layer due to the rotor rotation. Similar results can be found in the experimental investigations conducted by Bartl et al. (2012) and Schümann et al. (2013).

As shown clearly in Fig.15, the blade position would significantly influence the transversal velocity (e.g., magnitude and direction) in the shear layer, which could be induced by the strong turbulent wake mixing in this region. However, the blade position doesn't demonstrate a significant impact on the streamwise velocity distribution, and similar results can also be observed in Fig.16. The magnitude of transversal velocity in the turbulent wake of TRWT model is considerably higher than that of SRWT model, which can be easily inferred the reason is due to the existence of the auxiliary rotor blades appended in front of the main rotor. Meanwhile, smaller streamwise velocity deficit can be found in the SRWT case in comparison to the TRWT case, which indicates more energy from the incoming flow is harnessed and reproduces the same phenomenon shown in Fig.6. Higher transversal velocity could be beneficial for re-charge the high-momentum airflow above the rotational disk into the turbulent wake of TRWT model.

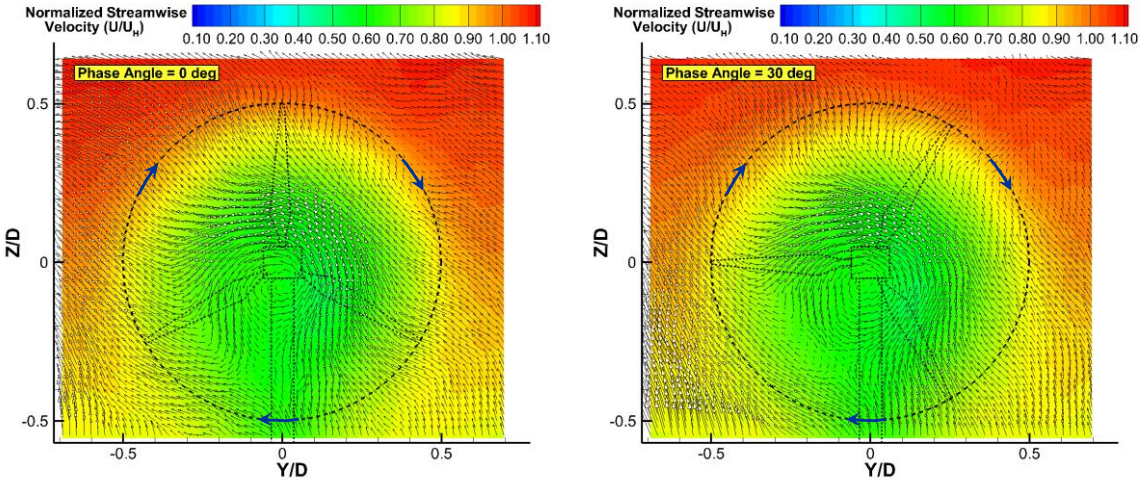

(a) θ=0 deg (b) θ=30 deg

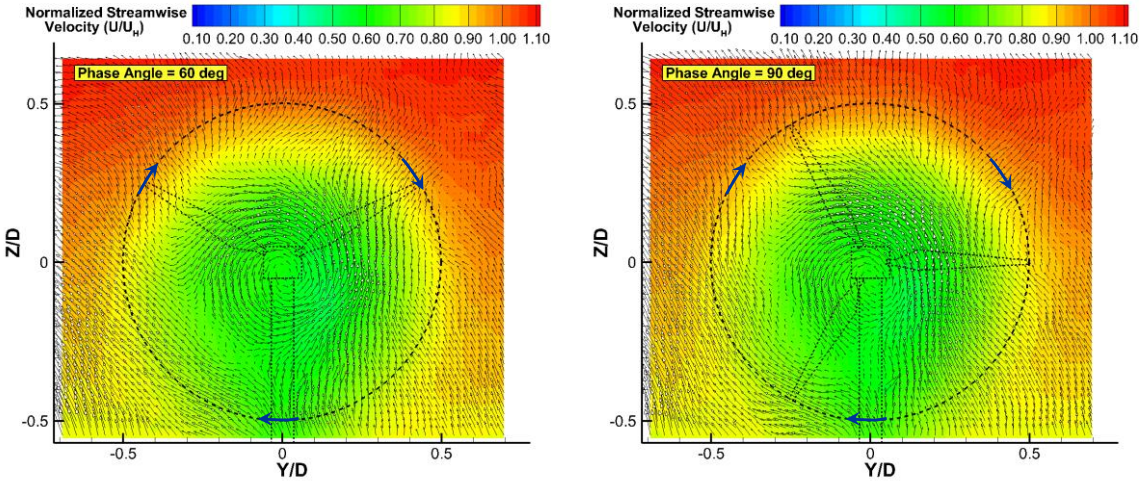

(c) θ=60 deg (d) θ=90 deg

Fig.15. Phase-locked flow velocity distributions at X/D=1.0 in the wake for the SRWT

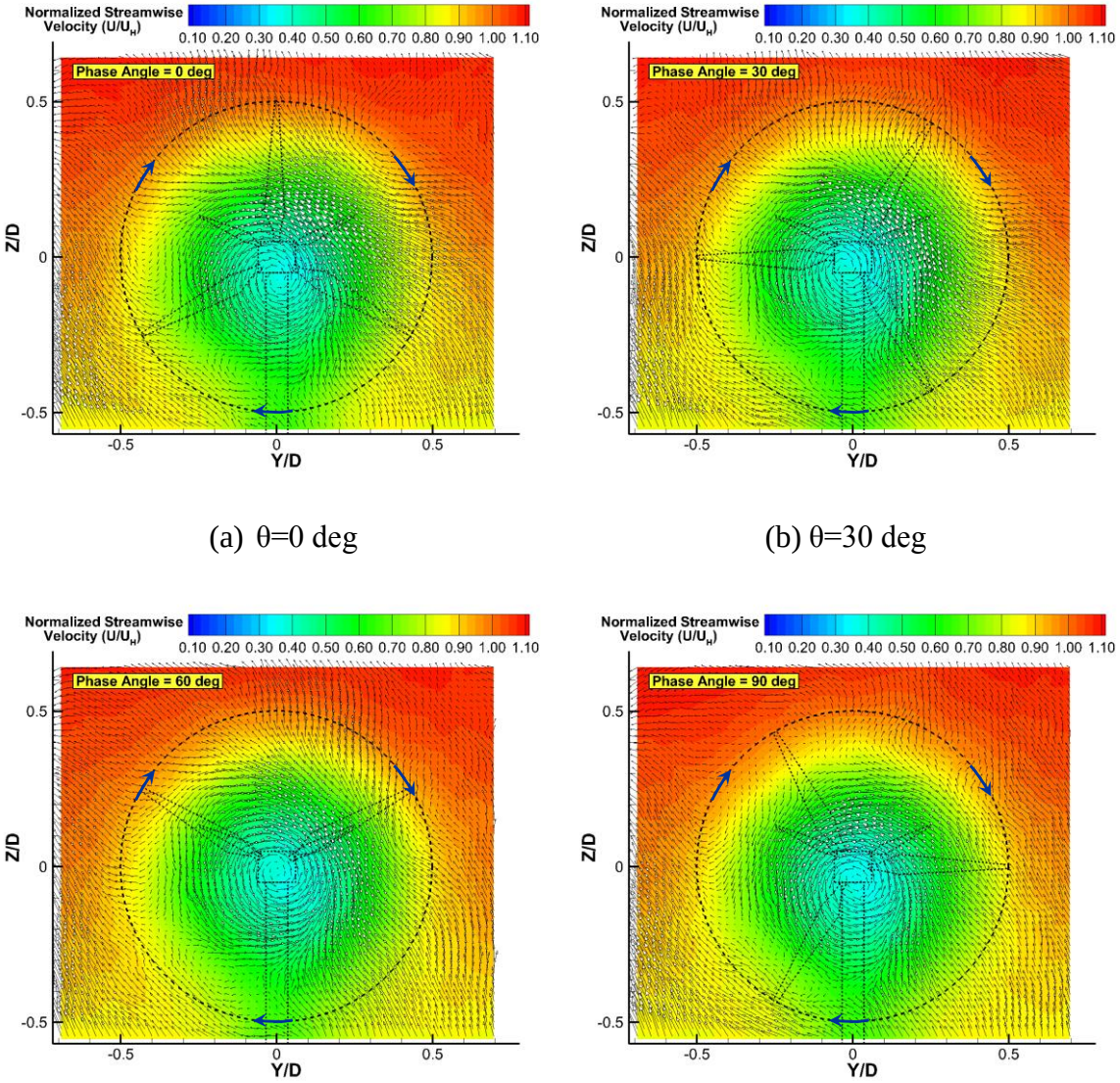

(a) θ=0 deg (b) θ=30 deg

(c) θ=60 deg (d) θ=90 deg

Fig.16. Phase-locked flow velocity distributions at X/D=1.0 in the wake for the TRWT

Figure 15 and 16 only showed the instantaneous results at the downstream location in the turbulent wake of X/D=1.0, the time-averaged solutions also need to be obtained for analyzing the ensemble-averaged flow quantities. Figure 17 compares the time-averaged velocity distributions at four pre-selected streamwise locations (i.e., X/D=0.5, X/D=1.0, X/D=2.0 and X/D=4.0) in the turbulent wakes of wind turbine models, which represent the measuring locations from the near wake to the far wake. As expected, the velocity deficit in

the region behind the small-rotor rotational disk in the near wake (X/D≤2.0) of the TRWT case is much larger than that of the SRWT case, which can be inferred that more airflow energy in the central region is harvested by the secondary small rotor. Also, the downstream wake can be observed clearly expands gradually from the near wake to far wake region. However, compared to a much higher velocity deficit exists in the near wake region of the TRWT case, the streamwise velocity can recover to a similar level with the SRWT case when X/D=4.0, which demonstrates that the TRWT has a better ability for entraining the high-momentum airflow into the wake region through the stronger wake mixing.

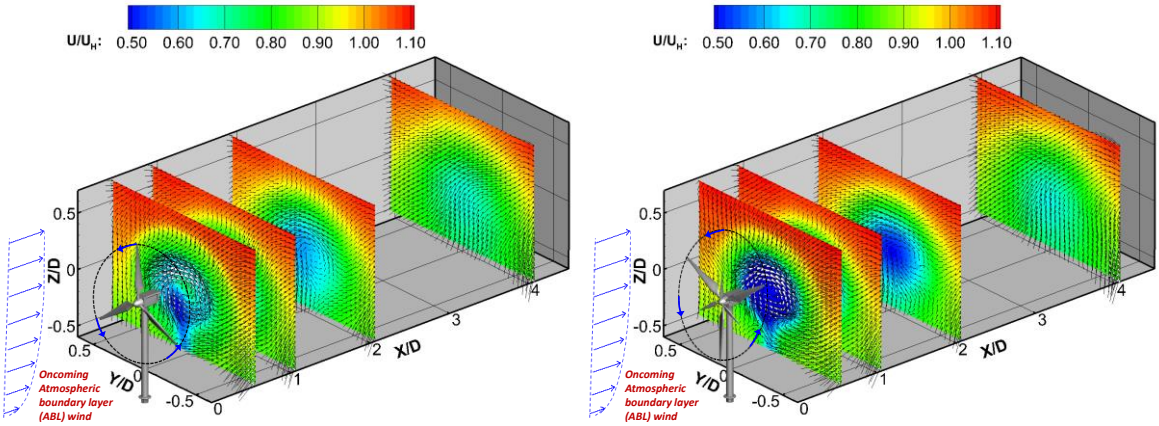

Fig.17. Ensemble-averaged velocity distributions in the wake of SRWT (left) and TRWT (right) models

In order to compare the effects induced by the secondary small-rotor more clearly, the normalized TKE ($TKE = 0.5(\overline{u'^2} + \overline{v'^2} + \overline{w'^2})/U_H^2$) distributions from the near wake (X/D=0.5) to far wake (X/D=4.0) for the SRWT and TRWT cases are illustrated in Figure 18, which can be used as an important parameter to indicate the extent of turbulent mixing in a turbulent flow (Tian et al., 2014). It should be noted that, since all of the three velocity components can be achieved by SPIV technique, the TKE for this measurement can be calculated by using the velocity fluctuations of *u*, *v* and *w* instead of only using *u* and *v* in 2-D PIV

measurements. As shown apparently in the figure, the normalized high TKE levels are found to be concentrated along the shedding path of the tip vortex structures in the near wake region (i.e., X/D=0.5) for both of the wind turbine models, which generates half "cycle-shaped" flow structure on the measuring planes. Meanwhile, the TKE levels in the region behind the tower and nacelle are highly turbulent due to the flow separation around them. However, the TKE levels in the far wake region (i.e., X/D≥2.0) of the TRWT case are observed much higher than those of the SRWT case due to the stronger mixing by the wake induced from the main rotor and the small rotor. As suggested by Tian et al. (2014), the much higher TKE levels would indicate more intensive wake mixing in the downstream region, which corresponds to a much faster velocity recovery in the turbulent wake of the TRWT case. This result has a good consistency with the velocity comparison shown in Figure 18, where the streamwise velocity in the central region of the near wake (X/D=0.5) in the TRWT case is much lower but is recovered to a similar level in the far wake region of the SRWT case (X/D=4.0).

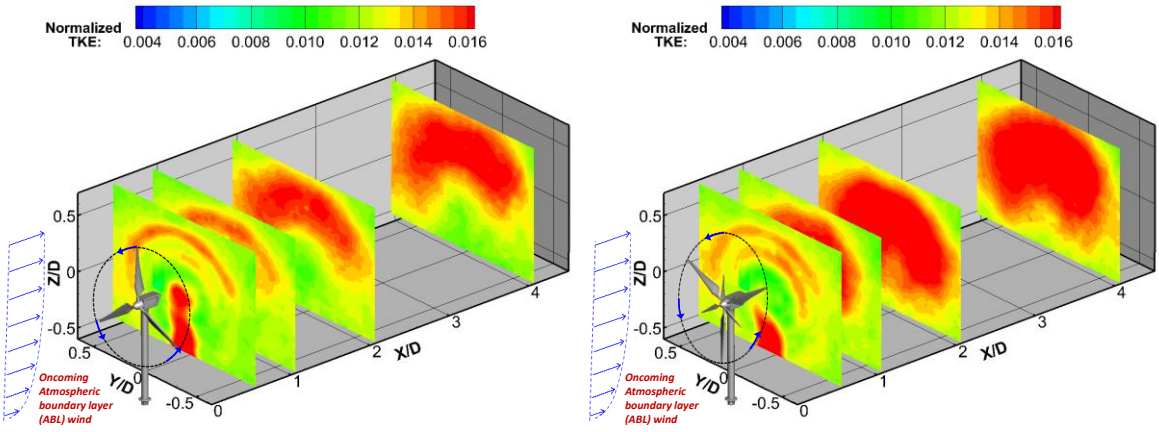

Fig.18. Ensemble-averaged TKE distributions in the wake of SRWT (left) and TRWT (right) models

4.4. Conclusion

An experimental study was conducted to explore a novel twin-rotor wind turbine (TRWT) concept for improved aerodynamic performances of isolated wind turbines as well as better wind farm efficiency. Unlike conventional single-rotor wind turbine (SRWT) designs, the TRWT design employs an extra set of smaller, co-axial auxiliary rotor blades appended in front of the main rotor blades with two objectives: 1) reduce root losses incurred in the root region of the main rotor blades; and 2) mitigate wake losses of downstream turbines in wind farm settings through enhanced turbulent mixing of turbine wake. The increased power generation capacity of the TRWT design can also be availed to extract energy at wind speeds below the current cut-in speeds.

The experimental study was performed in a large-scale wind tunnel with scaled TRWT and SRWT models placed in the same incoming boundary layer airflow under neutral stability conditions. In addition to measuring the dynamic wind loads acting on the model turbines, a high-resolution PIV system was used to make both "free-run" and "phase-locked" measurements to quantify the flow characteristics and behavior of the unsteady wake vortices (i.e., formation, shedding, breakdown and dissipation) in the near wakes behind the TRWT and SRWT models. A Cobra Probe Anemometry system was also used to conduct velocity measurements in the far wake flows (i.e., in the downstream region of $X/D \geq 2.0$) to supplement the near wake PIV measurements. Furthermore, the power outputs of a model turbine sited in the wake behind the TRWT model at different downstream locations were also measured and compared quantitatively with those of the same model turbine sited in the wake behind the SRWT model.

The measurement results reveal clearly that, while the TRWT design with an extra auxiliary rotor appended in front of the turbine main rotor was found to be capable of harvesting more wind energy from the same incoming boundary layer flow by reducing the root losses of the main rotor blades, the dynamic wind loads acting on the TRWT model were also found to be much greater (i.e., ~ 16% increase in time-averaged wind loads, up to 140% increase in the fluctuating amplitudes of the instantaneous wind loads) than those acting on the SRWT model. The much larger fluctuating amplitudes of the dynamic wind loads would indicate more significant fatigue loads acting on the TRWT model, which is believed to be closely related to the more complex vortex structures generated in the wake behind the TRWT model due to the existence of the extra auxiliary rotor.

It was also found that, due to the existence of the additional auxiliary rotor appended in front of the main rotor, significant differences in flow characteristics (i.e., much larger velocity deficits in the near wake, more complex wake vortex structures, earlier breakdown of the concentrated wake vortices, and higher TKE and turbulent Reynolds stress levels) were found in the near wake behind the TRWT model, in comparison with those in the near wake behind the SRWT model. Thanks to the more complex wake vortices generated behind the TRWT model, the turbulent mixing process in the TRWT wake flow was found to be enhanced greatly, which would promote the vertical transport of kinetic energy by entraining more high-speed airflow from above to re-charge the low momentum wake flow and resulting in a much faster recovery of the velocity deficits in the wake behind the TRWT model. Therefore, the wake flow behind the TRWT model was found to become more energetic in the far wake region of X/D>3.0 than that behind the SRWT model. As a result, the power output of a downstream turbine sited in the far wake behind the TRWT model was

found be substantially greater than that of the same turbine sited in the wake behind a conventional SRWT model (i.e., up to 7% more power output for the same downstream turbine when it sited at 6.0 rotor diameters away from the upstream turbine). It indicates that the TRWT design with an extra auxiliary rotor appended in front of the main rotor would not only be able to harvest more energy from the same incoming wind by reducing the root losses, but also can mitigate the wake losses of the downstream turbines in typical wind farm settings through enhanced turbulent mixing of the turbine wake flows.

It should be noted that, while the TRWT design were demonstrated to be capable of improving wind turbine performance by reducing the root losses and increasing wind farm efficiency by mitigating wake losses of downstream turbines in typical wind farm settings, the present experimental study was conducted in a wind tunnel with scaled TRWT and SRWT models. The corresponding Reynolds number of the scaled turbine models is about 2~3 orders lower than those of the utility-scale wind turbines due to the inherent limitations of the wind tunnel tests with scaled model turbines.

The phase-locked flow fields at the downstream location in the turbulent wake of X/D=1.0 measured by stereoscopic PIV technique revealed that, higher streamwise velocity deficit can be found in the central region of TRWT model and the blade phase angle location would have obvious impact on the distributions of transversal velocity. Much higher TKE levels in the wake of TRWT model would indicate more intensive wake mixing in the downstream region, which corresponds to a much faster velocity recovery in the turbulent wake. We believe that the findings derived from the present study are very helpful to gain further insight into aeromechanic characteristics of wind turbines, more comprehensive

researches are still needed to explore/optimize design paradigms for higher power yield and better durability of wind turbines.

Acknowledgements

The funding support from the Iowa Energy Center with Grant No. 14-008-OG and National Science Foundation (NSF) with Grant Numbers of CBET-1133751 and CBET- **1438099** is gratefully acknowledged.

References

Adaramola, M. S., & Krogstad, P.-Å. (2011). Experimental investigation of wake effects on wind turbine performance. *Renewable Energy*, *36*(8), 2078–2086.

Barthelmie, R. J., Folkerts, L., Ormel, F. T., Sanderhoff, P., Eecen, P. J., Stobbe, O., & Nielsen, N. M. (2003). Offshore Wind Turbine Wakes Measured by Sodar. *Journal of Atmospheric and Oceanic Technology*, *20*(4), 466–477.

Barthelmie, R. J., Hansen, K., Frandsen, S. T., Rathmann, O., Schepers, J. G., Schlez, W., … Chaviaropoulos, P. K. (2009). Modelling and measuring flow and wind turbine wakes in large wind farms offshore. *Wind Energy*, *12*(5), 431–444.

Barthelmie, R. J., & Jensen, L. E. (2010). Evaluation of wind farm effi ciency and wind turbine wakes at the Nysted offshore wind farm, (June), 573–586.

Barthelmie, R. J., Rathmann, O., Frandsen, S. T., Hansen, K. S., Politis, E., Prospathopoulos, J., Pijl, S. P. Van Der. (2007a). Modelling and measurements of wakes in large wind farms. *Journal of Physics: Conference Series*, *75*, 012049.

Barthelmie, R. J., Rathmann, O., Frandsen, S. T., Hansen, K. S., Politis, E., Prospathopoulos, J., Pijl, S. P. Van Der. (2007b). Modelling and measurements of wakes in large wind farms. *Journal of Physics: Conference Series*, *75*, 012049.

Bartl, J., Pierella, F., & Sætran, L. (2012). Wake measurements behind an array of two model wind turbines. *Energy Procedia*, *24*(1876), 305–312.

Cal, R. B., Lebrón, J., Castillo, L., Kang, H. S., & Meneveau, C. (2010). Experimental study of the horizontally averaged flow structure in a model wind-turbine array boundary layer. *Journal of Renewable and Sustainable Energy*, *2*(1), 013106.

Calaf, M., Meneveau, C., & Meyers, J. (2010). Large eddy simulation study of fully developed wind-turbine array boundary layers. *Physics of Fluids*, *22*(1), 015110.

Castillo, L., Kang, H. S., Meneveau, C., & Sardella, L. M. (2010). Interaction Between a Wind Turbine Array and a Turbulent Boundary Layer, (January), 1–10.

Chamorro L., Arndt R., & Sotiropoulos, F. (2011). Turbulent Flow Properties around a staggered wind farm. *Boundary-Layer Meteorology*, *141*(3), 349–367.

Chamorro, L. P., & Porté-Agel, F. (2010). Effects of Thermal Stability and Incoming Boundary-Layer Flow Characteristics on Wind-Turbine Wakes: A Wind-Tunnel Study. *Boundary-Layer Meteorology*, *136*(3), 515–533.

Hansen, K. S., Barthelmie, R. J., Jensen, L. E., & Sommer, A. (2012). The impact of turbulence intensity and atmospheric stability on power deficits due to wind turbine wakes at Horns Rev wind farm, (November 2011), 183–196.

Hu, H., Yang, Z., & Sarkar, P. (2012). Dynamic wind loads and wake characteristics of a wind turbine model in an atmospheric boundary layer wind. *Experiments in Fluids*, *52*(5), 1277–1294.

Jain, P. (2007). *Wind energy engineering*. McGraw Hill Professional.

Lignarolo, L. E. M., Ragni, D., Ferreira, C. J. S., & van Bussel, G. J. W. (2014). Kinetic energy entrainment in wind turbine and actuator disc wakes: an experimental analysis. *Journal of Physics: Conference Series*, *524*, 012163.

Medici, D. (2005). Experimental studies of wind turbine wakes : power optimisation and meandering. KTH.

Medici, D., & Alfredsson, P. H. (2006). Measurements on a wind turbine wake: 3D effects and bluff body vortex shedding. *Wind Energy*, *9*(3), 219–236.

Meyers, J., Lee, J., & Schwartz, R. (2001). Characterization of measurement error sources in Doppler global velocimetry. *Measurement Science and Technology*.

Okulov, V. L., & Sørensen, J. N. (2008). Refined Betz limit for rotors with a finite number of blades. *Wind Energy*, *11*(4), 415–426.

Prasad, A. K., & Adrian, R. J. (1993). Stereoscopic particle image velocimetry applied to liquid flows. *Experiments in Fluids*, *15*(1), 49–60.

Rosenberg, a, Selvaraj, S., & Sharma, a. (2014). A Novel Dual-Rotor Turbine for Increased Wind Energy Capture. *Journal of Physics: Conference Series*, *524*, 012078.

Schümann, H., Pierella, F., & Sætran, L. (2013). Experimental investigation of wind turbine wakes in the wind tunnel. *Energy Procedia*, *35*(1876), 285–296.

Sharma, A. and Frere, A. (2010). Diagnosis of Aerodynamic Losses in the Root Region of a Horizontal Axis Wind Turbine. *General Electric Global Research Center Internal Report*.

Tian, W., Ozbay, A., & Hu, H. (2014). Effects of incoming surface wind conditions on the wake characteristics and dynamic wind loads acting on a wind turbine model. *Physics of Fluids*, *26*(12), 125108.

Tian, W., Ozbay, A., Hu, H., Sarakar, P., & Yuan, W. (2013). An experimental study on the performances of wind turbines over complex terrain. *51st AIAA Aerospace Sciences Meeting Including the New Horizons Forum and Aerospace Exposition 2013*, (January),

Tong, W. (2010). *Wind power generation and wind turbine design*. Wit Press.

Newman, B. G. (1986). Multiple Actuator-disc Theory for Wind Turbines. *Journal of Wind Engineering and Industrial Aerodynamics*, *24*, 215–225.

Varshney, K. (2012). Characteristics of helical tip vortices in a wind turbine near wake. *Theoretical and Applied Climatology*, *111*(3-4), 427–435.

Vermeer, L. J., Sørensen, J. N., & Crespo, a. (2003). Wind turbine wake aerodynamics. *Progress in Aerospace Sciences*, *39*(6-7), 467–510.

Whale, J., Anderson, C. ., Bareiss, R., & Wagner, S. (2000). An experimental and numerical study of the vortex structure in the wake of a wind turbine. *Journal of Wind Engineering and Industrial Aerodynamics*, *84*(1), 1–21.

Wu, Y. T., & Porté-Agel, F. (2011). Large-Eddy Simulation of Wind-Turbine Wakes: Evaluation of Turbine Parametrisations. *Boundary-Layer Meteorology*, *138*(3), 345–366.

Wu, Y.-T., & Porté-Agel, F. (2012). Atmospheric Turbulence Effects on Wind-Turbine Wakes: An LES Study. *Energies*, *5*(12), 5340–5362.

Yang, Z., Sarkar, P., & Hu, H. (2012). Visualization of the tip vortices in a wind turbine wake. *Journal of Visualization*, *15*(1), 39–44.

Zhang, W., Markfort, C. D., & Porté-Agel, F. (2013). Wind-Turbine Wakes in a Convective Boundary Layer: A Wind-Tunnel Study. *Boundary-Layer Meteorology*, *146*(2), 161–179.

CHAPTER 5. AN EXPERIMENTAL STUDY ON THE WAKE CHARACTERISTICS BEHIND INNOVATIVE DUAL-ROTOR WIND TURTINES

Zhenyu Wang, Ahmet Ozbay, Wei Tian, Anupam Sharma, Hui Hu

Department of Aerospace Engineering, Iowa State University

Abstract： An experimental study was performed to investigate the wake characteristics and aeromechanic performance of an innovative dual-rotor wind turbine (DRWT) with co- and counter-rotating configurations, in comparison with those of a traditional single-rotor wind turbine (SRWT). The comparative study was performed in a large-scale Atmospheric Boundary Layer (ABL) wind tunnel with the scaled DRWT and SRWT models under neutral stability conditions. In addition to measuring the dynamic wind loads acting on the wind turbine models, a high-resolution 2-D PIV system and a Cobra Probe Anemometry system were also used to quantify the instantaneous and time-averaged flow quantities of the wake flows behind the wind turbine models. The power outputs from the isolated SRWT and DRWT wind turbines and a duplicate wind turbine model operating in the turbulent wakes behind the SRWT and DRWTs were also observed and compared quantitatively. Furthermore, a stereoscopic PIV system was used to measure the three velocity components of the wake flow behind the wind turbine models. The measurement results reveal clearly that the DRWT designs are capable of harnessing more wind energy than the SRWT design from the same incoming air flow by reducing the root losses incurred in the root region of the main rotor blades. Detailed wake flow field analysis (both of the “free-run” and “phase-locked” measurements) was performed in order to quantify the characteristics of the turbulent turbine wake flows and to visualize the transient behavior of the unsteady vortex structures behind the wind turbine models. The detailed flow field measurements were correlated with

the dynamic wind loads and power outputs to elucidate the underlying physics for higher total power generation and better durability of the wind turbines.

5.1. Introduction

Horizontal-axis wind turbine (*HAWT*) design is widely used for utility-scale turbines in modern onshore and offshore wind farms due to its reliability and durability. Most of HAWTs are of single-rotor design with three long rotating blades mounted on a hub in front of the turbine nacelle. The rotating blades are aerodynamically optimized in outboard sections in order to guarantee a good aerodynamic performance. However, the blade sections near inboard region (approximately bottom 25% of the span) are primarily designed for supporting structural loads. Hence, very high thickness-to-chord airfoils with poor aerodynamic performance are used in this region to ensure structural integrity. Such a configuration results in a very low energy-harvest zone near the root region where virtually very little wind energy can be harnessed from the incoming airflow. Besides, flow separation would occur in the root region when the rotor blades rotate during operation, which could cause span-wise (cross) flow deteriorating the aerodynamic performance of the outboard blade sections as well (Rosenberg et al, 2014). Up to 5% loss in wind energy extraction capability is estimated per turbine for the compromise of structural constraint (Sharma et al, 2010). These losses are enormous especially when contrasted with the electric power generated per year in the world by wind turbines.

A wind farm usually consists of a number of wind turbines arranged in organized topologies such as aligned or staggered patterns. A portion of the wind energy in the incoming airflow is harnessed by the upstream wind turbines as the airflow passes through the rotor blades, causing significant velocity deficits in the wake flows behind these turbines.

Therefore, downstream turbines see a considerably lower incoming airflow velocity than the upstream turbines, and thus, less wind energy is available for the downstream turbines. As a result, the power extractions from downstream wind turbines would be significantly lower than those of upstream wind turbines, which are also called *wake losses*, and have been found to be in the range of 20% ~ 40% in typical wind farms (Barthelmie et al., 2007, 2009, 2010; Storm et al., 2009). The reasons for the exceptionally wide range in wake losses are influenced by factors such as locations and layouts of wind farms, and atmospheric stability conditions. Highest wake losses have been found in offshore wind farms when turbine rows are aligned with wind direction, have a close spacing, and the atmospheric flow is stably stratified (Barthelmie et al., 2007, 2010; Hansen et al., 2012).

Wind turbine wakes, typically, can be divided into a near wake (i.e., up to one rotor diameter downstream) and a far wake (i.e., beyond the near wake region) (Vermeer et al., 2003). The rotor blades, tower and nacelle configurations as well as the flow structures such as stalled flows, Karman vortices and tip vortices shed from the wind turbines have significant impact in the near wake. However, the actual wind turbine geometry has less effect in the far wake, which is more concerned on the issues such as wake interferences/interactions and wake models. Ross et al. (1981) conducted an experimental study to investigate the wake flows in a set of wind turbine models by using Laser Doppler Anemometry technique. They observed that in the turbine wake the velocity deficit can be recovered up to around 50% within the first two rotor diameters behind the upstream turbines. Following this region, the velocity deficit was then recovered gradually to reach 70% and 75% at the downstream distances of 6*D* and 8*D*, respectively. Barthelmie et al. (2003) reported that, with the spacing between the wind turbines in the offshore wind farms

being 1.7*D* to 7.4*D*, the wake velocity deficit recovery that can range from 10% to 45%, but with a very slow recovery for the spacing beyond 6.5D. Tian et al. (2014) also carried out a comprehensive experimental study to investigate the effects of turbulence intensity of the incoming ABL winds on the recovery rate of the wake velocity deficits behind wind turbines. They observed that the velocity deficits would recover much faster in the incoming flow with a higher turbulence level (i.e., for the cases in typical onshore wind farms), compared to that in the incoming airflow with relatively low turbulence level (i.e., for the cases in typical offshore wind farms). Hu et al. (2012) studied the evolution of the unsteady vortex and turbulent flow structures in the near wakes of wind turbines placed in nonhomogeneous boundary layer airflows with rather high turbulence intensity levels. Based on the previous investigations, it can be easily found that the recovery rate of the velocity deficits and the turbulence characteristics of the turbine wake flows would significantly affect the power production and wind loadings acting on the downstream wind turbines.

While the significance of the "root" and "wake" losses is evident and large amounts of work have been dedicated to predict and measure wake or root losses, relatively very little research can be found in literature to explore effective strategies for root loss reduction or/and wake loss mitigation. In order to increase the energy conversion efficiency of wind turbines, many different concepts and blade designs have been proposed to improve the maximum power coefficient of wind turbines in the past few decades (Hau et al., 2000). Due to cost considerations, multi-stage designs (e.g., dual-rotor turbines) of *HAWTs* have received little attention. However, multi-stage turbomachineries are widely used in the gas turbine and propulsion industries in order to maximize the efficiency of fossil fuel usage. Since the "fuel" for wind turbines in nature is supposedly free, the cost of electricity production, instead of

efficiency, leads to current wind turbine designs. With the concerns that we will run out of sites (land or ocean) where we can realistically install wind turbines, the focus has to therefore shift towards high-efficiency turbine and wind farm designs to harvest higher power per square meters of surface area.

The maximum energy conversion efficiency for a traditional SRWT is around 59% according to the Betz Limit, but in reality, the best utility-scale SRWT can only harness up to 40% of the energy from the incoming airflow because of various associated losses such as viscous loss, 3-D loss and transmission loss (Lee et al., 2012). As a result, approximately 60% of the potential energy from the incoming wind is not harvested by SRWT systems. A dual-rotor wind turbine design is a promising strategy to enhance the energy conversion efficiency by using two identical rotors installed on the upwind and downwind sides of the wind turbine nacelle. This design allows for an extra portion of the unused wind energy to be extracted by installing a second rotor on the same tower. Newman (1986) calculated that the maximum Cp that an identical size dual-rotor wind turbine (DRWT) could reach was 0.64, almost an 8% enhancement compared to the Betz limit for conventional SRWT. But further addition of rotor stages would give diminishing returns. Lee et al. (2010, 2012) compared the aerodynamic characteristics of a SRWT and Counter-rotating dual-rotor wind turbine (CN-DRWT) by using numerical method. Through the comparisons of maximum power coefficients, the efficiency of a CN-DRWT was seen to be 30% more than a SRWT with half the solidity but was shown to be 5% less than a SRWT with equal solidity. Later, they found that the aerodynamic performance of the CN-DRWT can be improved by varying the combinations of pitch angles, the rotating speed ratio, and the radius difference of the two rotors. Recently, people recognized that the inner 30% portion of the main rotor can be

treated as dead zone, because it plays a less significant role in generating torque due to the low sweeping speed in this region of the blade (Jung et al., 2005). Jung built a CN-DRWT system consisting of two separate rotors: the main rotor and an auxiliary rotor. The diameter of the auxiliary rotor is half of the main rotor diameter, which is used to compensate for the dead zone in the main rotor area but also generating additional torque for the whole system. It was found that the flow velocity becomes reduced in the inner region (30% of the main rotor diameter) and thus less power is obtained. However, the flow would accelerate substantially and this increased flow velocity helps to generate more torque for the main rotor. The total power increase for the CN-DRWT system is about 20% in comparison with the baseline SRWT configuration. More recently, Yuan et al. (2014) conducted an experimental study to evaluate the effects of the relative rotation directions of a dual-rotor wind turbine on their power production performances. They found that the downwind turbine in the near wake of the upwind turbine could harness the additional kinetic energy associated with the swirling velocity of the wake flow of the upwind turbine when the two turbines are set to rotate in opposite directions. As a result, the turbines in the counter-rotating configuration would harvest more wind energy from the same incoming wind compared to the co-rotating configuration.

Based on the previous studies of DRWT model, a dual-rotor design can be used for harnessing more energy from the incoming wind. However, the shortages of the current design such as the poor aerodynamic performance in the downwind turbine and the root losses incurred in near hub region for both of the rotor blades should be addressed. As a result, this design is still ineffective and more effective design should be proposed to overcome these drawbacks existing in the dual-rotor wind turbine design. In the present

study, an innovative dual-rotor wind turbine (a small rotor appended in front of the main rotor using a different shaft) was designed aiming to improve power production performance of an isolated turbine and overall wind farm efficiency.

There are two objectives in the newly designed DRWT: 1) to reduce the root losses incurred in the root region of the main rotor blades; and 2) to mitigate wake losses in wind farm settings through rapid mixing of turbine wake. Mixing rate of DRWT wake will be enhanced by a) increasing radial shear in wind velocity in wakes, and b) using dynamic interaction among the unsteady wake vortices shed from the primary and small rotor blades. The increased power capacity due to the smaller, auxiliary rotor blades can also be used to extract energy at wind speeds below the current cut-in speeds of conventional SRWT design.

The experimental study was carried out in a large-scale wind tunnel located at the Aerospace Engineering Department of Iowa State University. Scaled DRWTs with co- and counter-rotating configurations and SRWT models were placed in an atmospheric boundary layer wind under neutral stability conditions. In addition to measuring the dynamic wind loads acting on the turbine models, a set of high-resolution 2-D and Stereoscopic Particle Image Velocimetry (PIV) systems were also used in the present study to quantify the flow quantities behind the DRWTs model, in comparison with those behind the conventional a SRWT model. The power outputs of the isolated wind turbine models (i.e., DRWTs and SRWT) and a model turbine (SRWT) sited in the wake flow behind the DRWT models at different downstream locations were also compared quantitatively with those of the same model turbine sited in the wake behind the SRWT model. The detailed flow field measurements were correlated with the power output data and dynamic wind loading

measurements to elucidate underlying physics for higher total power yield and better durability of wind turbines.

5.2. Experimental Setup and Test Models

5.2.1. Atmospheric Boundary Layer (ABL) Wind-tunnel used in the present study

The present experimental investigations were performed in a large-scale Atmospheric Boundary Layer (*ABL*) wind-tunnel located at the Aerospace Engineering Department of Iowa State University. This closed-circuit wind-tunnel has a test section of 20 m long, 2.4 m wide and 2.3 m high, optically transparent side walls, and a capacity of generating a maximum wind speed of 45 m/s in the test section. Figure 1 illustrates the test section of the *ABL* wind-tunnel with a scaled *SRWT* model mounted in the center of floor. Chain arrays (with a spacing about 380mm) that are perpendicular to the flow direction were placed on the upstream floor of the wind turbine model in order to generate a typical atmospheric boundary layer wind profile and turbulence intensity corresponding to an open-water terrain. The wind-tunnel ceiling is flexible and is adjusted along the length to ensure the turbulent boundary layer growth of the simulated *ABL* wind under close to zero pressure gradient condition in the flow direction. The temperature of the airflow in the wind tunnel during the experiments was kept as constant by using a cooling system, hence, the incoming ABL wind approaching the wind turbine model would be under neutral stability conditions.

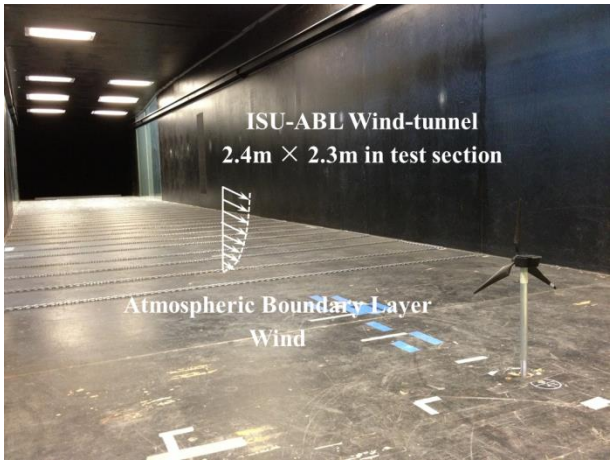

Fig. 1 Test section of the ABL wind-tunnel

It is suggested that the mean velocity profile of an atmospheric boundary layer flow over an open terrain condition can usually be fitted by using a power law (Jain, 2007). For the present study, the wind speed at any height can be expressed as a power law based on a reference height, i.e., $U(z)=U_H(z/H)^{\alpha}$, where U_H is the wind speed at hub height H. The value of the power law exponent 'α' is determined by the terrain roughness. Turbines in offshore wind farms (e.g., the Greater Gabbard in UK and Horns Rev II in Denmark) usually operate in an *ABL* profile of $\alpha\approx0.10$. An exponent of $\alpha\approx0.11$ for open water (e.g., for offshore wind farms) under neutral stability conditions was recommended by Hsu (Hsu et al, 1994), and this value was also recommended by ASCE standard to represent the ABL wind over offshore (open sea) terrain. Furthermore, offshore wind farms on the flat ocean surfaces have relatively lower turbulence level compared to the onshore case. Tong (2010) and GL (Germanischer Lloyd) regulations suggested a range from 0.08 to 0.12 for the turbulence intensity at hub height of offshore wind turbines. Figure 2 illustrates the measured *ABL* wind speed profiles, which were obtained by using a Cobra Probe Anemometry system (TFI series 100 of Turbulent Flow Instrumentation Pty Ltd) at the location where the wind turbine model was mounted. In the present study, the ceiling height in the test section was adjusted, so the

wind speed profile fit a curve with an exponent of α=0.11 and turbulence intensity of 9.9% at the wind turbine hub height. Here the turbulence intensity is defined by using the expression of $I_u = \sigma_u / \overline{U}_{local}$, where σ_u is the root-mean-square of the turbulent velocity fluctuation, and $\overline{U}_{local}$ is the time-averaged local velocity where Cobra probe located.

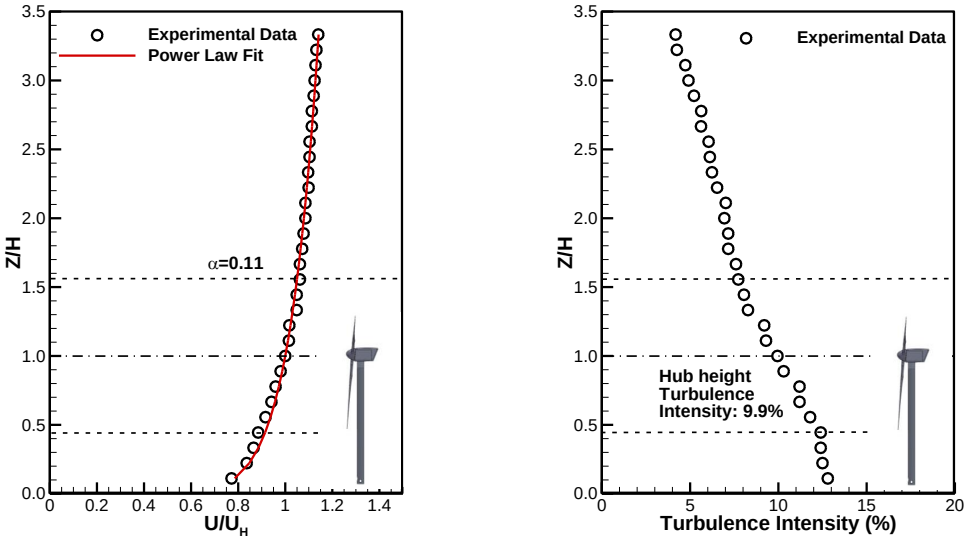

(b) Mean velocity profile (b) Turbulence intensity profile

Fig.2 The measured Atmospheric Boundary Layer wind profiles

5.2.2. Wind turbine models

In the present study, two wind turbine models were built for the comparative investigations. A SRWT was used as the baseline, which represents the most commonly used three-blade horizontal axis wind turbines (HAWT) seen in modern wind farms. The detailed descriptions about the design parameters for this *SRWT* can be found in the previous study (Tian et al, 2013). The model turbine has a rotor diameter of D = 280 mm and a hub height of H = 225 mm over the wind tunnel floor. The SRWT model (at a scale ratio of 1:350) was used to simulate a typical commercial HAWT mounted in the offshore wind farm with the rotor diameter around 90*m* and tower height about 80*m*. The rotor blades were produced of a hard plastic material by a fast prototyping machine. As shown in Fig. 3, a secondary rotor

with three small blades was appended in front of the main rotor (using by different shaft) for DRWT designs. The rotational directions of the upstream and downstream wind turbines (i.e., co-rotating and counter-rotating) in the DRWT models were also compared due to the flow performance in which configuration would be better still being unclear. It should be noted that the blockage ratio of the wind turbine models (i.e., the ratio of the turbine rotor swept area to the cross-section area of the *ABL* wind-tunnel test section) was found to be less than 2%, and thus the blockage effect of the wind turbine models in the test section is negligible for the present study.

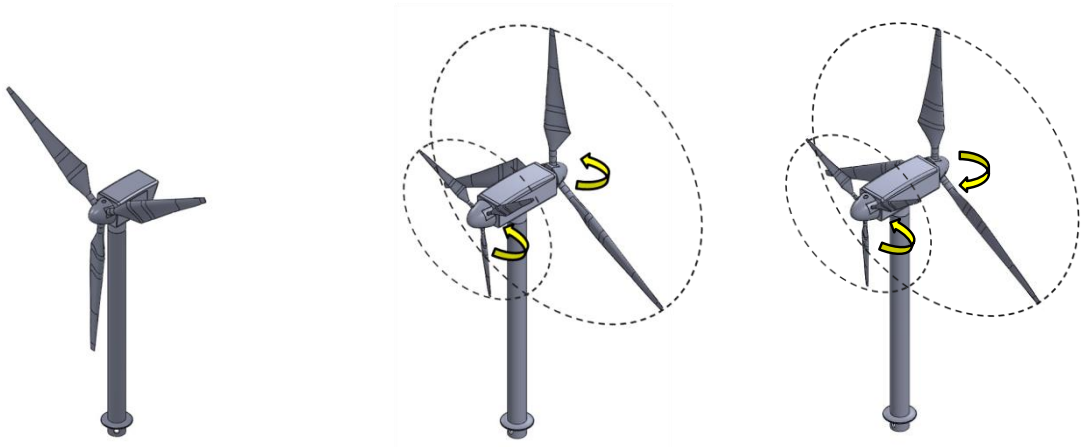

(b)SRWT (b) CO-DRWT (c) CN-DRWT

Fig.3 Schematic of the test models used in the present study

During the experiments, the mean velocity of the airflow at hub height was set to be around 6.5 m/s (i.e., $U_H \approx 6.5$m/s), corresponding to a Reynolds number of approximately 1.2×10^5 (i.e., $\mathrm{Re}_D \approx 1.2\times10^5$, based on the main rotor diameter and the wind speed at the hub height). It is significantly lower than the Reynolds number of the utility-scale wind turbines ($\mathrm{Re}_D > 1.0\times10^7$). According to Alfredsson et al. (1982), it may have a significant effect on the power generation performance of the wind turbines (i.e., the maximum power coefficient would be much lower for a small-scale model turbine operating at a lower Reynolds

number). However, according to a comprehensive investigation conducted by Chamorro et al (2011) recently, they found that the fundamental flow statistics (e.g., normalized profiles of mean velocity, turbulence intensity, kinetic shear stress) showed asymptotic behavior with Reynolds number in the wake. The Reynolds number of mean velocity to reach the independence condition is lower than those of higher statistics (i.e., turbulence intensity and kinetic shear stress). Reynolds number independence for mean velocity could be reached at $\mathrm{Re}_D \approx 4.8\times10^4$ and that of higher order statistics started at $\mathrm{Re}_D \approx 9.3\times10^4$. In the present study, the Reynolds number based on the rotor diameter (found to be around 1.2×10^5) lies above the required minimum Reynolds number as suggested by Chamorro to satisfy Reynolds number independence for wake flow characteristics. In addition, Whale et al (2000) observed similar wake statistics for a wide range of Reynolds number although the boundary layer over the blades and the shedding vorticity is known to be highly sensitive to Reynolds number. As suggested by Medici et al (2006), the behaviors of the unsteady vortex and turbulent flow structures in the wake of wind turbines would be independent of the Reynolds number when the Reynolds number of the wind turbine is high enough. The wind turbines with similar tip-speed-ratio (*TSR*) would generate similar near wake characteristics such as helical shape, rotation direction and strength decay of the tip vortices.

5.2.3. Dynamic wind loads acting on the turbine and power output measurements

In the present study, the wind turbine rotor and nacelle were supported by an aluminum rod which was also used as a turbine tower. A high-sensitive force-moment sensor (JR3 load cell, model 30E12A-I40) was mounted under the wind tunnel floor and used to hold the wind turbine models while measuring the dynamic wind loads (thrust forces and bending moments) acting on them. The JR3 load cell is capable of measuring the forces on three

orthogonal axes and the moments about each axis. The precision of this load cell for force measurements is ±0.25% of full range (40N). During the experiments, the dynamic wind load data was acquired for 120 seconds at a sampling rate of 1,000 Hz for each test case. A Monarch Instrument Tachometer was also used to measure the rotation speed of the wind turbine blades independently.

During the experiments, the incoming wind velocity was kept as constant, and the rotating speed of the rotors was adjusted by applying different electric loadings to the small DC generator installed inside the nacelle. The power outputs of the model turbines were achieved by measuring the voltage outputs from the small generators and the corresponding electrical loadings applied to the electric circuits. The voltage outputs of each DC generator were acquired through an A/D board plugged into a host computer at a data sampling rate of 1.0 kHz for 120 seconds. By applying different electric loads to the small electricity generators, the optimum tip-speed-ratio of a turbine model, i.e., at the tip-speed-ratio when the turbine model reaches the maximum power output, can be determined. The optimum tip-speed-ratio (TSR) of the wind turbine models used in the present study was found to be about 5.0 (i.e., $TSR \approx 5.0$). As described above, the power coefficients of the scaled wind turbine models would be much lower than those of the utility-scale wind turbines. Therefore, instead of using absolute values of the power coefficients, the normalized power outputs of the wind turbine models (i.e., normalized by the power output of the same turbine model operating in isolation) were used in the present study to assess the effectiveness of using the DRWT designs to reduce the root losses and wake losses for improving wind farm efficiency.

5.2.4. PIV and point-wise streamwise velocity measurements to quantify the wake characteristics behind the wind turbine models

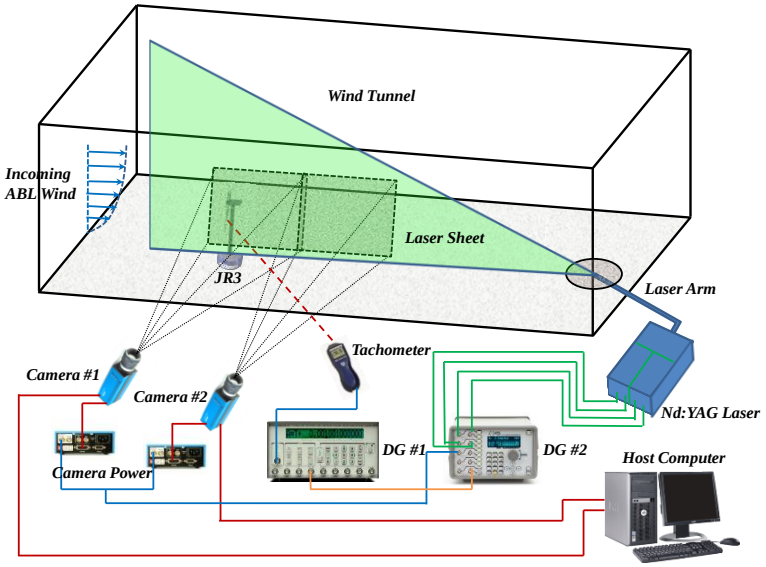

Fig.4

Fig.4 Experimental setup used for PIV measurements

In addition to the power outputs and dynamic wind loading measurements, a high-resolution PIV system was also used to acquire the flow fields to characterize the flow statistics in the turbine wakes. Figure 4 illustrates the schematic of the experimental setup for the PIV measurements, which was used to obtain detailed flow field measurements to quantify the turbulent flow structures behind the wake (X/D<2.5) of the wind turbine models. The airflow was seeded with ~1μm oil droplets which were generated using a fog machine (ROSCO 1900). Illumination was provided by a double-pulsed Nd:YAG laser (EverGreen 200) with a pulse energy of 200 mJ at the wavelength of 532nm. The laser beam was shaped to a sheet by a set of mirrors along with spherical and cylindrical lenses. The thickness of the laser sheet in the measurement region was about 1.0 mm. In order to obtain a larger measurement window along the streamwise direction to visualize the evolution of the unsteady wake vortex and turbulent flow structures behind the model turbines, two high

resolution 14 bit CCD cameras (PCO2000) with an overlapping length of 20mm in the streamwise direction were used for image acquisition with the axis of camera oriented perpendicular to the laser sheet simultaneously. The CCD camera and the double-pulsed Nd:YAG laser were connected to a host computer via digital delay generator (BNC565), which was used to control the timing of the laser illumination and image acquisition.

After image acquisition, the instantaneous PIV velocity vectors were calculated from the cross-correlation technique with a 32 × 32 pixels interrogation window. An effective overlap of 50% of the interrogation windows was employed in the PIV image processing. The vorticity ($\omega_z = \frac{\partial v}{\partial x} - \frac{\partial u}{\partial y}$) can be calculated from the instantaneous velocity vectors (u_i,v_i). The distributions of the ensemble-averaged flow statistics such as the normalized mean velocity, normalized Reynolds stress ($\tau = -\overline{u'v'}/U_H^2$) and turbulence kinetic energy ($TKE = 0.5(\overline{u'^2} + \overline{v'^2})/U_H^2$) were also calculated from the data after image processing. In the present study, a sequence of 1000 frames of instantaneous PIV image pairs were acquired in order to achieve a good convergence of flow quantities of the PIV measurements, especially for high-order turbulence statistics such as Reynolds stress and TKE. The measurement uncertainty level for the first-order flow quantity, such as velocity vector, is estimated to be within 2%, while the uncertainties levels for ensemble-averaged high-order flow statistics, such as Reynolds stress distributions, are to be about 5%.

Both “free-run” and “phase-locked” PIV measurements were performed during the experiments. The “free-run” PIV measurements were conducted in order to determine the time-averaged flow quantities (e.g., mean velocity, Reynolds stress, TKE) in the wake flow. For the “free-run” experiments, the image acquisition rate was selected at a fixed frequency which would avoid matching the harmonic frequency of the rotating blades in order to obtain

as much blade phase positions as possible to ensure the ensemble-averaged flow statistics. The "phase-locked" PIV measurements were performed to elucidate more details about the evolution of unsteady wake structures such as vortices related to the phase position of the rotating blades. For the "phase-locked" measurements, a digital tachometer (Monarch PLT 200) and an additional timing delay generator (Stanford DG535) were used to detect the phase position of a pre-marked rotor blade to achieve the "phase-locked" PIV measurements. At each selected phase angle, 400 frames of image pairs were acquired to calculate the phase-averaged flow quantities (i.e., velocity and vorticity) distributions in the wake flow.

A Cobra probe Anemometry system was mounted on an accurate motorized traverse system, which was also used to measure all three components of instantaneous and time-averaged flow velocity at the locations of interest to supplement the PIV results, especially at far wake region (i.e., at the downstream locations of X/D=2, 4, 6 and 8). Other flow quantities such as the turbulence intensity and Reynolds stresses can also be derived based on the instantaneous measured data. At each measurement point, data was acquired for 60 seconds at a sampling rate of 2.5 KHz.

5.3. Results and Discussions

5.3.1. Dynamic wind loads acting on the wind turbine models

Recently, the effects of the unsteady turbulence flow and associated dynamic wind loads are being paid more and more attention for optimal design of modern wind turbines (Hu et al., 2012). In the present study, the wind loading measurements were conducted on the SRWT and DRWTs models when they are operating at their optimum tip-speed-ratio (i.e., TSR ≈ 5.0) and the power outputs reaching their peak values in the same incoming airflow. The JR3 force-moment sensor was used to obtain time-resolved measurements of all three

force components and moments about each axis at a sampling rate of 1 KHz. The thrust coefficient (C_T) and the bending moment coefficient (C_M) corresponding to the wind turbine models, are defined as

$$C_T = T / (0.5\rho U_H^2 \pi R^2) \quad (1)$$

and

$$C_M = M / (0.5\rho U_H^2 \pi R^2 H) \quad (2)$$

where T is the thrust force acting on the wind turbine model, M is the bending moment, ρ is the air density, U_H is the mean flow velocity at hub height H and R is the radius of the main turbine rotor. Figure 5 shows the dynamic wind load measurement results in terms of the instantaneous (i.e., solid lines) and time-averaged (dashed lines) thrust coefficients of the SRWT and DRWTs models. As shown in the plot, the instantaneous aerodynamic loads acting on the wind turbine models are highly fluctuated as a function of time. It is found that the dynamic wind loads (both of the mean values and the fluctuation amplitudes) acting on the DRWTs are considerably higher than those on the SRWT model in the same incoming airflow, due to the small rotor appended on the DRWT models.

According to the time-series dynamic load measurements shown in Fig.5 and the mean loads and standard deviation values on the wind turbine models illustrated in Table 1, the loading characteristics of the SRWT and DRWT models can be quantified. As described above, since DRWTs have co-rotating and counter-rotating configurations, both of them are compared with the SRWT system, aiming to find which one would be a better configuration for the DRWT designs. It can be seen that, due to the additional rotor installed in front of the main rotor for the DRWT models, the mean dynamic wind loading (both of the mean thrust coefficient and bending moment coefficient) on CO-DRWT and CN-DRWT models are

found to increase to 13% and 3.5% respectively, in comparison to those of the SRWT system. While the standard deviation amplitude of the dynamic wind loads acting on the CO-DRWT model were observed to be much (i.e., ~67% augment in the thrust force and 82% increase in the bending moment) higher than those of the SRWT model. However, the loads acting on the CN-DRWT model demonstrate another trend with the CO-DRWT design, which only have a 15% increase in thrust force and 24% boost for bending moment are observed in CN-DRWT model, in comparison to the SRWT system.

According to the suggestions by Adaramola et al. (2011) and Hu et al. (2012), the aerodynamic thrust force acting on a wind turbine is proportional to the momentum deficits in the square of the airflow velocity across the rotation disk of the wind turbine, and the power output of the wind turbine would be proportional to the deficits in the cube of the flow velocity across the rotation disk. As a result, higher mean thrust forces acting on the DRWT models (i.e., C_T=0.392 and 0.358 for CO-DRWT and CN-DRWT models, respectively, compared to C_T=0.346 for the SRWT system) are supposed to harvest more energy from the wind. However, a different scenario is found in DRWT systems, and we will discuss with the power output measurements in detail later.

The standard deviation of the dynamic wind loads can be used to quantitatively evaluate the fatigue loads acting on a wind turbine, the higher fluctuations of the wind loads on the DRWT models would indicate more severe fatigue loading compared to those of the SRWT model. It is believed to be closely related to the more complicated turbulent structures in the wake behind the DRWT models induced by the additional rotor, and which will be revealed clearly and qualitatively in the PIV measurements in the following section.

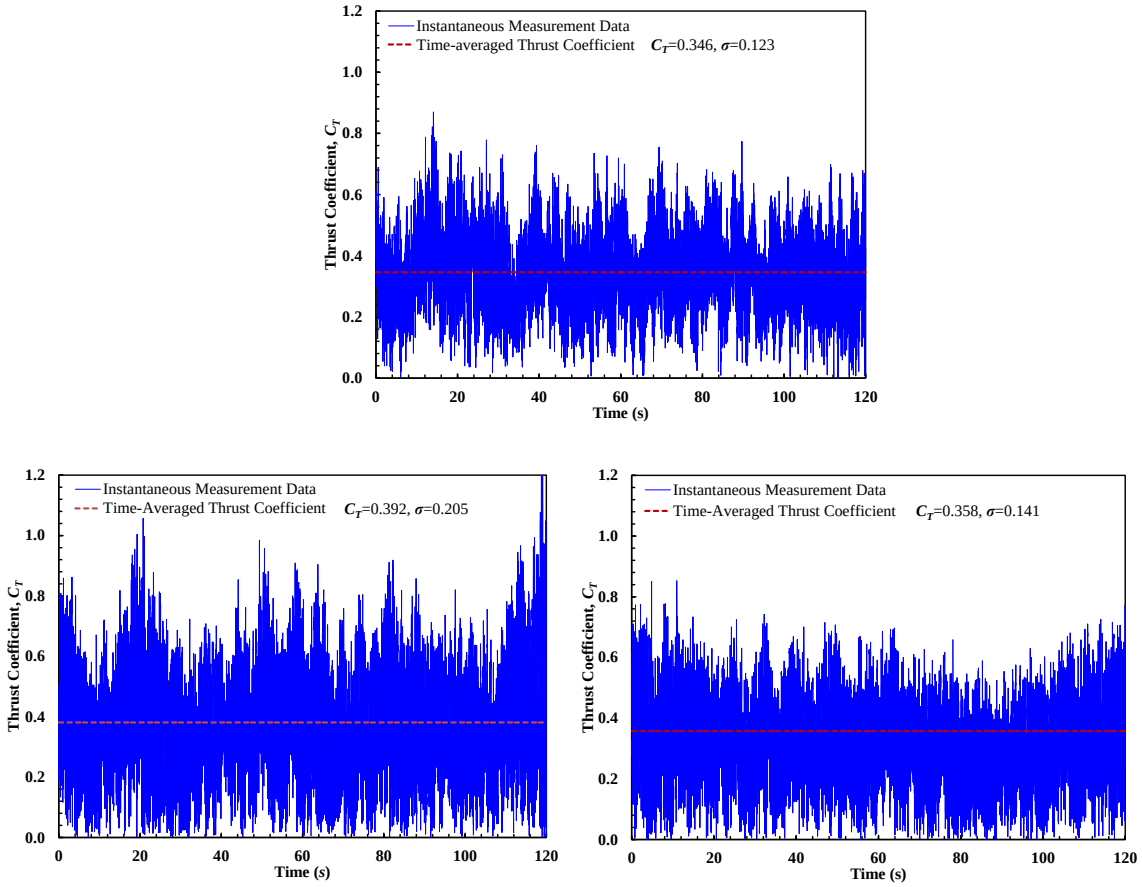

Fig.5 Time history of the instantaneous thrust coefficient for SRWT (upper), CO-DRWT (down left) and CN-DRWT (down right)

Table.1 The wind loads acting on the turbines in SRWT and DRWT models

	SRWT	CO-DRWT	CN-DRWT
Mean thrust coefficient, C_T	0.346	0.392	0.358
The standard deviation of the thrust coefficient, σ_{CT}	0.123	0.205	0.141
Mean bending moment coefficient, C_M	0.411	0.455	0.416
The standard deviation of the bending moment coefficient, σ_{CM}	0.133	0.242	0.165

5.3.2. 2-D PIV measurement results

Based on an image sequence of around 1,000 frames of instantaneous PIV measurements, the ensemble-averaged flow statistics such as the mean velocity and in-plane TKE in the wind turbine wakes can be achieved. Figure 6 shows the ensemble-averaged streamwise velocity distributions in the wake flows behind the SRWT and DRWT models. As shown in Fig. 6, a proportion of the kinetic energy from the incoming airflow is harvested by the model turbines and the oncoming airflow is found to decelerate greatly as it passes through the rotation disks of the rotor blades. A region with relatively high velocity exists in the near wake of the SRWT system right above the turbine nacelle and near the roots of the turbine blades (i.e., $Z/D<0.2$), which extends up to $X/D=0.6$ downstream (Shown in Fig. 6a). While similar relatively high velocity regions are also found to occur in the turbulent wake of DRWT models (shown in both CO-DRWT and CN-DRWT systems), the regions are significantly smaller (i.e., $X/D<0.1$) and extend longer (i.e., $X/D\approx1.0$) compared to those of the SRWT model. It is believed that the poor design in aerodynamics near the roots of the main rotor blades would result in a "dead zone", where very little wind energy is harnessed by the wind turbine. As a portion of wind energy from the same incoming airflow can be harvested by the small rotor installed in front of the main rotor for DRWT cases, the "dead zone" region is decreased in contrast with the SRWT system (i.e., reducing the root losses). It can be seen clearly that the incoming airflow within the small rotation disk is decelerated significantly as it passes through the front rotor in DRWT systems, but the induced wake from the small rotor has little effects on the aerodynamic performance of the main rotor.

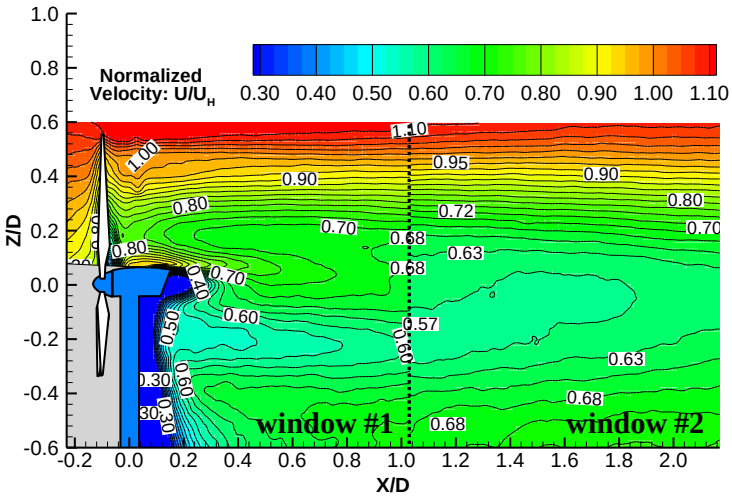

(a) The velocity distributions behind the SRWT model

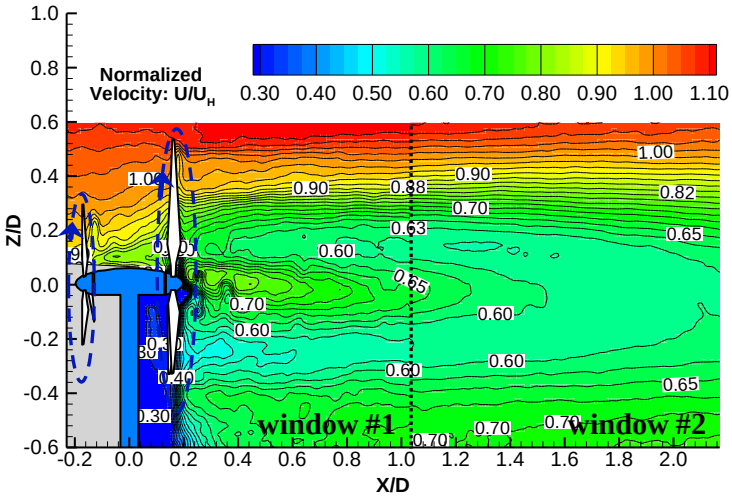

(b) The velocity distributions behind the CO-DRWT model

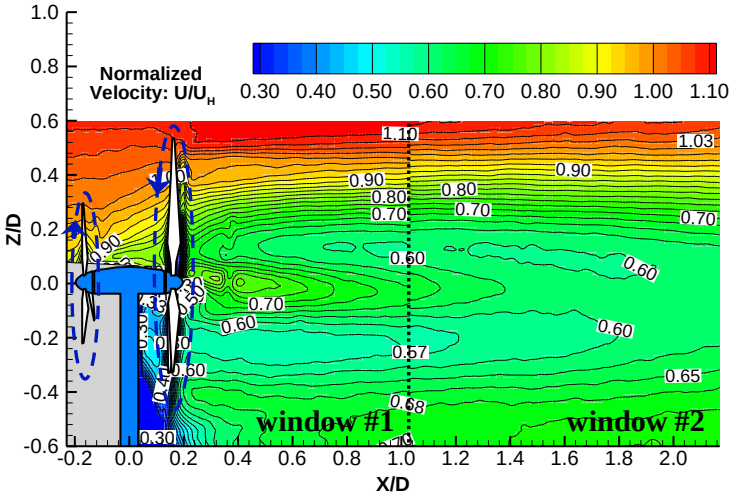

(c) The velocity distributions behind the CN-DRWT model

Fig. 6 Ensemble-averaged streamwise velocity distributions in the turbine wakes

In order to provide a quantitative comparison for the velocity deficit in the wakes of the wind turbine models, the transverse velocity profiles were extracted from the ensemble-averaged PIV measurement results at the downstream locations of X/D=0.5, 1.0 and 2.0, respectively. As shown in Fig. 7, significant velocity deficits are found to be generated in the turbulent wakes behind the wind turbine models, compared to the velocity of the oncoming airflow. Due to the existence of the secondary small rotor in front of the main rotor in the DRWT designs, the velocity deficits in the wakes behind the DRWT model are observed to be slightly larger than those of the SRWT case, which indicates the wind energy from the incoming airflow is also harvested by the additional rotor. As described in Hu et al. (2012), larger velocity deficits in the near wake behind a wind turbine would indicate a stronger thrust force acting on the wind turbine. As greater velocity deficits are observed in the wakes behind the DRWT models, higher thrust force would also be generated on the DRWT systems, which confirm with the results of the dynamic wind loading measurements as shown in Fig. 5 and Table. 1.

Based on the measurement results given in Fig. 7(a), very little changes can be observed among the transverse velocity profiles extracted at different downstream locations when Z/D>0.2 in the wake of SRWT design. However, the velocity profiles in the corresponding region in the wakes of the DRWT systems are observed to be decelerated gradually when the airflows move to the downstream locations. As the main rotor is installed behind the nacelle and tower in the DRWT designs, the peak value in relatively high velocity region over the turbine nacelle is found to be slightly higher than that of the SRWT case at the location of X/D=0.5, but the velocity profiles would recover faster to in comparison to those of the SRWT design. The faster recovery of the velocity deficits in the far wake behind

the DRWT designs is believed to be closely related to the generation of more complex wake vortex structures and enhanced turbulent mixing of the turbine wake flow due to the existence of the additional rotor installed in front of the main rotor blades, which can be revealed clearly from the streamwise velocity profiles extracted from the PIV results at the centerline location (i.e., Z/D=0) behind the wind turbine models.

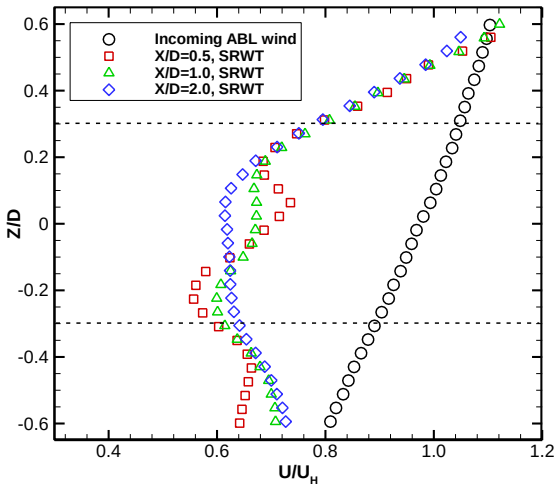

(a) The wake behind SRWT model

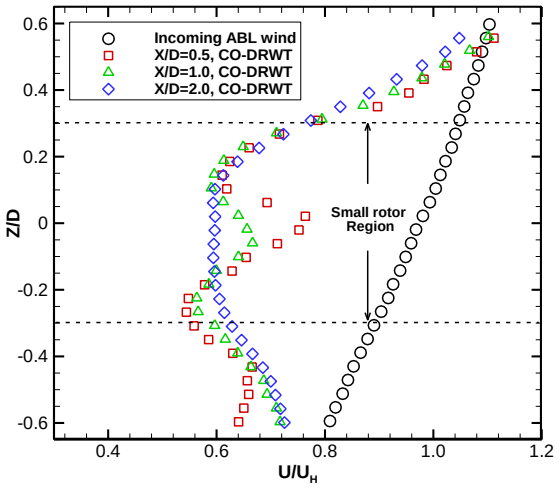

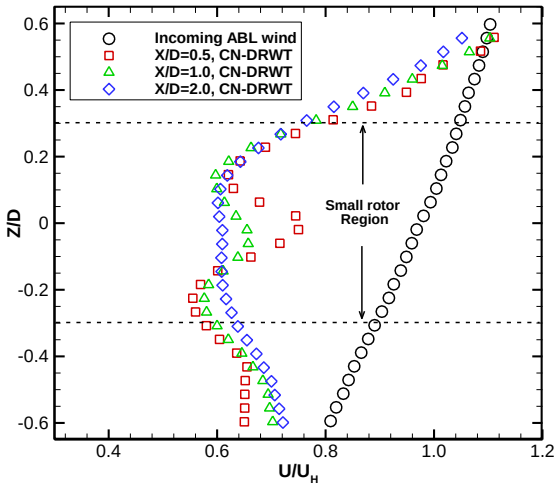

(b) the wake behind CO-DRWT model (c) the wake behind CN-DRWT model

Fig.7 Transverse velocity profiles in the wake flows behind the wind turbine models

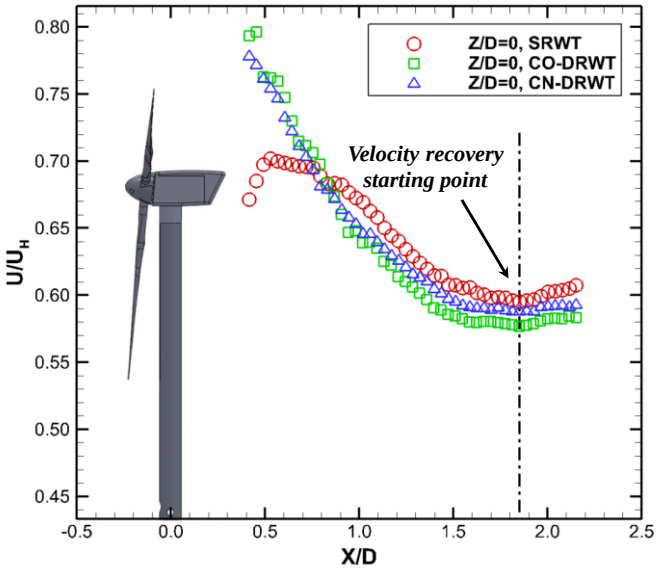

Fig.8 Streamwise velocity distributions at the centerline in the wakes behind the SRWT and DRWT models

Figure 8 illustrates the streamwise velocity profiles extracted from the PIV measurements at the centerline location in the wakes behind the wind turbine models. It can be seen that the streamwise velocity would decrease gradually from near wake (e.g., *X/D*=0.5) to far wake region (e.g., *X/D*=1.8) due to the influence induced by the turbulent wake mixing. The streamwise velocity in the near wake region (e.g., *X/D*=0.5) of DRWT models is higher than that of SRWT model. While the re-energizing process would start at the same location of $X/D \approx 1.85$ (the dash-dotted line in represents the location where the airflow velocity start to recover) for all of the wind turbine models. Taking into account that the rotor in SRWT system is installed in front of the nacelle whereas the main rotor in DRWTs is located behind the turbine nacelle and tower, thus, the distance for the recovery of the velocity deficits behind the DRWT designs is much shorter than that of SRWT case. The streamwise velocity of the airflow in the wake of CN-DRWT model is slightly higher than that of the CO-DRWT system, which would indicate a better ability for velocity recovery in the counter-rotating design.

Figure 9 demonstrates the in-plane normalized turbulent kinetic energy (i.e., $TKE = 0.5(\overline{u'^2} + \overline{v'^2})/U_H^2$) distributions in the wake flows, which provides further insights to explain the distinctions in the velocity deficit recovery behind the compared wind turbine models. As suggested by Lignarolo et al. (2014) and Tian et al. (2014), the evolution of the unsteady wake vortices (i.e., the generation, breakdown and dissipation processes) would play an important role on the TKE production in a turbine wake. It can be seen clearly that, the regions with relatively high TKE levels are found in the wake right behind the turbine nacelle and towers. This is believed to be closely related to the formation and shedding of unsteady wake vortices from the turbine nacelles and towers, which are visualized more clearly from the "phase-locked" PIV measurement results and will be discussed later. The TKE levels are also found to be quite high at the upper regions behind the rotation disks of the turbine blades, which is correlates with the shedding paths of the unsteady vortices from the tips of the rotating rotor blades in the wake flows.

As shown in Figure 9, even though the main rotor is installed in the downstream side of the tower in DRWT designs, the regions with relatively high TKE levels behind the tower would extend shorter than that of the SRWT design (i.e., up to X/D ≈ 0.4 in DRWT cases versus X/D ≈ 0.5 in SRWT case). This is due to the periodic turbulent motions induced by the downstream rotor blades can break up the vortices shedding from the turbine tower and enhance the turbulent mixing in the wake region. The relatively high TKE levels are also found to be concentrated along the shedding paths of the unsteady tip vortices, and the TKE values would increase gradually with the increasing distance in the downstream wake. It can be seen clearly that the TKE values in the shedding path of the tip vortices in the far wake (i.e., X/D>1.0) behind the CO-DRWT system would be higher than those of the other two

models, while the TKE in the far wakes of the SRWT and the CN-DRWT cases show a similar level to each other. As described in Tian et al. (2014), the TKE level can usually be used as a parameter to indicate the extent of turbulent mixing in a turbulent flow. The higher TKE levels existing in the far wake behind the CN-DRWT case would indicate more intensive mixing in the wake flow, resulting in a faster recovery of the velocity deficits in the downstream region. This finding will be verified by the power measurements in the following session.

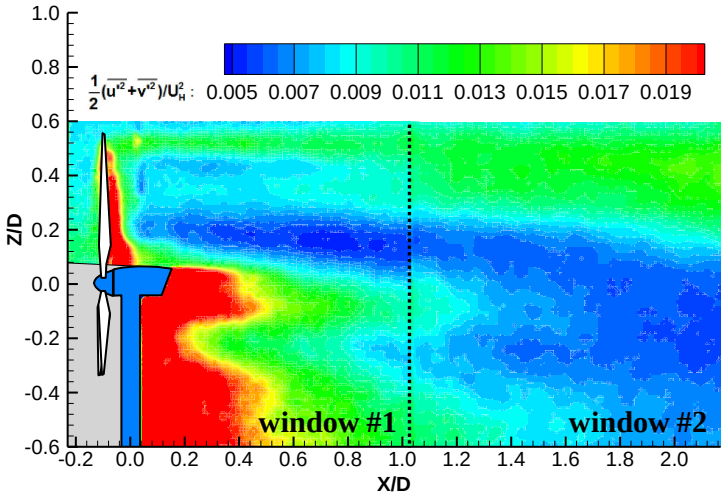

(a) Normalized TKE distribution behind the SRWT model

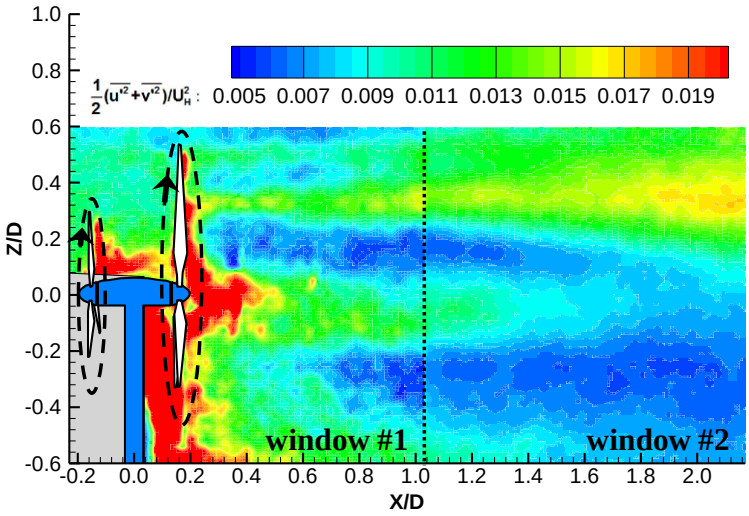

(b) Normalized TKE distribution behind the CO-DRWT model

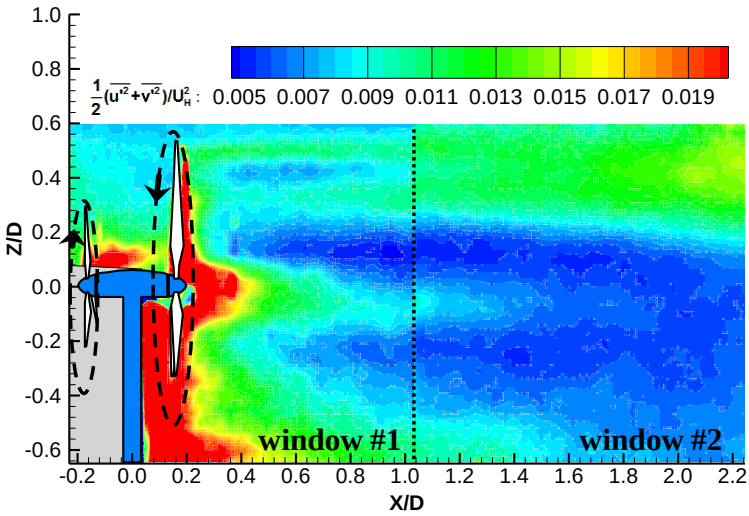

(c) Normalized TKE distribution behind the CN-DRWT model

Fig. 9 Normalized TKE distributions in the wake flow behind the SRWT and DRWT models

As described above, the "phase-locked" PIV measurements were also performed in the present investigation to visualize the "frozen" image of unsteady vortex structures in the wakes at various rotation phase angles of the rotor blades. It should be noted that, the phase angle was defined as the angle between the position of a pre-marked main rotor blade and the vertical PIV measurement plane. The initial position of the pre-marked rotor blade for the PIV measurement (i.e., phase angle of $\theta = 0.0°$) was located within the vertical PIV measurement plane, where the pre-marked blade would be at the most upward position. The pre-marked turbine blade would rotate out of the vertical PIV measurement plane as the phase angle increasing. Figure 10 illustrates the "phase-locked" measurements in terms of the vorticity distributions in the wake flows for the SRWT and DRWT models at the phase angles of $\theta = 0.0°$, 30.0°, 60.0°, and 90.0°, respectively. Various unsteady vortex structures with different sizes and orientations are observed in the wake flows behind the wind turbine models.

As shown clearly in the case of SRWT model (Fig.10a), a tip vortex was generated in the wake from the tip of the pre-marked rotor blade at the phase angle of angle of θ =0.0°. The tip vortex was found to shed from the rotor blade tip position when the pre-marked blade was rotating out of the vertical PIV measurement plane and align itself nicely with other tip vortices induced by the other two rotor blades to constitute a moving tip vortex array in the turbulent wake flow. Apart from the tip vortices, an additional array of concentrated vortex structures is also observed to be produced in the wake flow at approximately 60% ~ 70% span of the rotor blades. The vortex structures are found to move outward with the expansion of the wake flow, and merge with the tip vortices in the near wake and then dissipate eventually at far wake region. Similar vortex structures at the position of approximately 60% ~ 70% span of the rotor blades were also observed in the experimental investigations of Whale et al. (2000), Hu et al. (2012) and Tian et al. (2014) to study the evolution of the unsteady vortex structures in the wake flows. Except for the tip vortices and the vortex structures shedding from the rotor blade periodically, a series of unsteady vortices are also generated and shed periodically from the root sections of the turbine blade. The unsteady vortices produced from the turbine nacelle as well as the unsteady von-Karman vortex streets generated from the turbine tower, can be found obviously in the phase-locked PIV measurements. As suggested by Tian et al. (2014), the flow characteristics in the turbulent wake were found to be dominated by the evolution (i.e., formation, shedding, breakdown and dissipation) of the unsteady wake vortices.

Figures 10 (b) and (c) depict similar complex vortex structures in the wake flows behind the DRWT systems compared with those of the SRWT case (i.e., periodic tip and root vortices as well as the concentrated vortices at approximately 60% ~ 70% span shedding

from the rotor blades, and the unsteady vortex structures shedding from the turbine nacelle and tower), but some obvious distinctions still can be identified from the comparisons in the downstream wakes. As the main rotor was switched from the front side of the tower to the rear side and a secondary small rotor was added in front of the main rotor, the vortex structures in the wake flows behind the small rotor rotation disk were considerably affected by the configurations in DRWT designs. The vortices from the blades of the secondary rotor are found to merge with the unsteady vortex structures at approximately 60% ~ 70% span of main rotor blades, which would result in two different phenomena due to different rotational directions. The strength of the unsteady vortex structures behind the CO-DRWT model is observed to be increased significantly, in comparison to those vortex structures in the SRWT case. This set of vortex structures would become parallel to the tip vortices array and then breakdown even further than the tip vortices in the downstream location. However, as shown in the Fig 10(c), the turbulent structures induced from the frontal rotor blades would combine with the vortex structures at 60% ~ 70% span of the main rotor blades, and then breakdown rapidly in the near wake (i.e., vortices breakdown at X/D ≈ 0.8 for the CN-DRWT case, while at X/D ≈ 1.0 for the CO-DRWT case) of the CN-DRWT model. The unsteady vortices shedding from the root sections of the main blade in the wake flow of CO-DRWT system is found to be elongated in the spanwise direction, in comparison to the orbicular-shape root vortices behind the SRWT model. While the concentrated unsteady root vortices are observed to tilt toward upstream direction in the wake flow of CN-DRWT case. Both of the vortices shedding from root sections of the main blades in the wake flows of the CO-DRWT and CN-DRWT systems would extend longer and breakdown further downstream compared to those of the SRWT case (i.e., X/D ≈ 1.8 in DRWT cases versus X/D ≈ 1.2 in SRWT case),

which are found to be agreed well with the earlier appearance of the regions with relatively high TKE levels in the wake regions behind the DRWT models as shown in Fig.9.

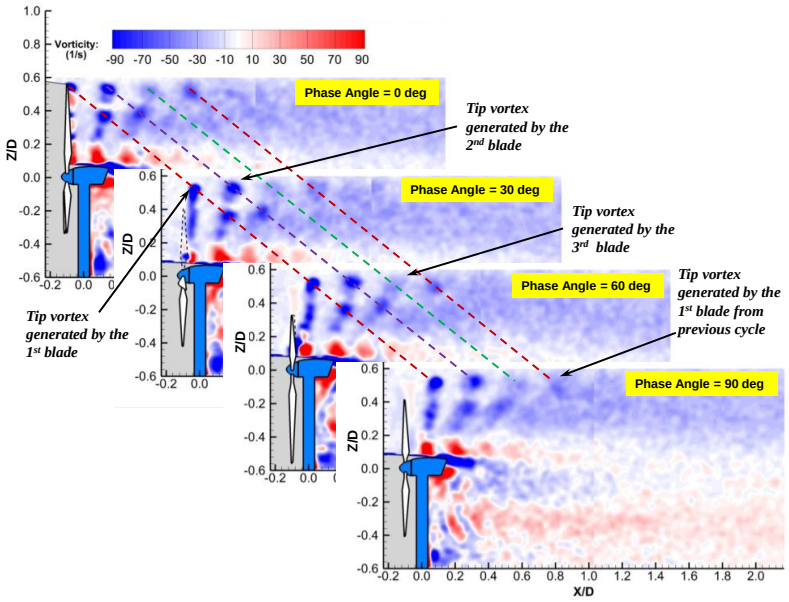

(a) Vorticity distribution in the wake behind the SRWT model

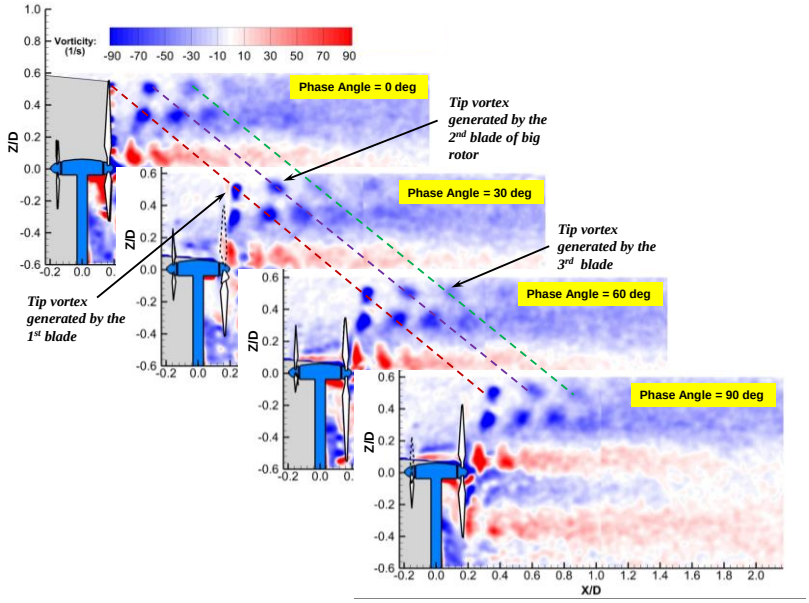

(b) Vorticity distribution in the wake behind the CO-DRWT model

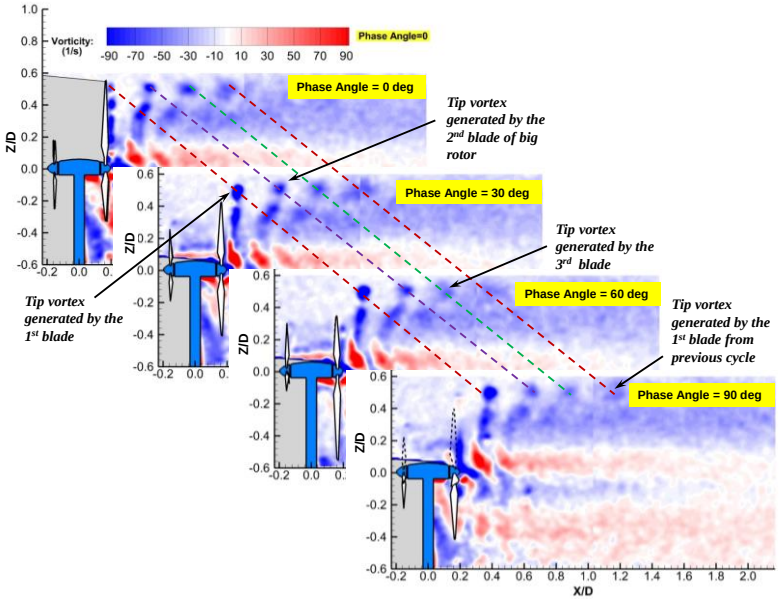

(c) Vorticity distribution in the wake behind the CN-DRWT model

Fig.10 Phase-locked PIV measurements in the wakes behind the wind turbine models

5.3.3. Point-wise flow statistics in the far wakes behind the SRWT and DRWT models

In the present study, Cobra Probe Anemometry was also utilized to attain the point-wise flow statistics in the far wake (i.e., at the downstream location of X/D ≥ 2.0) behind the wind turbine models to supplement the results achieved by PIV measurements. Figures 11 and 12 illustrate the measured transverse profiles of the time-averaged streamwise velocity and turbulent intensity in the far wake of the wind turbine models at the downstream positions of X/D=2.0, 4.0, 6.0 and 8.0, respectively. The streamwise velocity and turbulence intensity profiles of the free stream, which indicates no wind turbine installed at the upstream location, were also provided in the plots for comparison. It can be easily found that the upper wake boundaries, marked by dashed lines, can be identified from the plots, and the turbulent wakes would expand monotonically as the downstream distance increases.

Due to the secondary small rotor appended in front of the main rotor, the DRWT designs are able to harvest more wind energy form the same incoming airflow by reducing the root

losses of the rotor blades. It can be seen from Fig. 11(a) that, the streamwise velocities in the downstream regions behind the turbine nacelles and root sections of main blades in the DRWT cases are lower than that of the SRWT model. As shown in the results obtained by PIV measurements from Figs. 6, 7 and 8, the incoming airflow would be decelerated more in the wake flows in the DRWT cases and the velocity deficits are also found to have a good agreement with the measurement results by Cobra Probe Anemometry given in Fig. 11(a) at the downstream location of X/D = 2.0. This would indicate more wind energy from the incoming flow is harnessed by the secondary small rotor in front of the main rotor. The measured turbulent intensity profiles listed in Fig. 12(a) reveal that the turbulence intensity levels in the region behind the rotation disk of the CN-DRWT model are considerably higher than those of the CO-DRWT and SRWT cases, which would be consistent with the TKE results shown in Fig. 9. The turbulence intensity levels in the wakes are believed to be closely related to the generation and shedding of various unsteady vortex structures in the downstream wakes as visualized apparently in Fig. 10. As suggested by Cal et al. (2010), Calaf et al. (2010) and Wu et al. (2012), the higher turbulence intensity levels in the wake would indicate more intensive turbulent mixing in the wake flows to provide a faster vertical transport process of kinetic energy from the high-momentum airflow above the rotation disk to re-charge the wake flows, which would result in a faster velocity deficit recovery rate at the downstream location of X/D=2.0 behind the DRWT models.

As lower streamwise velocities but higher turbulence intensity levels at the location of X/D = 2.0 in the wakes of the DRWT systems, the higher velocity deficits recovery rate in the downstream location of X/D > 2.0 can be concluded according to previous results. Figures 11(b) and 12(b) illustrate the streamwise velocity distributions and turbulence

intensity levels in the wake of the wind turbine models. The streamwise velocities in the DRWT cases are found to be much higher than that of the SRWT case at the downstream location at X/D = 4.0 due to higher turbulence intensity levels and turbulent mixing in upstream airflows, which would imply more kinetic energy is available for downstream wind turbines sited in the wake of the DRWT models. However, the turbulence intensity is observed to be much smaller in the wake of the DRWT systems in comparison to that of the SRWT case at the downstream location of X/D = 4.0, which may indicate lower velocity deficit recovery rate in the far wakes (X/D > 4.0) of the DRWT systems compared to that in the SRWT case.

As shown in Fig. 11(c), the streamwise velocity in the wake of SRWT model at the downstream location of X/D=6.0 is recovered to a similar level with those in the DRWT cases. This result would confirm the findings derived from Figs. 11(b) and 12(c), where the turbulence intensity levels in the wake behind the SRWT model are higher than those in DRWT cases at the downstream location of X/D = 4.0. While the turbulence intensity levels in the wakes between the DRWT cases and SRWT case are found to be lower at the downstream position of X/D = 4.0 compared with those at the upstream locations, which would imply the velocity deficit differences, namely, the influence bringing by the wind turbine configurations behind these three wind turbine models at the further downstream region of X/D > 6.0 could become smaller gradually as the distance increases.

Figures 11(d) and 12(d) illustrate the velocity and turbulence intensity profiles increase at the downstream distance of X/D = 8.0, quite small velocity difference can be found to exist in the wake flows behind all of the three wind turbine models but significant velocity deficits still can be observed clearly compared to the velocity profile in free-stream. It indicates that

the flow velocity in the turbulent wake has not fully recovered in comparison with the incoming airflow, but the real wind turbine configurations can be neglected due to the velocity profiles observed at the far wake region of X/D = 8.0. The turbulence intensity levels can also be found to be within the same level in the far wake location as shown in Fig. 12(d), which implies that the benefits of the DRWT designs with a secondary small rotor to increase the wake interferences between the rotors to enhance turbulent mixing for a faster recovery of the velocity deficits in the wake flows would die away gradually in the further downstream region of X/D > 8.0.

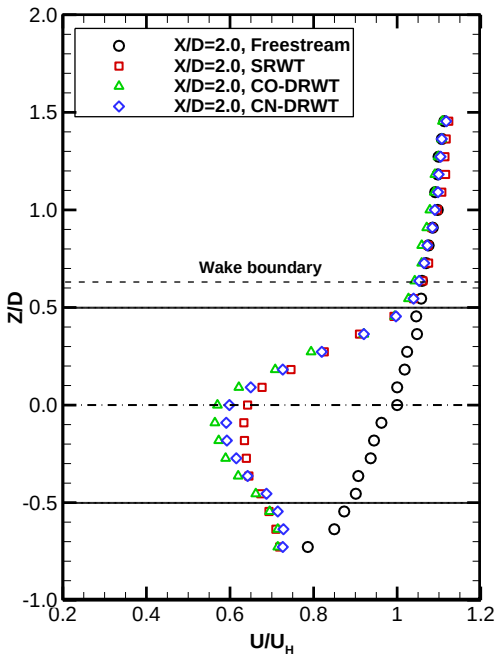

(a) X/D=2.0

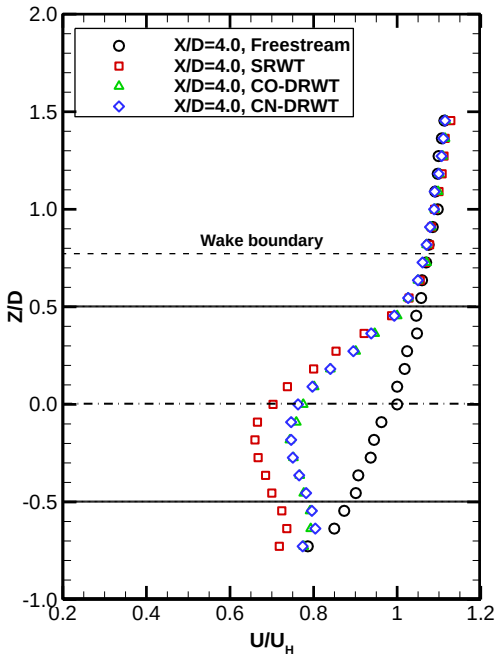

(b) X/D=4.0

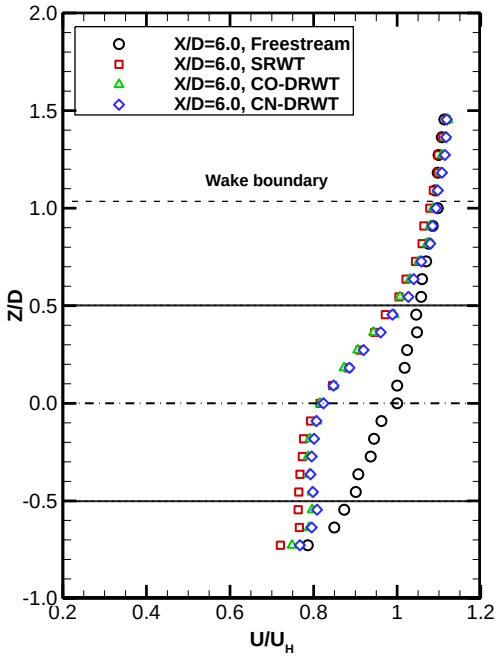

(c) X/D=6.0

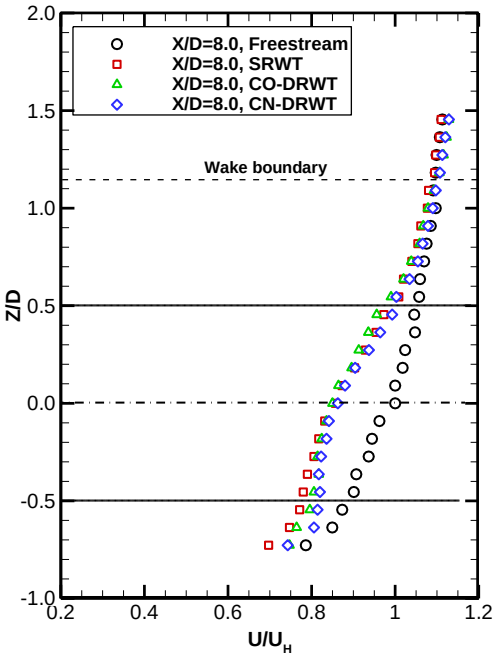

(d) X/D=8.0

Figure.11 Transverse velocity distributions in the far wake flows behind the wind turbine models

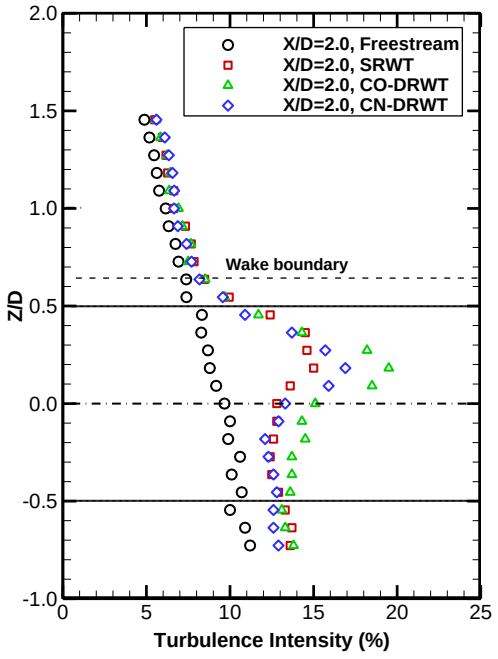

(a) X/D=2.0

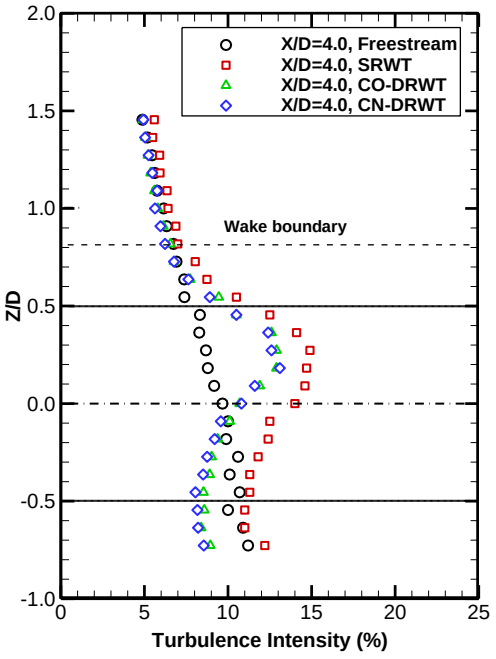

(b) X/D=4.0

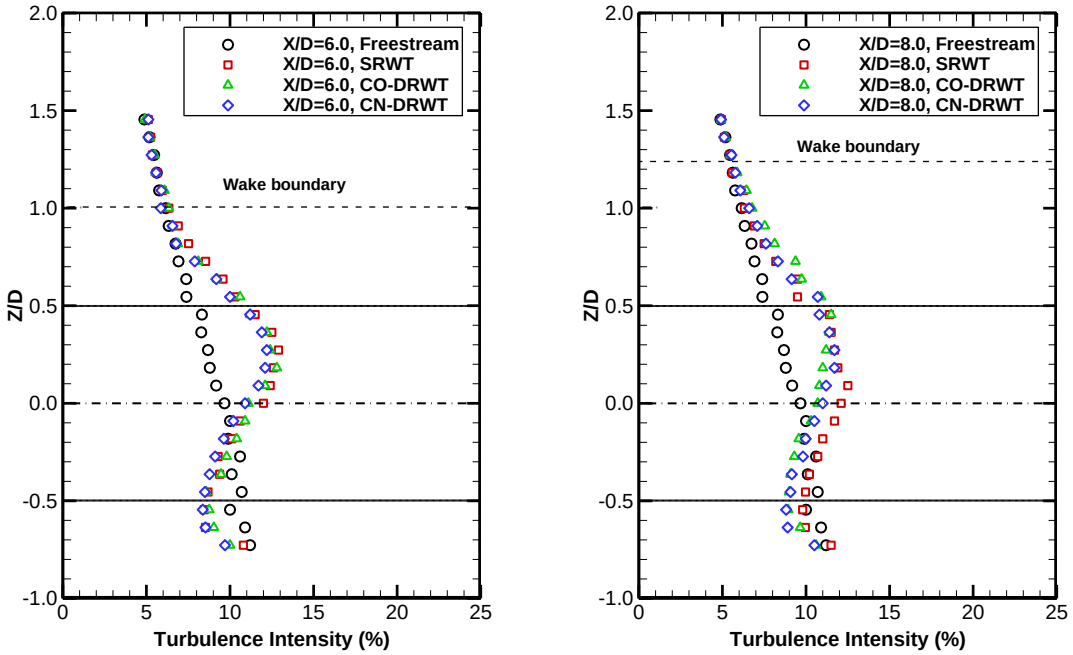

(c) X/D=6.0 (d) X/D=8.0

Figure.12 Transverse profiles of the turbulent intensity in the far wakes behind the wind turbine models

5.3.4. Power outputs in the wakes behind the SRWT and DRWT models

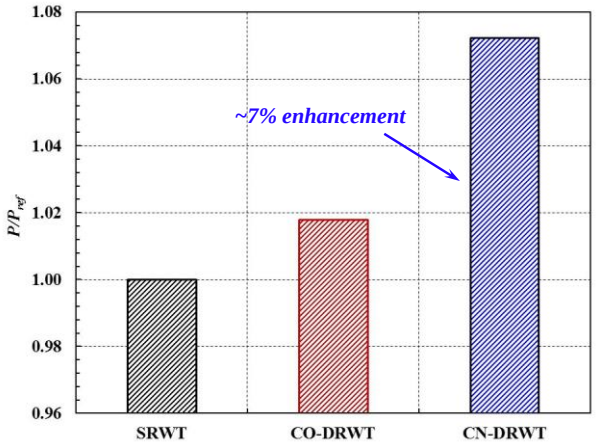

Figure 13. Normalized power output comparisons for the SRWT and DRWT models operating in isolated conditions

In the present study, the motivation of proposing the DRWT designs is to improve wind turbine performance and wind farm efficiency by reducing the root losses and mitigating

wake losses. As a result, a series of power output measurements were also conducted to assess the ability to harvest wind energy from the innovative DRWT designs compared to the conventional SRWT model. Instead of using the absolute power outputs, a normalized power output coefficient was utilized in the present study based on the measured power output for an traditional SRWT operating in isolated condition. The power output calculated in the present study was used by the expression of $P = V^2 / R_L$, where V is the voltage measured on the applied resistance, and R_L is the applied resistance in the circuit. The power coefficient was calculated by the expression of $C_P = P\eta / (0.5\rho U_H^3 A)$, where A is the area of blade rotation disk, η is DC motor efficiency. The optimum mechanical power coefficient for the test wind turbine models can reach up to around 0.2. Figure 13 gives the measured power output coefficients of the wind turbine models operating in the isolated conditions, which are normalized based on the power output from the SRWT model. It should be noted that, since the small rotors in the DRWT designs can also be used for harvesting the wind energy from the incoming airflows in addition to the main rotor, the power outputs from the DRWT systems were the sum of the power harnessed by the small and main rotors. As described above, the additional small rotor appended in front of the main rotor was designed to reduce the root losses by harnessing the wind energy existing near to the root sections of the rotor, the power outputs from the DRWT designs are found to be increased to some extent with the same incoming airflows compared with that in SRWT model. Specifically, the power outputs from the CO-DRWT and CN-DRWT designs are about 2% and 7% higher than the conventional SRWT model when they operate in isolated conditions, which indicate a higher wind energy conversion efficiency by the DRWT designs in contrast to the SRWT model. This result would be consistent with the velocity deficits obtained by PIV measurements

shown in Fig. 6, where more significant velocity deficits is found in the wake flows of the DRWT models. However, it shows a contrary phenomenon when compared with the dynamic wind loads illustrated in Fig. 5 and Table.1, where the wind loadings (i.e., thrust force coefficient and bending moment) for CO-DRWT case are about 9.5% higher than that in CN-DRWT system. It may imply that the unsteady flow structures (e.g., tangential velocity) induced by the frontal small rotor can enhance the flow performance of the main rotor in CN-DRWT system but deteriorate the flow conditions in CO-DRWT design.

In order to examine the wake losses in the downstream flows of the wind turbines, the power outputs were measured for a traditional SRWT model installed in the wake behind the SRWT and DRWT models (i.e., aligned with the oncoming airflow direction) at various downstream locations (i.e., at the downstream locations of X/D = 2.0, 4.0, 6.0, 8.0 and 12.0). Following the previous work, the power outputs of the downstream wind turbine were normalized by the power output of the SRWT operating in isolated condition in order to reveal the power characteristics of the downstream wind turbine due to the wake effects in typical wind farms setting. Figure 14 illustrates the normalized power outputs as a function of the distance between upstream and downstream wind turbine models. As expected, significant power losses are found the in downstream wind turbine model due to ingestion of the low-momentum wake flows. It can be seen clearly that, about 60%~70% power losses can be observed when the downstream wind turbine is sited at the downstream location of X/D = 2.0 for the SRWT and the DRWT models. As revealed quantitatively from the PIV measurements and the point-wise velocity measurements described above, the DRWT designs can harvest more wind energy from the same incoming airflow due to the secondary small rotor appended in front of the main rotor by reducing the root losses. Since the velocity

deficit at the downstream location of X/D = 2.0 in the wake of the CO-DRWT model is larger than those in the other two wind turbine models (shown in Fig. 11), the power output of this model is also found to be lower than the others from the Fig. 14. As illustrated in Fig. 11, the velocity deficits in the downstream wakes of the wind turbines would recover gradually as the distance increases, and power losses of the downstream turbine is found to become less and less when the downstream wind turbine is being moved further away from the upstream turbines. As more intense turbulent mixing in the wake can be found in the CO-DRWT case, faster velocity deficit recovery rate is also observed in the downstream region behind the CO-DRWT model. It can be seen obviously that, more kinetic energy can be harnessed by the same wind turbine model at the downstream location of X/D = 4.0, and about 8% more power output is attained behind the CN-DRWT system in comparison to the conventional SRWT case. Recall the CO-DRWT and CN-DRWT systems can produce about 2% and 7% more power output when operating in isolated conditions respectively, so 8% and 15% more power output in total can be achieved by the co-rotating and counter-rotating configurations compared to that of single-rotor design. It indicates that the DRWT designs would not only be able to utilize the wind energy near the hub region by reducing the root losses of the main rotor blades, but also be capable of mitigating wake losses in the downstream airflows by enhance the turbulent mixing in typical wind farms, compared with those of the traditional SRWT design.

With the downstream wind turbine model moving further away from the upstream turbine, the benefit of the DRWT design over the traditional SRWT model in mitigating the wake losses is found to decrease gradually. The difference in the power outputs from the downstream wind turbine sited in the wake flows is found to shrink at the downstream

location of X/D=6.0, which would confirm the streamwise velocity in the wakes of DRWT systems are slightly higher than that in the wake of SRWT shown in Fig. 11(c). Less advantages of the DRWT designs in reducing the wake losses can be found in the power output measurements for the downstream wind turbine, only about 3% more power can be harvested when the wind turbine is sited at the location with the distance of X/D = 12.0. As reported by Barthelmie et al. (2007), the distance between the upstream and downstream wind turbine is around 7 ~ 10 rotor diameters in a typical offshore wind farm, the wake losses can be reduced by 4% ~ 5% from more intensive wake mixing induced by a secondary small rotor added in front of the main rotor in the DRWT designs, compared to the traditional SRWT system.

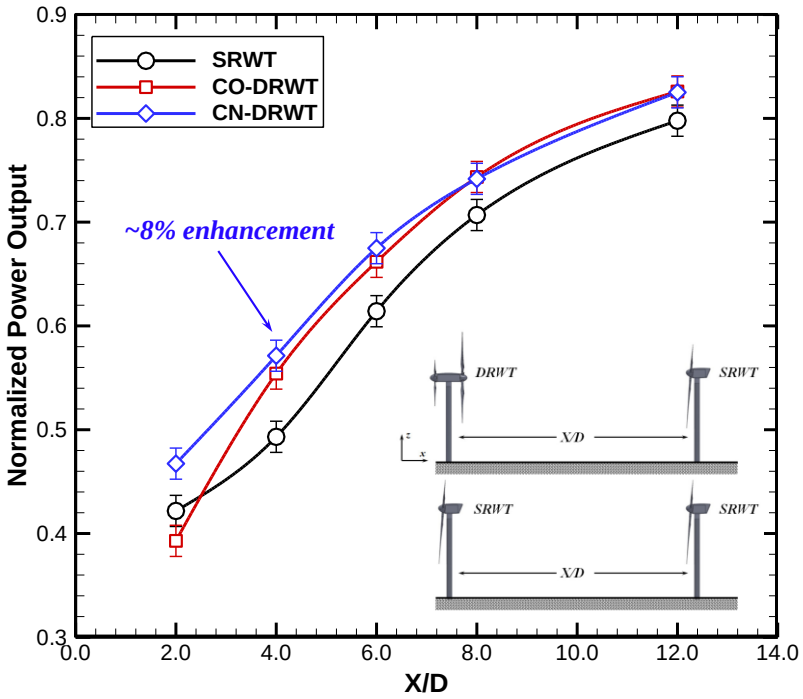

Figure.14 Normalized power measurements of the downstream wind turbine sited in the wakes behind the SRWT and DRWT models

5.3.5. Stereoscopic PIV measurements

Similar to the investigations conducted in Chapter 4, a high-resolution Stereoscopic PIV (SPIV) system was also employed in the present study to measure the three velocity components (*u*,*v*,*w*) at several pre-selected vertical planes (Y-Z planes) perpendicular to the central plane (used in 2-D PIV measurements) in the turbulent wake. Figure 15 illustrates the set-up used for the SPIV measurements, two PCO cameras equipped with two 105mm lenses were arranged at the downstream side of the laser sheet. Similar to the 2-D PIV measurements, the "free-run" and the "phase-locked" measurements were acquired and processed to analyze the flow quantities in the wind turbine wakes.

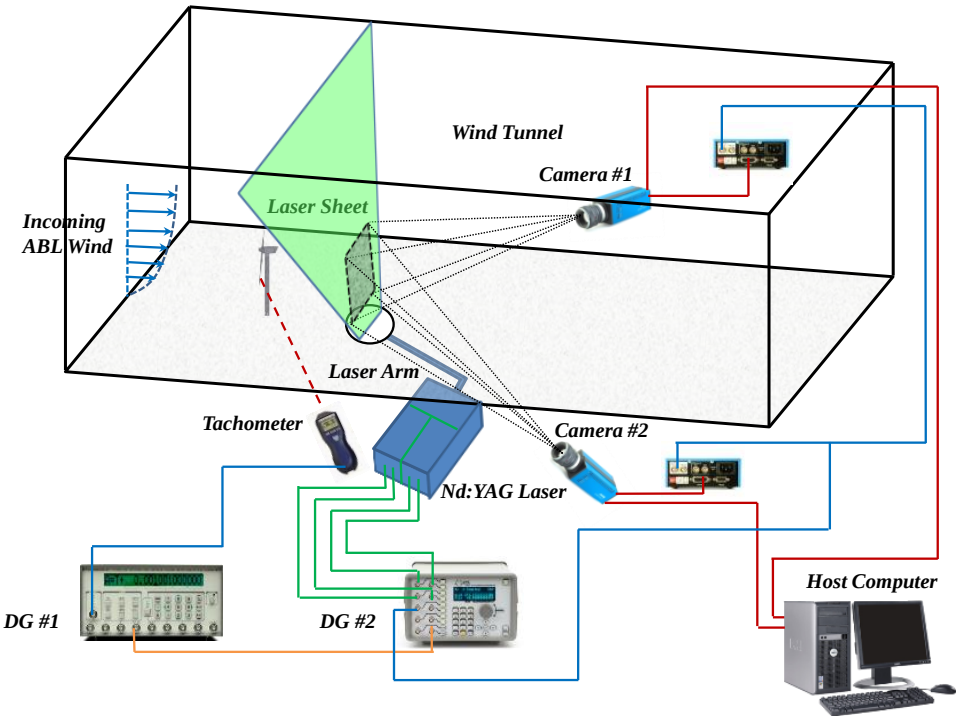

Fig.15 Experimental setup used for Stereoscopic PIV measurements

Figure 16 shows the time-averaged velocity distributions at three downstream locations from the near wake to the far wake regions (i.e., X/D=1.0, X/D=2.0 and X/D=4.0) behind the wind turbine models. The three-component velocities can be obtained by the stereoscopic

PIV measurements, the color contour and the arrows shown in Fig. 16 represent the streamwise velocity (u) and the sum of swirling velocities (v,w), respectively. It should be noted that, the positions of the laser sheet to illuminate the PIV measurement plane and the cameras to acquire the images were fixed during the experiments. The locations of the upstream wind turbines were changed along the streamwise direction to attain different distances between the wind turbine and the laser sheet. As expected, significant velocity deficits can be found in the region behind the turbine rotor disks in the wakes of the wind turbine models, especially in the wake region near the turbine (i.e., X/D $\leq$ 2.0). The velocity deficits are recovered gradually as the turbulent mixing keeps increasing in the downstream wakes, and the wake behind the wind turbine models can be observed to be expanded gradually as the downstream distance increases.

It can be seen clearly that the deficits in streamwise velocity and the magnitude of the swirling velocity at the measuring location of X/D =1.0 in the wake of DRWT models are higher than those of the SRWT system. It confirms the findings derived above and indicates more wind energy in the same incoming airflow is harvested by the DRWT systems. A more intensive swirling velocity is induced by the interactions between the front and the rear rotors. The streamwise velocity deficits in the wake region of X/D = 1.0 can be found to be the highest level in the case of CO-DRWT model among the measured three cases, which corresponds with the highest dynamic wind loading and bending moment shown in Fig. 5 and Table. 1. It should be noted that, the rotational directions for the main rotor in the co-rotating and counter-rotating cases are opposite, which would dominate the rotational direction of the swirling velocity in the downstream wakes. When the downstream measuring plane is moved to X/D = 2.0, the velocity deficits in the low-momentum airflow region

behind the DRWT systems are slightly higher than that in the SRWT case, which would be consistent with the velocity measured by Cobra Probe Anemometry (shown in Fig. 11a). In addition, more intensive swirling velocities are also found in the DRWT cases compared with the measuring result in the SRWT case, which would be related to the higher turbulent mixing and TKE levels illustrated in the previous 2-D PIV measurements. As discussed above, faster recovery of velocity deficits can be observed in the wake behind the of the DRWT systems. Therefore, the velocities behind them demonstrated in Fig. 16 are found to be recovered to a higher level than that behind the SRWT model at the downstream location of X/D = 4.0. As a result, more wind energy is available in the downstream airflows and higher power yields can be obtained by the duplicate SRWT model sited behind the wake of DRWT systems.

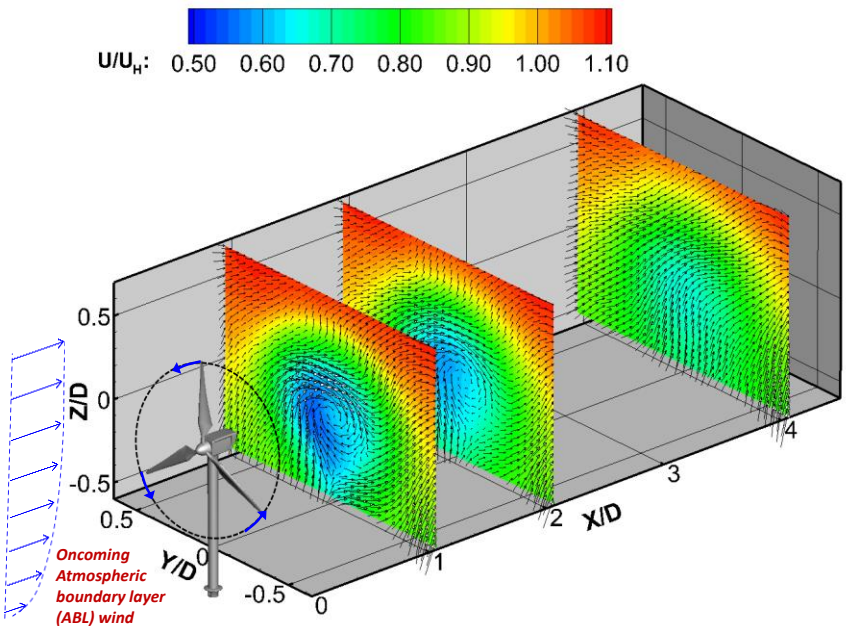

(a) The velocity distributions in the wake behind the SRWT model

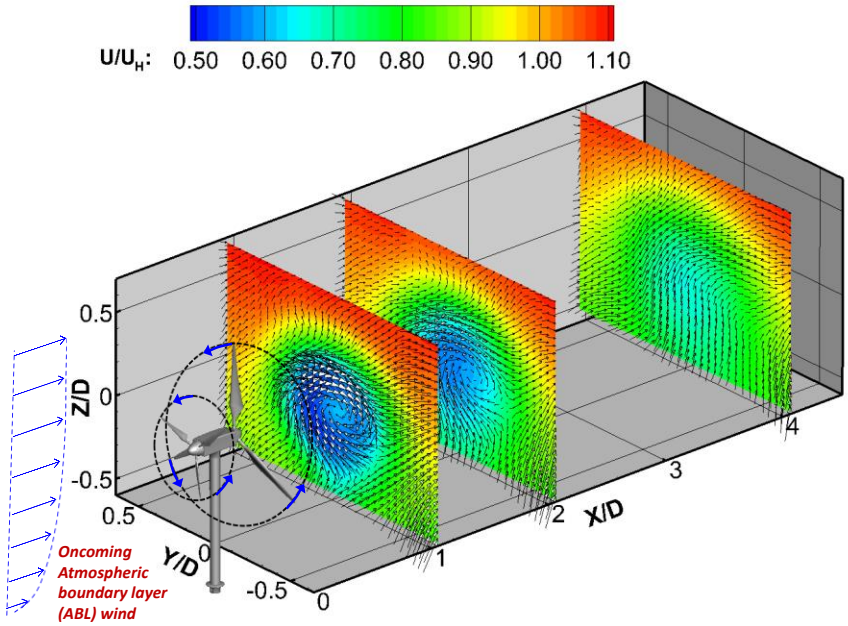

(b) The velocity distributions in the wake behind the CO-DRWT model

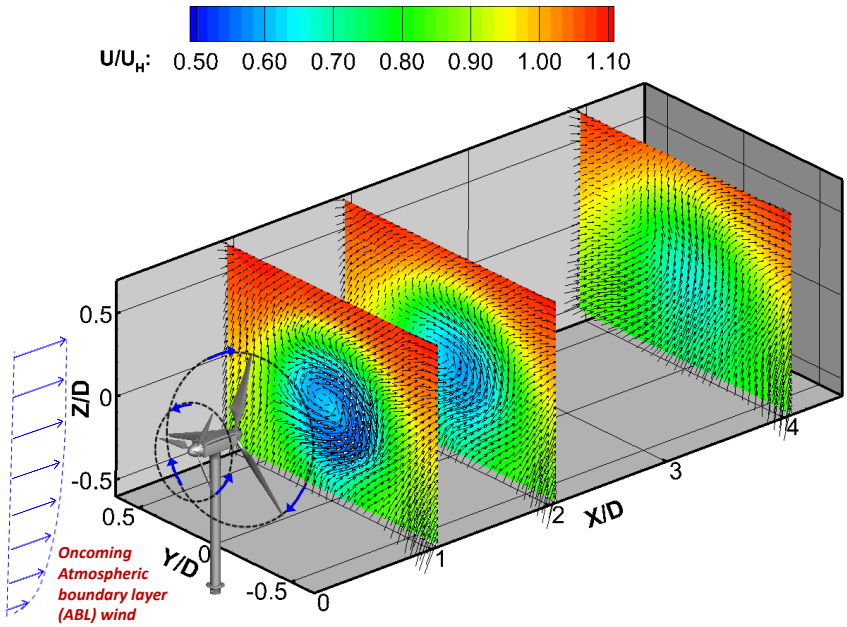

(c) The velocity distributions in the wake behind the CN-DRWT model

Fig. 16 Ensemble-averaged velocity distributions in the wake behind the wind turbine models

Figure 17 depicts the normalized TKE ($TKE = 0.5(\overline{u'^2} + \overline{v'^2} + \overline{w'^2})/U_H^2$) distributions in the wake flows (i.e., X/D = 1.0, 2.0 and 4.0) behind the SRWT and the DRWT models. TKE is an important parameter to evaluate the extent of turbulent mixing in a turbulent flow in the wake behind a wind turbine model (Tian et al., 2014). As Fig. 9 only showed the vertical central plane for the 2-D PIV measurement up to X/D ≈ 2.2, more comprehensive flow details and statistics can be obtained through the stereoscopic PIV measurements from the near wake to the far wake regions. It can be seen that the TKE levels are to be the highest in the wake of CO-DRWT design among the all measured wind turbine models, which would be consistent with the TKE results measured in Fig. 9 through 2-D PIV measurement. As suggested by Tian et al. (2014), the much higher TKE levels would indicate more intensive wake mixing in the downstream region, corresponding to a much faster velocity recovery in the turbulent wake of the CO-DRWT case. The relationship between the TKE levels and the velocity deficit recovery in the wake flows can be affirmed with the power output measurements shown in Fig. 14. The higher swirling velocity may also have a close relationship with the higher TKE levels in the wake regions of the wind turbine models. Due to the dual-rotor designs in DRWT models, the benefits of reducing the losses near the root regions of the main rotor blades and mitigating the losses in the wakes by enhancing the turbulent mixing can be quantified by the detailed flow statistics measurements in the wake flows.

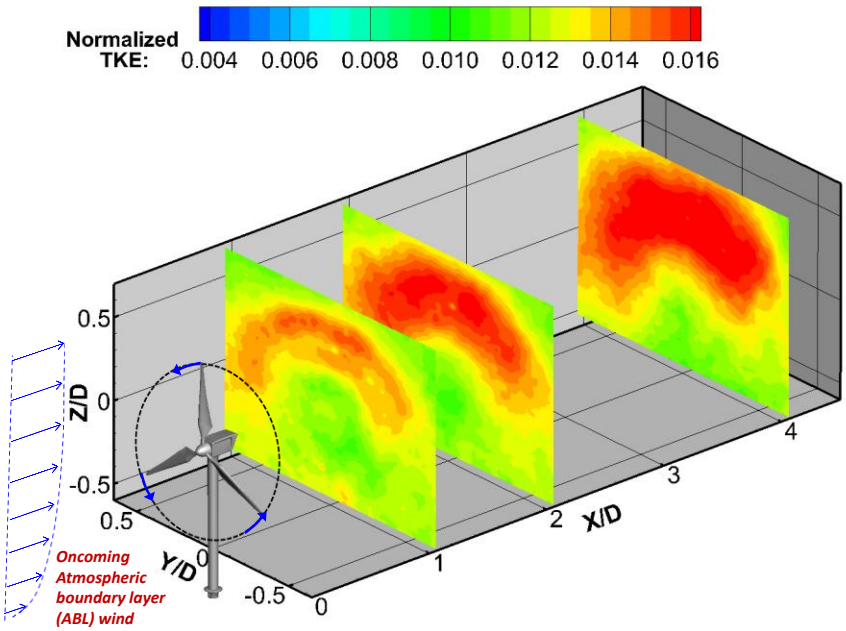

(a) The TKE distributions in the wake behind the SRWT model

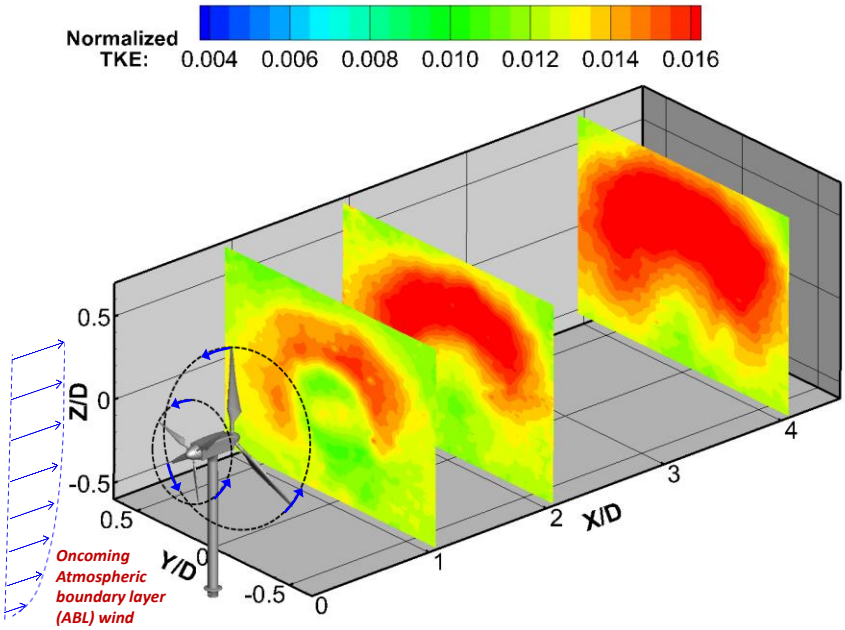

(b) The TKE distributions in the wake behind the CO-DRWT model

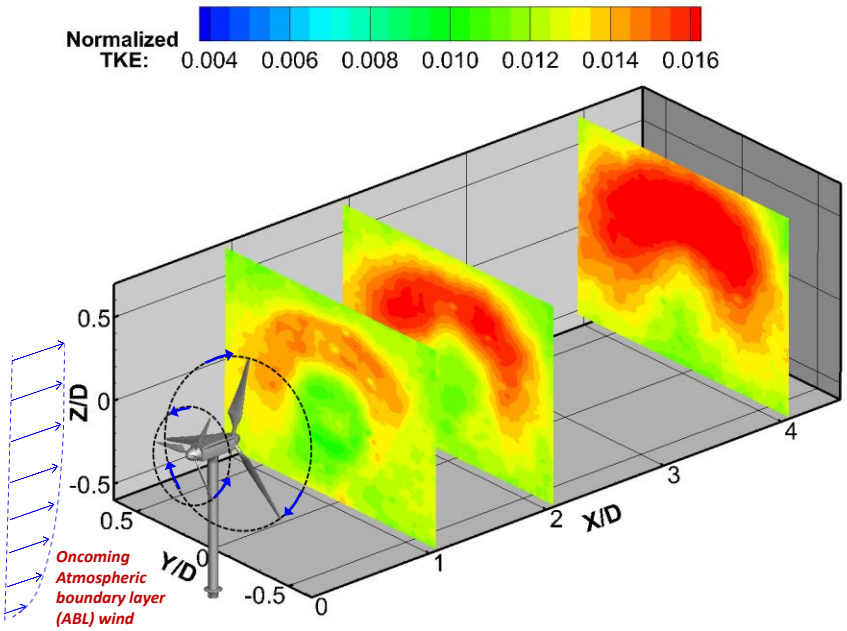

(c) The TKE distributions in the wake behind the CN-DRWT model

Fig. 17 Ensemble-averaged TKE distributions in the wake behind the wind turbine models

5.4. Conclusion

A wind tunnel study was conducted to investigate the aeromechanic performance and the wake characteristics of innovative dual-rotor wind turbines (DRWTs) compred with those of a traditional single-rotor wind turbine (SRWT). The DRWT designs employed a small rotor added in front of the main rotor with two objectives: 1) reduce root losses incurred in the root region of the main rotor blades; and 2) mitigate wake losses of downstream turbines in wind farm settings through enhanced turbulent mixing of turbine wake. The experimental study was performed in a large-scale wind tunnel with scaled DRWT and SRWT models placed in an Atmospheric Boundary Layer (ABL) wind. In addition to measuring the dynamics wind loads acting on the scaled wind turbine models, a high-resolution 2-D PIV and stereoscopic

PIV systems were used to make both "free-run" and "phase-locked" measurements to elaborate the flow characteristics and behavior of the unsteady wake structures in the near and far wakes behind the SRWT and DRWT models. An accurate Cobra Probe Anemometry system was also used to conduct velocity measurements in the far wake regions (i.e., in the downstream locations of X/D≥2.0) to supplement the 2-D PIV measurements. Furthermore, the power outputs of the scaled wind turbines operating in isolated condition and a duplicate model turbine sited in the wake behind the SRWT and DRWT designs were measured and compared quantitatively for detailed analysis.

As an additional rotor was appended in the DRWT designs, it was found to be capable of harnessing more wind energy from the same incoming airflows by reducing the root losses of the main rotor. Higher dynamic wind loads (i.e., ~13% and 3.5% enhancement in mean thrust force on CO-DRWT and CN-DRWT models respectively) were observed to act on the DRWT models than that acting on the SRWT model. More significant fluctuations of the dynamic loads were also found in the DRWT cases, which would indicate more severe fatigue loads acting on the DRWT models and are believed to be closely related to the more complicated vortex structures generated in the wake flows. Higher dynamic wind loading would indicate more power generated from the wind turbine models with 2% and 7% more power were produced by CO-DRWT and CN-DRWT configurations, respectively, compared to the traditional SRWT design.

Due to the existence of the additional rotor installed in front of the main rotor, considerable differences in the flow quantities such as larger velocity deficits in the near wake, more complicated wake vortex structures and higher TKE levels, were observed in the wake behind the DRWT models, in comparison to those in the downstream flow behind the

SRWT model. The position of velocity recovery for all the wind turbine models was found to start from X/D ≈ 1.85, but the velocity recovery rates were found to be higher in the wake of DRWT designs than that in SRWT case. More complex wake vortices and intensive turbulent mixing process were observed to be increased, which would promote the vertical transport of kinetic energy by entraining more high-momentum airflows above the region behind the rotation disk to re-charge the low momentum wake flows behind the DRWT models. As a result, more wind energy would be available in the far wake and higher power outputs can be obtained by a downstream turbine sited in the wake behind the DRWT models (i.e., up to 7% more power output for the same turbine when it was installed at X/D = 4.0 in the downstream airflows). It reveals that the DRWT designs with the additional rotor in front of the main rotor would not only be able to harness more energy from the same incoming airflow by reducing the root loss, but also can mitigate the wake losses in typical wind farm by enhancing turbulent mixing in the wake flows. We believe that the findings derived from the present study are very helpful to gain further insight into aeromechanic characteristics of wind turbines, more comprehensive research is still needed to explore/optimize design paradigms for higher power yield and better durability of wind turbines.

Acknowledgements

The funding support from the Iowa Energy Center with Grant No. 14-008-OG and National Science Foundation (NSF) with Grant Numbers of CBET-1133751 and CBET- 1438099 is gratefully acknowledged.

References

Adaramola, M. S., & Krogstad, P.-Å. (2011). Experimental investigation of wake effects on wind turbine performance. *Renewable Energy*, *36*(8), 2078–2086.

Alfredsson, P. H., Dahlberg, J.-A., & Vermeulen, P. E. J. (1982). A comparison between predicted and measured data from wind turbine wakes. *Wind Engineering*, *6*, 149–155.

Barthelmie, R. J., Folkerts, L., Ormel, F. T., Sanderhoff, P., Eecen, P. J., Stobbe, O., & Nielsen, N. M. (2003). Offshore Wind Turbine Wakes Measured by Sodar. *Journal of Atmospheric and Oceanic Technology*, *20*(4), 466–477.

Barthelmie, R. J., Hansen, K., Frandsen, S. T., Rathmann, O., Schepers, J. G., Schlez, W., Chaviaropoulos, P. K. (2009). Modelling and measuring flow and wind turbine wakes in large wind farms offshore. *Wind Energy*, *12*(5), 431–444.

Barthelmie, R. J., Rathmann, O., Frandsen, S. T., Hansen, K. S., Politis, E., Prospathopoulos, J., Pijl, S. P. Van Der. (2007). Modelling and measurements of wakes in large wind farms. *Journal of Physics: Conference Series*, *75*, 012049.

Barthelmie, R., & Pryor, S. (2010). Quantifying the impact of wind turbine wakes on power output at offshore wind farms. *Journal of Atmospheric and Oceanic Technology*, *8(2010)*.

Cal, R. B., Lebrón, J., Castillo, L., Kang, H. S., & Meneveau, C. (2010). Experimental study of the horizontally averaged flow structure in a model wind-turbine array boundary layer. *Journal of Renewable and Sustainable Energy*, *2*(1), 013106.

Calaf, M., Meneveau, C., & Meyers, J. (2010). Large eddy simulation study of fully developed wind-turbine array boundary layers. *Physics of Fluids*, *22*(1), 015110.

Chamorro L., Arndt R., & Sotiropoulos, F. (2011). Turbulent Flow Properties around a staggered wind farm. *Boundary-Layer Meteorology*, *141*(3), 349–367.

Hansen, K. S., Barthelmie, R. J., Jensen, L. E., & Sommer, A. (2012). The impact of turbulence intensity and atmospheric stability on power deficits due to wind turbine wakes at Horns Rev wind farm, *Wind Energy*, 15, 183–196.

Hau, E., & Von Renouard, H. (2000). *Wind turbines: fundamentals, technologies, application, economics* (pp. 67–80). Springer Science & Business Media.

Hu, H., Yang, Z., & Sarkar, P. (2012). Dynamic wind loads and wake characteristics of a wind turbine model in an atmospheric boundary layer wind. *Experiments in Fluids*, *52*(5), 1277–1294.

Jain, P. (2007). *Wind energy engineering*. McGraw Hill Professional.

Jung, S. N., No, T.-S., & Ryu, K.-W. (2005). Aerodynamic performance prediction of a 30kW counter-rotating wind turbine system. *Renewable Energy*, *30*(5), 631–644.

Lee, S., Kim, H., & Lee, S. (2010). Analysis of aerodynamic characteristics on a counter-rotating wind turbine. *Current Applied Physics*, *10*(2 SUPPL.), S339–S342.

Lee, S., Kim, H., Son, E., & Lee, S. (2012). Effects of design parameters on aerodynamic performance of a counter-rotating wind turbine. *Renewable Energy*, *42*, 140–144.

Lignarolo, L. E. M., Ragni, D., Ferreira, C. J. S., & van Bussel, G. J. W. (2014). Kinetic energy entrainment in wind turbine and actuator disc wakes: an experimental analysis. *Journal of Physics: Conference Series*, *524*, 012163.

Medici, D., & Alfredsson, P. H. (2006). Measurements on a wind turbine wake: 3D effects and bluff body vortex shedding. *Wind Energy*, *9*(3), 219–236.

Rosenberg, a, Selvaraj, S., & Sharma, a. (2014). A Novel Dual-Rotor Turbine for Increased Wind Energy Capture. *Journal of Physics: Conference Series*, *524*, 012078.

Ross J N, A. J. F. (1981). Wake measurements in clusters of model wind turbines using laser Doppler anemometry. In *Proceedings of the Third BWEA Wind Energy Conference* (pp. 172–184). Cranfield, UK.

S.A.Hsu, Eric A.Meindl, D. B. G. (1994). Determining the power law wind profile exponent under near neutral stability condition at sea.pdf. *Journal of Applied Meteorology*, 757–765.

Sharma, A. and Frere, A. (2010). Diagnosis of Aerodynamic Losses in the Root Region of a Horizontal Axis Wind Turbine. *General Electric Global Research Center Internal Report*.

Storm, B., Dudhia, J., Basu, S., Swift, A., & Giammanco, I. (2009). Evaluation of the Weather Research and Forecasting model on forecasting low-level jets: implications for wind energy. *Wind Energy*, *12*(1), 81–90.

Tian, W., Ozbay, A., & Hu, H. (2014). Effects of incoming surface wind conditions on the wake characteristics and dynamic wind loads acting on a wind turbine model. *Physics of Fluids*, *26*(12), 125108.

Tian, W., Ozbay, A., Hu, H., Sarakar, P., & Yuan, W. (2013). An experimental study on the performances of wind turbines over complex terrain. *51st AIAA Aerospace Sciences Meeting Including the New Horizons Forum and Aerospace Exposition 2013*, (January),

Tong, W. (2010). *Wind power generation and wind turbine design*. Wit Press.

Newman, B. G. (1986). Multiple Actuator-disc Theory for Wind Turbines. *Journal of Wind Engineering and Industrial Aerodynamics*, *24*, 215–225.

Vermeer, L., Sørensen, J., & Crespo, A. (2003). Wind turbine wake aerodynamics. *Progress in Aerospace Sciences*.

Whale, J., Anderson, C. ., Bareiss, R., & Wagner, S. (2000). An experimental and numerical study of the vortex structure in the wake of a wind turbine. *Journal of Wind Engineering and Industrial Aerodynamics*, *84*(1), 1–21.

Wu, Y.-T., & Porté-Agel, F. (2012). Atmospheric Turbulence Effects on Wind-Turbine Wakes: An LES Study. *Energies*, *5*(12), 5340–5362.

Yuan, W., Tian, W., Ozbay, A., & Hu, H. (2014). An experimental study on the effects of relative rotation direction on the wake interferences among tandem wind turbines. *Science China Physics, Mechanics & Astronomy*, *57*(5), 935–949.

CHAPTER 6. GERNEAL CONCLUSION

In this thesis, the major objectives from the topics of axial fan noise reduction and innovative wind turbine designs are discussed and summarized below.

In Chapter 2, several modification strategies for noise reduction on a baseline axial fan were experimentally investigated. Sound pressure levels and spectra distributions were obtained from the measurements of the newly designed fan and the baseline fan. The results revealed that, the flow rate from the newly designed fan was about 30~40% higher than that of the baseline model at the same rotation speed. The overall sound pressure level for the newly designed fan at the relatively low flow rate (e.g., $3m^3$/min) was about 3 dB quieter but and there is about a 6 dB decrease at the relatively high flow rate (e.g., $7m^3$/min) than that of the baseline case. In addition, the power output requirement for the newly designed fan was less than that of the baseline fan at the same flow rate, which would indicate higher flow efficiency in the newly designed fan. The measured spectra results also demonstrated that the amplitudes of both the tonal and the broadband components of the newly designed fan were less predominant than that radiated from the baseline fan. The PIV results illustrated that the discontinuous flow in the lower stream emanated from the baseline fan, which indicates poor design may exist in the guide vane. The wake expansion angles in the newly designed fan case were found to be higher than those of the baseline case. Lower TKE and Reynolds stress levels were also observed in the wake of the newly designed fan compared to those of the baseline fan, which means lower flow fluctuations and weaker shear stress in the wake flows were induced by the pressure fluctuations through rotor-stator interaction.

Following with the work conducted in Chapter 2, a numerical study was performed in Chapter 3 to provide more useful information to elucidate the noise radiation from the newly

designed axial fan. The qualitative and quantitative measurements from the PIV results agreed very well with the numerical solutions. The instantaneous pressure solutions represent the high negative pressure regions on the blade surface existing close to the rotor region. When the blades rotated close to the guide channel, the static pressure near the tip region was increased to some extent compared with the blades on the other phase angles. The streamline patterns demonstrated the unsmooth flow path occurred in the flow passages, which could be caused by the severe interactions between the blades and stators or inappropriate design such as angle of attack or stagger angle in the rotor. This could induce the unnecessary noise emitted from the fan by reasons such as boundary layer separation from the blade surfaces. The time-averaged normalized TKE distributions and static pressure fluctuations caused by rotor-stator interactions indicated the locations of the noise sources, which may also indicate the flow separations occurring in rotary regions, and induce the high TKE levels and pressure fluctuations in the downstream wake flows.

In Chapter 4, an experimental study was conducted to explore a novel twin-rotor wind turbine (TRWT) concept for improved aerodynamic performances of isolated wind turbines as well as better wind farm efficiency. The measurement results revealed clearly that, while the TRWT design with an extra auxiliary rotor appended in front of the turbine main rotor was found to be capable of harvesting more wind energy from the same incoming boundary layer flow by reducing the root losses of the main rotor blades, the dynamic wind loads acting on the TRWT model were also found to be much greater (i.e., ~ 16% increase in time-averaged wind loads, up to 140% increase in the fluctuating amplitudes of the instantaneous wind loads) than those acting on the SRWT model. The much larger fluctuating amplitudes of the dynamic wind loads would indicate more significant fatigue loads acting on the TRWT

model, which is believed to be closely related to the more complex vortex structures generated in the wake behind the TRWT model due to the existence of the extra auxiliary rotor. It was also found that, due to the existence of the additional auxiliary rotor appended in front of the main rotor, significant differences in flow characteristics (i.e., much larger velocity deficits in the near wake, more complex wake vortex structures, earlier breakdown of the concentrated wake vortices, and higher TKE and turbulent Reynolds stress levels) were found in the near wake behind the TRWT model, in comparison with those in the near wake behind the SRWT model. Due to the more complex wake vortices generated behind the TRWT model, the turbulent mixing process in the TRWT wake flow was found to be enhanced greatly, which would promote the vertical transport of kinetic energy by entraining more high-speed airflow from above to re-charge the low momentum wake flow and resulting in a much faster recovery of the velocity deficits in the wake behind the TRWT model. Therefore, the wake flow behind the TRWT model was found to become more energetic in the far wake region of X/D>3.0 than that behind the SRWT model. As a result, the power output of a downstream turbine sited in the far wake behind the TRWT model was found be substantially greater than that of the same turbine sited in the wake behind a conventional SRWT model (i.e., up to 7% more power output for the same downstream turbine when it sited at 6.0 rotor diameters away from the upstream turbine). It indicates that the TRWT design with an extra auxiliary rotor appended in front of the main rotor would not only be able to harvest more energy from the same incoming wind by reducing the root losses, but also can mitigate the wake losses of the downstream turbines in typical wind farm settings through enhanced turbulent mixing of the turbine wake flows. The phase-locked flow fields at the downstream location in the turbulent wake of X/D=1.0 measured by the

stereoscopic PIV technique reveal that, higher streamwise velocity deficit can be found in the central region of TRWT model and the blade phase angle location would have obvious impacts on the distributions of transversal velocity. Much higher TKE levels in the wake of TRWT model indicate more intensive wake mixing in the downstream region, which corresponds to a much faster velocity recovery in the turbulent wake.

Following with the study carried out in Chapter 4, a dual-rotor wind turbine design was proposed in Chapter 5 to improve the wind turbine performance and enhance the wind farm efficiency. It can be revealed clearly that, higher dynamic wind loads (i.e., ~13% and 3.5% enhancement in mean thrust force on CO-DRWT and CN-DRWT models respectively) were observed to act on the DRWT models than that acting on the SRWT model. More significant fluctuations of the dynamic loads were also found in the DRWT cases, which indicated more severe fatigue loads acting on the DRWT models and were believed to be closely related to the more complicated vortex structures generated in the wake flows. As higher dynamic wind loads would indicate more power would be generated from the wind turbine models, 2% and 7% more power were produced by CO-DRWT and CN-DRWT configurations respectively compared to the traditional SRWT design. The position of velocity recovery for all the wind turbine model were found to start from X/D ≈ 1.85, but the velocity recovery rates were found to be higher in the wake of DRWT designs than that in SRWT case. More complex wake vortices and intensive turbulent mixing process were observed to be increased, which would promote the vertical transport of kinetic energy by entraining more high-momentum airflows above the region behind the rotation disk to re-charge the low momentum wake flows behind the DRWT models. As a result, more wind energy would be available in the far wake and higher power outputs can be obtained by a downstream turbine sited in the wake

behind the DRWT models (i.e., up to 7% more power output for the same turbine when it was installed at X/D = 4.0 in the downstream airflows). It reveals that the DRWT designs with the additional rotor in front of the main rotor would not only be able to harness more energy from the same incoming airflow by reducing the root loss, but also can mitigate the wake losses in typical wind farm by enhancing turbulent mixing in the wake flows. We believe that although the findings derived from the present study are very helpful to gain further insight into aeromechanic characteristics of wind turbines, more comprehensive research is still needed to explore/optimize design paradigms for higher power yield and better durability of wind turbines.